Some (Oxy)sulfide Materials as Visible Light Driven Photocatalysts for Water Splitting Reaction

（可視光応答型光触媒(オキシ)サルファイド

を用いた水分解反応）

Kiyonori Ogisu

(荻巣　清徳)

Department of Chemical System Engineering,

School of Engineering, The University of Tokyo

2009 Doctoral Thesis

Acknowledgement

I would like to express my hearty thanks to Professor Kazunari Domen and Associate Professor Jun Kubota for valuable discussion and continuous encouragement through my course of my research work. I would like to special thanks Dr. Ishikawa and Dr. Takanabe for their valuable discussions, proper guideline, helpful suggestion, revising the manuscript and kind encouragement. I wish to acknowledge valuable advice and encouragement with Dr. Tsuyoshi Takata, Dr. Masao Katayama (The University of Tokyo), Dr. Kentaro Teramura (Kyoto University), Professor Takashi Tatsumi, Professor Michikazu Hara, Dr. Junko Nomura and Dr. Daling Lu (Tokyo Institute of Technology), and Associate Professor Yasuhisa Maeda (Shizuoka University) .

I appreciate the help received from Professor Hisayoshi Kobayashi and Dr. Yoshiki Shimodaira (Kyoto Institute of Technology) with band structure calculation. I appreciate the help received from Associate Professor Masatomo Yashima (Tokyo Institute of Technology) with crystal structure and electron density analysis. I appreciate the help received from Associate Professor Kenji Toda (Niigata University) with identification of crystal structure. I appreciate the help received from Professor Toshiharu Teranishi, Dr. Masayuki Kanehara, Mr. Masaki Saruyama and Mr. Takahiro Ikeda (University of Tsukuba) with preparation of nanoparticles and characterization.

Acknowledgements are also extended to Mr. Masaaki Yoshida, Mr. Yoshitaka Ozaki and the members of Domen-Kubota Laboratory for their kindness support for my research work. Finally, I would like to thank my parents, older brother, sister, nephew for their encouragement and supports.

2009

Kiyonori Ogisu

Chapter 1

General Introduction

1-1. Research Background

Energy consumption has increased significantly since the start of the industrial revolution. This is due to increases in the human population, production of consumer goods, and use of energy intensive appliances. Our current modes of fossil-fuel-dependent energy-system are leading to huge emissions of carbon dioxide (CO_2) into the atmosphere, which is considered to be a direct cause of the enhanced greenhouse effects responsible for global climate change. According to the Energy information Administration report in 2005,[1] 86% of primary energy production in the world comes from burning fossil fuels. Non fossil sources are hydroelectric 6.3%, nuclear 6.0%, and other (geothermal, solar, wind, and wood and waste) 0.9%. Fossil fuels are non-renewable resources because they are being consumed much faster than they are being formed. A global movement toward the generation of renewable energy is therefore under way to substitute fossil fuels and help meet increased energy needs. Renewable energy is derived from natural processes that are replenished constantly to a great extent; e.g., sunlight, wind, rain, tides and geothermal heat. Present supply from renewable energy sources accounts for 18% of the total energy use in 2006.[2]

The renewable energy has tremendous potential to be exploited for extensive use in the near future. As shown in Table 1-1, the technical potential of renewable energy sources (1.8×10^{21} J) are ~ 30 times more than the current global primary energy use, and several times higher than the projected energy use in 2100 (4.0×10^{20} J).[3] The theoretical potential means the amount of energy theoretically available for energy purposes, such as, in the case of solar energy, the amount of incoming radiation at the surface of the earth. The technical potential is more practical estimate of how much renewable

energy could be put to human use by considering conversion efficiencies of the available technology and available land area. The technical potential of the renewable energy resources clearly indicates that the renewable energy has great margin to be used as the primary energy for human activity.

Table 1-1. The renewable energy resources

	Current use (2001) /exajoule ($\times 10^{18}$kJ)	Technical potential /exajoule	Theoretical potential /exajoule
Hydropower	9	50	147
Biomass energy	51	> 276	2,900
Wind energy	0.1	640	6,000
Solar energy	0.1	> 1,575	3,900,000
Geothermal energy	0.6	-	-
Ocean energy	not estimated	not estimated	7,400
Total	60	> 1,800	> 4,000,000

Solar energy has the highest fraction among the alternative energy resources, thus is considered to be the most promising resource. Almost all of light energy from the sun, however, is not used except for the utilization of photosynthesis in plants. If we want to utilize the solar energy to practice, we have to convert solar energy to accessible energies such as heats, and chemical and electric energies. The representative and practical example of energy conversion system is photovoltaic cells which convert photon energy to electric one with high efficiency. However, present solar cells consisting of the high cost of crystal Si are not able to provide all of the energy consumed by the human to date and limited to electric generation. Recently the researchers have been undertaking and

improving the solar cell system. Dye-sensitized solar cell, so-called Grätzel cell[4], is one of the most advanced technologies at present, and a new class of solar cell that uses available and relatively inexpensive materials which can be fabricated rather easily. Figure 1-1 shows the scheme of dye sensitized cell. The cell system is based on an optically transparent film of TiO_2 particles of a few nanometers in size, coated with a monolayer of charge-transfer dye as a sensitizer for light gathering. The device is able to utilize solar energy with high efficiency (the solar energy conversion yield is 7.1-7.9 %). The large current densities (greater than 12 mA cm^{-2}), excellent stability (giving at least five million turnovers without decomposition of the sensitizers), and low cost of the fabrication make practical applications of these cells feasible. In Chapter 4, the author investigated the system sensitized with CdS quantum dots instead of dye as photoanode.

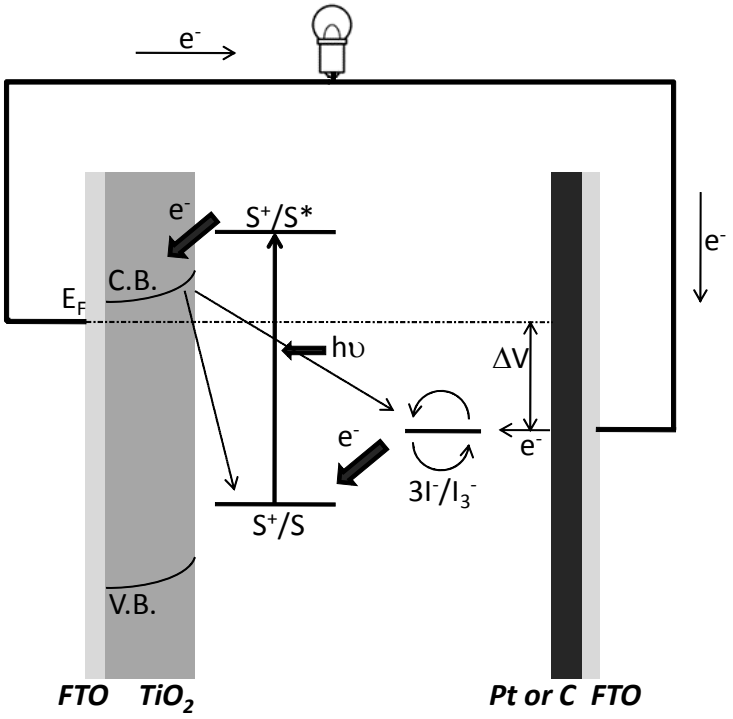

Figure 1-1. Scheme of dye sensitized solar cell

1-2. Photoelectrochemical Generation of Hydrogen and Oxygen from Water

An alternative method to convert solar light into accessible energy form is the production of H_2 energy from prevalent water. Hydrogen is expected to become the main energy carrier in the future because it is a fuel for high efficient fuel cell. However, H_2 is currently produced from fossil fuels such as natural gas and naphtha, and therefore the H_2 production is inevitably accompanied by the formation of CO_2. If sunlight becomes the primary energy resource to produce H_2, the totally clean energy generation system will be established.

Photoelectrochemical water splitting over semiconductors; in particular, photo-assisted decomposition of water at semiconductor electrodes has been the subject of lively research in recent years,[5-9] since the first report of water photoelectrolysis at TiO_2 electrodes by Fujishima and Honda in 1971.[5] Photoelectrochemical cell consists of a rutile TiO_2 photoanode and a Pt counter electrode has been used in these studies (Figure 1-2). In a photochemical cell with an n-type semiconductor electrode, such as TiO_2, the electronic state at the interface between a semiconductor electrode and an aqueous solution creates band bending, which promotes the charge separation as shown in Figure 1-2. The absorption of light in a semiconductor results in electron excitation from the valence band to the conduction band, resulting in the formation of electron-hole pair. The electrons transfer to a Pt counter electrode through an external circuit and H_2 is produced by the reduction of H^+ at Pt electrode. H_2O is oxidized to O_2 by the holes at TiO_2 surface. In this system, TiO_2 photoelectrode requires a degree of chemical or electrical bias to make H_2 to be evolved, because E_{CB} is

approximately 0.2 V more positive than E (H^+/H_2).[5] Since then, many investigations for overall water splitting reaction have been attempted to make it practice without any external bias in both photocatalytic systems and photoelectrochemical reactions.[11-16]

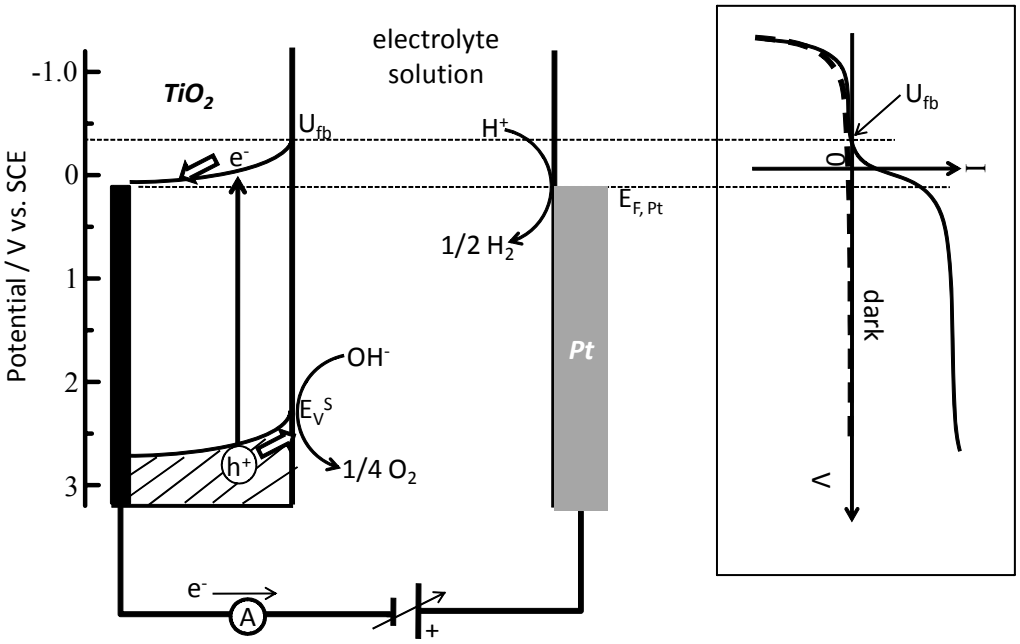

Figure 1-2. Energetic of a photoelectrochemical cell for water splitting

1-3. Photocatalytic Water Splitting over Semiconductor Photocatalysts

1-3-1. Mechanism

Irradiation of a semiconductor with photon of energy equal to or higher than the bandgap leads to electron-hole pair by promotion of an electron from the valence band to the conduction band. The generated electron and hole can be used to drive chemical reactions in a non-spontaneous ($\Delta G > 0$) direction provided that: (a) the bandgap is larger than the energy required for the reaction; (b) the redox potentials of the e^- and h^+ species are sufficient to include the related reduction and oxidation

processes, respectively; and (c) the rates of these redox reactions are fast enough to compete with recombination between electron and hole. These energetic relationships are illustrated in Figure 1-3. In the case of water splitting reaction, semiconductor photocatalyst theoretically need to possess band gap energy greater than 1.23 eV.

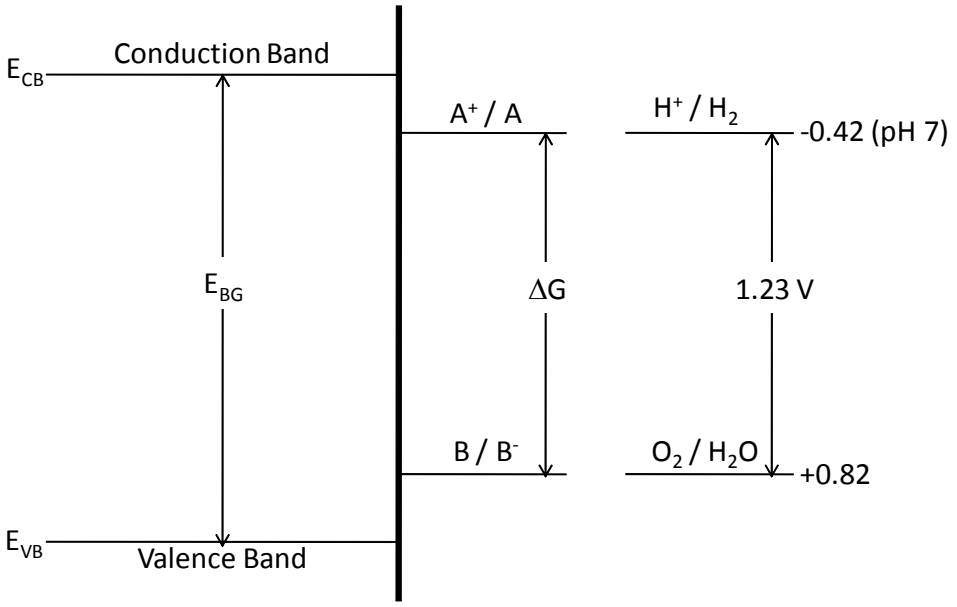

Figure 1-3. Energetic relationship required for driving the reaction: $A^+ + B^- \rightarrow A + B$ by irradiation of a semiconductor. E_{CB} = conduction band, E_{VB} = valence band, E_{BG} = bandgap energy of the semiconductor; A^+/A and B/B^- represent the redox potentials and ΔG is free energy of the reaction.

The processes of photocatalytic water splitting reactions consists of 4 steps as follows[17] (Figure 1-4).

1. Absorption of photons

2. Charge separation of photoexcited electron-hole pairs in the bulk

3. Migration of carriers from bulk to surface (3'. Recombination between photogenerated electron and holes)

4. H_2 and O_2 evolution reactions

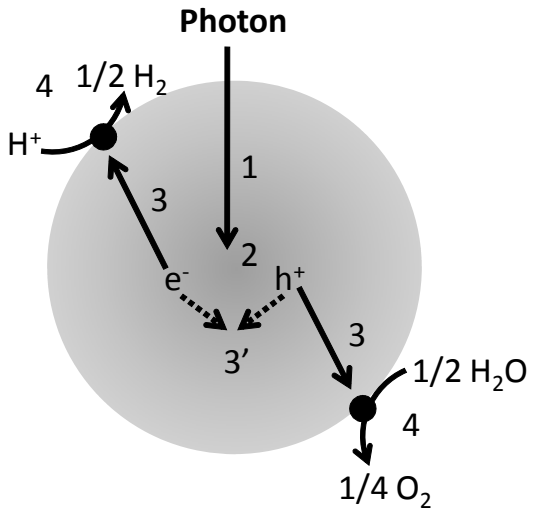

Figure 1-4. Schematic of photocatalytic water splitting reaction in semiconductor particle

The first step (1) of the photocatalytic reaction is absorption of photons. This process only proceeds when photocatalysts materials absorb photon energy greater than the band-gap energy of the material. In order to respond visible light, the band gap (BG) of photocatalysts must be smaller than 3.0 eV. Moreover, the conduction and valence band positions should satisfy the energy requirements set by the reduction and oxidation potential for H_2O, respectively. The second step (2) consists of charge separation of photoexcited electron-hole pairs in the bulk. The third step (3) is migration of carriers from bulk to surface. This process may be affected by the crystallinity of photocatalyst and the defects in bulk. The defects act as trapping and recombination centers between photogenerated electrons and holes (3'), resulting in loss of the photocatalytic activity. The final step (4) includes chemical reactions (e.g., H_2 and O_2 evolution reactions) and photogenerated carriers on the surface.

Figure 1-5 indicates the energetic relationships between the band gap position of several semiconductors and the redox potentials of the water as a reference. [18-21] The reactions are shown as below.

$$2e^- + 2H^+ \xrightarrow{red} H_2$$
$$4h^+ + 2H_2O \xrightarrow{Ox} O_2 + 4H^+$$

The band position of photocatalyst materials is essential to interpose the redox potential for water. Thus, the potential of E_{CB} is more negative than H^+/H_2 (E = -5.67 V vs. vacuum at pH=0), on the other hand, the potential of E_{VB} is more positive than O_2/H_2O redox potential (E = -4.44 V vs. vacuum at pH=0). TiO_2 (rutile), WO_3 and Si do not satisfy these requirements; i.e., those photocatalysts are inactive for the overall water splitting reaction by themselves. Another requisite of the photocatalyst is that it must respond to visible light from the viewpoint of the utilization of sun light. TiO_2 (anatase), $SrTiO_3$, and ZrO_2 have a potential for water splitting reaction under UV-light irradiation, but they can not absorb visible light. On the other hand, several non-oxides such as phosphide (GaP), sulfide (CdS) and selenide (CdSe) satisfy the two requirements with having sufficient potentials for water splitting and good absorption properties in the visible region.[21-22] However, these materials are not stable under irradiation because the materials decompose during oxidation of water to form O_2 by photoanodic dissolution. For example, CdS is photooxidized as follows.

$$CdS + 2h^+ \rightarrow Cd^{2+} + S$$

This indicates that a band position is just one of the essential requirements for water splitting reaction. The essential factors for water splitting reaction are summarized as follows.

I. Band position of the photocatalysts (sufficient potential for water splitting and visible light response)

II. Stability of the photocatalysts (photostability and insolubility in water)

III. Crystallinity of the photocatalysts (the low probabilities of recombination between electrons and holes)

IV. The presence of active sites for the formation of H_2 and O_2

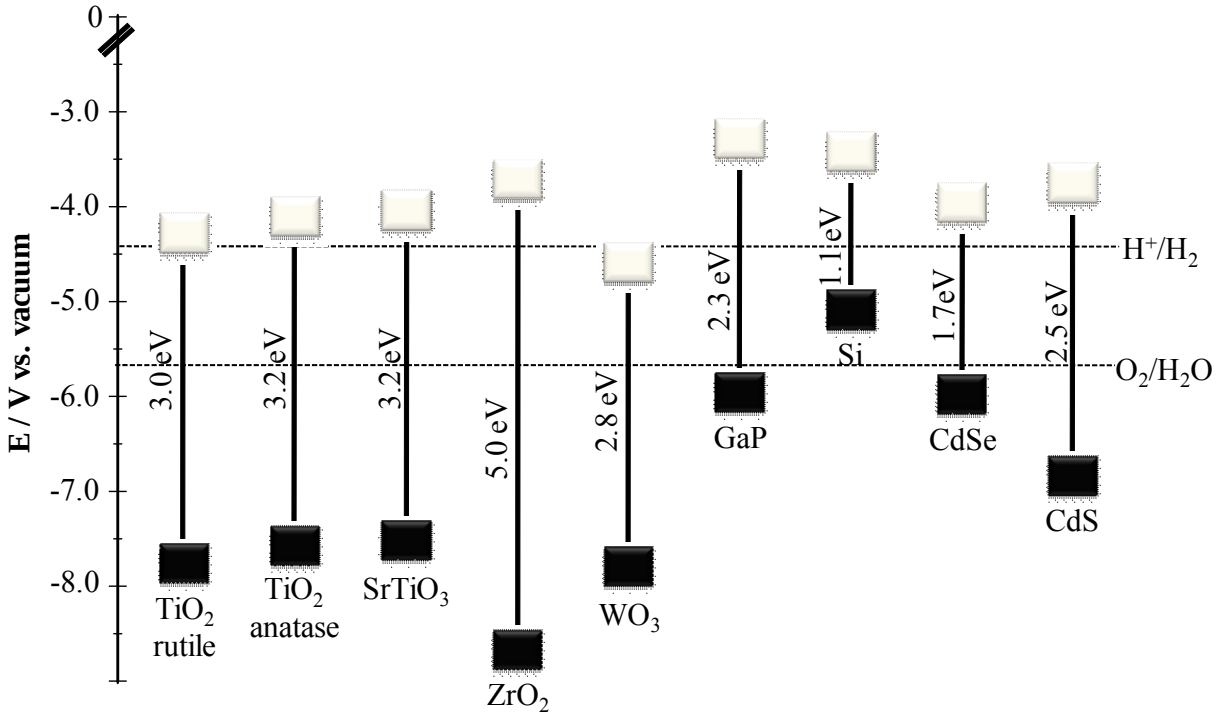

Figure 1-5. Band-edge positions of several semiconductors at pH=0

1-3-2. Materials for Photocatalytic Water Splitting

Photocatalysts for overall water splitting include some transition or typical metal base oxides as summarized in Table 1-2.[24-43]

Table 1-2. Metal based oxide photocatalysts with d^0 or d^{10} electronic configuration

Cation (d^0 cation)	Oxide photocatalysts
Ti^{4+}	TiO_2, $SrTiO_3$, $Na_2Ti_6O_{13}$, $BaTi_4O_9$, $K_2La_2Ti_3O_{10}$
Zr^{4+}	ZrO_2
Nb^{5+}	$K_4Nb_6O_{17}$, $Sr_2Nb_2O_7$
Ta^{5+}	$K_3Ta_3Si_2O_{13}$, $ATaO_3$ (A=Li, Na, K), $BaTa_2O_6$, $RbNdTa_2O_7$, $H_2SrTa_2O_7 \bullet nH_2O$
W^{6+}	$AMWO_6$ (A=Rb, Cs; M=Nb, Ta)

Cation (d^{10} cation)	Oxide photocatalysts
Ga^{3+}	$ZnGa_2O_4$
In^{3+}	$AInO_2$ (A=Li, Na), AIn_2O_4 (A=Ga, Sr)
Ge^{4+}	Zn_2GeO_4
Sn^{4+}	Sr_2SnO_4
Sb^{5+}	$NaSbO_3$, $CaSb_2O_6$, $A_2Sb_2O_7$ (A=Ca, Sr)

All of these photocatalysts have wide band gap and include metal cations with d^0 or d^{10} electronic configuration (d^0 or d^{10} type oxide). The concept of band structure is shown in Figure 1-6. The valence band consists of O 2p orbital in both types, and the conduction bands of d^0 and d^{10} metal based materials consist of nd (n=3,4,5) and ns+np (n=3,4,5) orbitals, respectively.

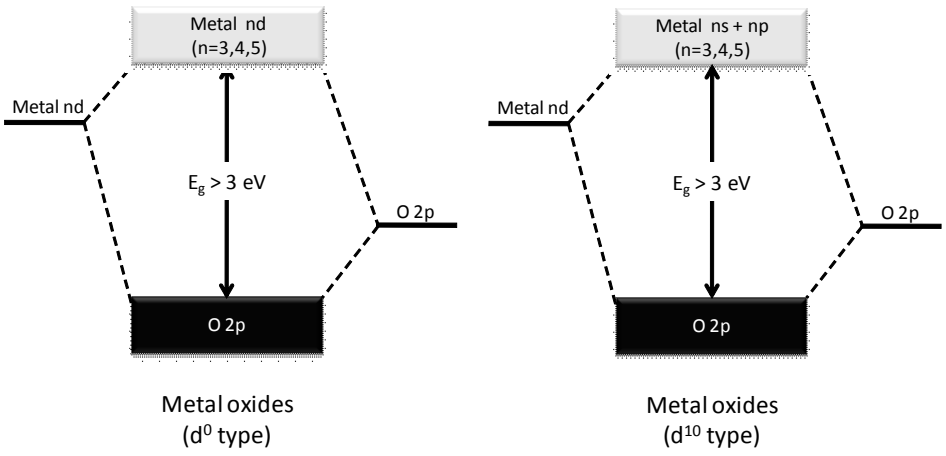

Figure 1-6. Schematic band structure of d^0 type or d^{10} type metal oxide

It was reported in 1980's that Pt/TiO_2 (anatase) was not able to produce H_2 and O_2 because of the rapid reverse reaction from H_2 and O_2 to H_2O over Pt cocatalyst. Then, in a concentrated Na_2CO_3 solution, evolution of H_2 and O_2 was observed while suppressing the reverse reaction.[44] NiO_x cocatalyst is effective to suppress the reverse reaction, and therefore NiO_x has been widely used as an effective cocatalyst for photocatalytic water splitting.[45-47] Structural separation between the reduction and oxidation sites were also considered to be the effective approach to prevent reverse reaction of overall water splitting. First example was $K_4Nb_6O_{17}$ which had an ion exchangeable layers. As shown in Figure 1-7 (a), Ni metal particles as H_2 evolution sites were loaded in interlayer I as ultrafine particle and dispersed uniformly.[31] Photoexcited electrons in niobate sheets transfer to the ultrafine Ni metal particles in interlayer I and reduce H^+ to H_2, and holes oxidize H_2O to O_2 at the interlayer II.[31] Second example was $NaTaO_3$:La which had high efficiency for water splitting reaction under UV irradiation. The mechanism is illustrated in Figure 1-7 (b).[36] The characteristic nanostep structure was created at the surface of the $NaTaO_3$:La particles. The reaction sites for H_2 and O_2 evolution were effectively separated from each other because of the ordered surface nanostep structure. At the edges of the reduction sites, H^+ is effectively reduced to H_2 on the highly dispersed ultrafine NiO particles. On the other hand, photogenerated holes migrate to the groove of oxidation sites. The walls on both sides of the groove would facilitate the multihole injection and the coupling between intermediate species to form O_2.[36]

On the other hand, d^{10} type oxides such as MIn_2O_4 (M=Ca and Sr) have been reported

similarly.[42] The distortion of InO_6 octahedral plays an important role, causing formation of local dipole moments, resulting in the efficient charge separation. The conduction band of d^{10} type photocatalyst consists of hybridized sp orbitals, while that of d^0 type photocatalyst consists of empty d orbitals. The conduction band is more delocalized for photogenerated electrons for d^{10} type photocatalysts than for d^0 type photocatalysts.

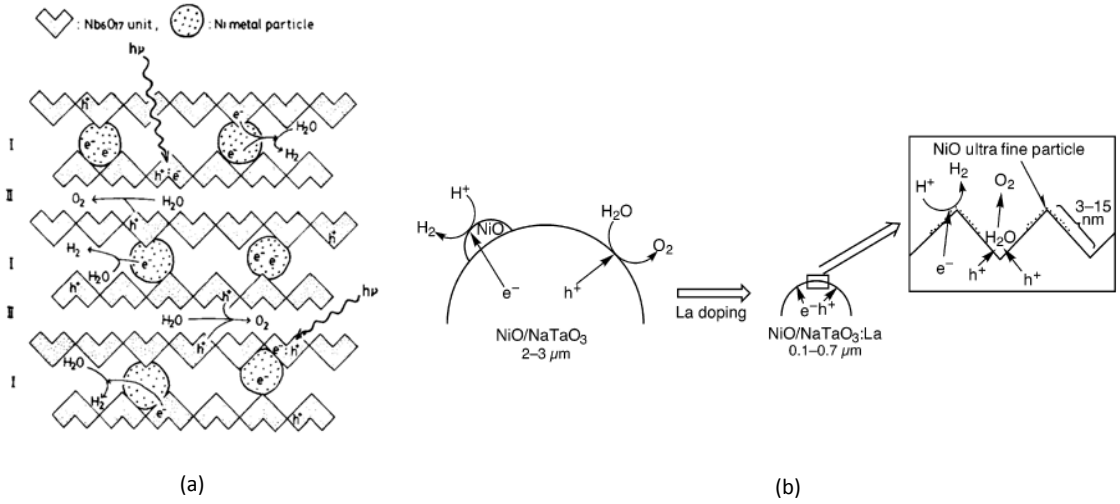

Figure 1-7. Schematic illustrations of reaction mechanism of (a) Ni-$K_4Nb_6O_{17}$ and (b) NiO-$NaTaO_3$:La

1-3-3. Development of Visible Light Driven Photocatalysts

The above mentioned oxide photocatalysts only respond to UV-light, that is, these photocatalytic reactions on these photocatalysts are not driven by visible light which occupies large part of solar energy. $NiO_x/In_{0.9}Ni_{0.1}TaO_4$[48] and $Pt/CdS/RuO_2$[49] have been reported to be visible light driven photocatalysts for overall water splitting, but these data are hardly reproducible. For several years, Domen's group has extensively explored to non-oxide materials such as oxy(nitride) and

oxy(sulfide) materials as visible light driven photocatalysts instead of oxides. For absorption in the visible region and adequate band position for water splitting, the design of the band structure of materials by suitable band engineering is needed. The strategies for development of visible light driven photocatalysts are classified into three ways as shown in Figure 1-8. Some visible light driven photocatalysts have already been discovered by these strategies.[50-72]

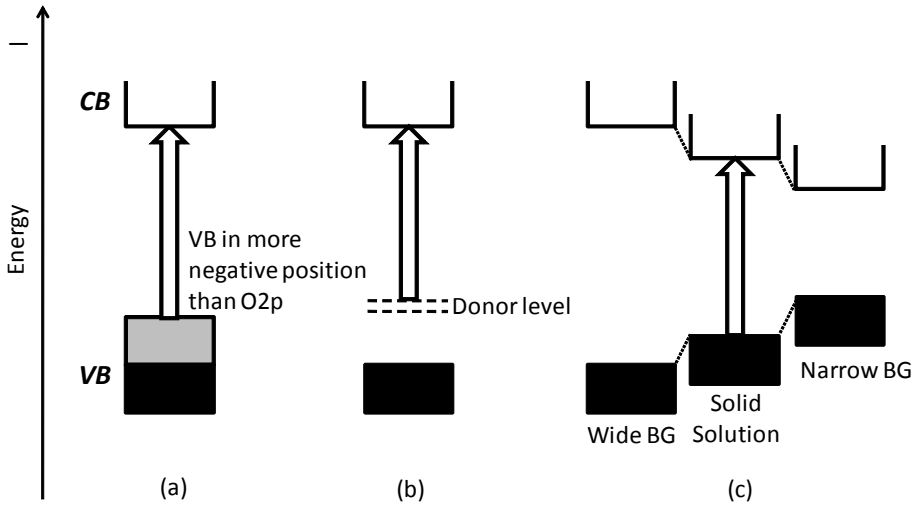

Figure 1-8. Band engineering for photocatalyst materials with visible light response

Strategy (a) is to survey materials that have a stable valence band in more negative position than O2p. This method utilizes the hybridization of orbitals between O2p and the orbitals with more negative orbital than O2p such as cations (Pb6s, Bi6s, Sn5s, and Ag4d orbitals) or anions (N2p, S3p). As cation replaced type materials, $HPb_2Nb_3O_{10}$,[50] $BiVO_4$,[51] $PbBi_2NbO_9$,[52] $AgNbO_3$,[53] Ag_3VO_4,[54] and $SnNb_6O_7$[55] have been reported as visible light driven photocatalysts for H_2 or O_2 evolution. On the other hand, Ta_3N_5,[56] TaON,[57] $LaTiO_2N$,[58] and $Sm_2Ti_2S_2O_5$[59] were reported as examples of anion replace type materials. The density functional theory (DFT) calculations for these semiconductors

have demonstrated that the tops of the valence band is hybridized several cations and anions.

Strategy (b) is the doping of other elements into active photocatalysts with a wide band gap to form donor levels in the forbidden band. The visible light response is attributed to the transition from the electron donor levels to the conduction band of host materials. TiO_2 has been widely used as host materials because of appropriate characteristics for potential application such as photocatalytic activity, low cost, stability, nontoxicity. Recently, Rh-doped $SrTiO_3$,[60] Cr and Ta codoped $SrTiO_3$,[61] Cr and Fe codoped $La_2Ti_2O_7$,[62] N doped $Sr_2Nb_2O_7$,[63] and Ni or Cu doped ZnS[64] have been reported. However, this type of photocatalysts is faced to mainly three problems. One is that foreign elements may act as the recombination centers between photogenerated electrons and holes. Second is that the mobility of the electrons and holes in the doping level is decreased by the presence of the doping levels in a forbidden band. Third is that the absorbing quantity by the transition from doping level to conduction bottom.

Strategy (c) is the control of the energy structure by formation of a solid solution between materials with wide and narrow band gaps. This strategy is often used for band engineering of semiconductors. This idea has been applied to develop a visible light response photocatalyst; e.g., Nb_2O_5-Bi_2O_3,[65] Ga_2O_3-In_2O_3,[66] $Sr_2Nb_2O_7$-$Sr_2Ta_2O_7$,[67] SnO_2-TiO_2,[68] ZnS-CdS,[69] and CdS-CdSe[70] solid solutions. Recently, GaN-ZnO[71] and ZnO-$ZnGeN_2$[72] achieved the evolution H_2 and O_2 simultaneously by visible light irradiation. The advantages of solid solution are more sufficiently absorption of visible light than photocatalysts doped with foreign elements to form novel band. Another advantage is that photoinduced electrons and holes are smoothly transfered to the surface

through the continuous energy bands formed by making a solid solution.

The author has studied oxysulfide materials as photocatalyst candidates on the basis of strategy (a). Ishikawa reported that $Ln_2Ti_2S_2O_5$ (Ln = Pr, Nd, Sm, Gd, Tb, Dy, Ho, and Er) oxysulfide materials behave as stable photocatalysts for H_2 or O_2 evolution reactions.[73] However, other oxysulfide photocatalysts have not been reported. The author attempted to discover novel oxysulfide photocatalysts and evaluation of photocatalytic performance such as photocatalytic reaction for H_2 and/or O_2 evolution reaction or photoelectrochemical measurements. Another approach applied in the current study is to utilize quantum size effect which causes a blue shift in the optical band gap when the diameter of the semiconductor approaches the Bohr diameter. The author dealt with CdS nanoparticles exhibiting quantum size effect with protective organic ligands, and immobilized the nanoparticles on TiO_2 to exhibit the CdS nanoparticle nature.

1-4. Objects of the Present Thesis

In this thesis, the possibility of visible light driven photocatalysts for overall water splitting over oxysulfide materials is demonstrated. The author has studied the preparation and photochemical properties of various oxysulfides based on metal ions with d^0 or d^{10} electronic configuration. Another approach in this research is that CdS nanoparticles exhibiting quantum size effect with a narrow particle size distribution, which were then immobilized on an oxide substrate in attempt to preserve particle size and optical property during photocatalytic H_2 evolution and photoelectrochemical reaction in Na_2S-Na_2SO_3 solution under visible light.

Chapter 1: This chapter explains the background for this research and principles of photocatalytic reactions. The strategies for development of visible light driven photocatalyst were also discussed.

Chapter 2: This chapter describes the possibility of new oxysulfides based on metal ions (Cu^{+}, Zn^{2+}, In^{3}+, Ga^{3+}, Ge^{4+}, and Sn^{4+}) with d^{10} electronic configuration as visible light driven photocatalysts through the photocatalytic reactions and photoelectrochemical measurements. In these materials, $La_5In_3S_9O_3$ and La_3GaS_5O are demonstrated to evolve H_2 or O_2 from water containing hole scavengers (Na_2S-Na_2SO_3) or electron scavenger (Ag^{+}).

Chapter 3: This chapter describes the possibility of new oxysulfides based on metal ions (Ti^{4+}, Nb^{5+}, and Sn^{4+}) with d^0 electronic configuration as visible light driven photocatalysts through the photocatalytic reactions and photoelectrochemical measurements.

Chapter 4: This chapter describes the application of CdS nanoparticles exhibiting quantum size effect dispersed on TiO_2 through the photocatalytic reactions and photoelectrochemical measurements.

Chapter 5: The results described in the Chapters 2-4 are summarized.

References

1. Intergovernmental panel on climate change report 2007
2. International Energy Annual 2005, Retrieved on 2007-09-09.
3. World Energy Assessment 2001.
4. B. O'Regan, M. Grätzel, *Nature,* **353**, 737 (1991).
5. A. Fujishima, K. Honda, *Nature*, **238**, 37 (1972).
6. M. D. Archer, *J. Appl. Electrochem.* **5**, 17 (1975).
7. H. Gerischer, B. Bunsenges, *Phys. Chem.* **80**, 1046 (1976).
8. A. J. Bard, *J. Photochem.* **10**, 59 (1979)
9. A. J. Nozik, *Annu. Rev. Phys. Chem.* **29**, 189 (1978).
10. M. S. Wringhton, *Accts. Chem. Res.* **12**, 303 (1979).
11. T. Watanabe, A. Fujishima, K. Honda, *Bull. Chem. Soc. Japan* **49**, 355 (1976).
12. M. S. Wringhton, A. B. Ellis, P. T. Wolczanski, D. L. Morse, H. B. Abrahamson, D. S. Ginley, *J. Am. Chem. Soc.* **98**, 2774, (1976).
13. J. G. Mavroides, J. A. Kafalas, D. F. Kolesar, *Appl. Phys. Lett.* **28**, 241 (1976).
14. R. D. Nasby, R. K. Quinn, *Mater. Res. Bull.* **11**, 985 (1976).
15. G. N. Schrauzer, T. D. Guth, *J. Am. Chem. Soc.* **99**, 7189 (1977).
16. H. V. Damme, W. K. Hall, *J. Am. Chem. Soc.* **101**, 4373 (1979).
17. A. Kudo, H. Kato, I Tsuji, *Chem. Lett.* **33**, 1534 (2004).

18. E. C. Dutoit, F. Cardon, F. Vanden Kerchove, W. P. Gomes, *J. Appl. Electrochem.*, **8**, 247 (1978).

19. V. N. Pak, N. G. Ventov, *Zh, Fiz. Khim.*, **49**, 2535 (1975).

20. J. M. Bolts, M. S. Wringhton, *J. Phys. Chem.* **80**, 2641 (1976).

21. H. H. Kung, H. S. Jarrett, A. W. Sleight, A. Ferretti, *J. Appl. Phys.* **48**, 2463 (1977).

22. A. B. Ellis, S. W. Kaiser, J. M. Bolts, M. S. Wringhton, *J. Am. Chem. Soc.,* **99**, 2839 (1977).

23. R. Williams, *J. Chem. Phys.*, **32**, 1505 (1960).

24. S, Sato, J. M. White, *J. Chem. Phys. Lett.*, **72**, 83 (1980).

25. K. Domen, S. Naito, M. Soma, T. Onishi, K. Tamaru, *J. Chem. Soc., Chem. Commun.*, 543 (1980).

26. Y. Inoue, T. Kubokawa, K. Sato, *J. Chem. Soc., Chem. Commun.* 1298 (1990).

27. Y. Inoue, T. Niiyama, Y. Asai, K. Sato, *J. Chem. Soc, Chem. Commun.* 579 (1992).

28. T. Takata, Y. Furumi, K. Shinohara, A. Tanaka, M. Hara, J. N. Kondo, K. Domen, *Chem. Mater.*, **9**, 1063 (1997).

29. S. Ikeda, M. Hara, J. N. Kondo, K. Domen, H. Takahashi, T. Okubo, M. Kakihana, *J. Mater. Res.*, **13**, 852 (1998).

30. K. Sayama, H. Arakawa, *J. Phys. Chem.* **97**, 531 (1993).

31. A. Kudo, A. Tanaka, K. Domen, K. Maruya, K. Akira, T. Onishi, *J. Catal.* **111**, 67 (1988).

32. H. G. Kim, D. W. Hwang, J. Kim, Y. G. Kim, J. S. Lee, *Chem. Commun.* 1077 (1999).

33. A. Kudo. H. Kato, *Chem. Lett.* **26**, 867 (1997).

34. H. Kato, A. Kudo, *Chem. Phys. Lett.* **295**, 487 (1998).

35. H. Kato, A. Kudo, *J. Phys. Chem. B*, **105**, 4285 (2001).

36. H. Kato, K. Asakura, A. Kudo, *J. Am. Chem. Soc.* **125**, 3082 (2003).

37. M. Machida, J. Yabunaka, T. Kijima, *Chem. Commun.*, 1939 (1999).

38. K. Shimizu, Y. Tsuji, M. Kawakami, K. Toda, T. Kodama, M. Sato, Y. Kitayama, *Chem. Lett.*, **31**, 1158 (2002).

39. S. Ikeda, T. Itani, K. Nango, M. Matsumura, *Catal. Lett.* **98**, 229 (2004).

40. K. Ikarashi, J. Sato, H. Kobayashi, N. Saito, H. Nishiyama, Y. Inoue, *J. Phys. Chem. B*, **106**, 9048 (2002).

41. J. Sato, H. Kobayashi, N. Saito, H. Nishiyama, Y. Inoue, *J. Photochem. Photobiol. A.* **158**, 139 (2003).

42. J. Sato, N. Saito, H. Nishiyama, Y. Inoue, *J. Phys. Chem. B* **105**, 6061 (2001).

43. J. Sato, H. Kobayashi, K. Ikarashi, N. Saito, H. Nishiyama, Y. Inoue, *J Phys. Chem. B*, **108**, 4369 (2004).

44. K. Sayama, H. Arakawa, *J. Chem. Soc., Faraday Trans.*, **93**, 1647 (1997).

45. K. Dome, A. Kudo, T. Onishi, *J. Catal.* **102**, 92 (1986).

46. M. Machida, S. Murakami, T. Kijima, S. Matsushima, M. Arai, *J. Phys. Chem. B*, **105**, 3289 (2001).

47. D. W. Hwang, J. S. Le, W. Li, S. H. Oh, *J. Phys. Chem. B.*, **107**, 4963 (2003).

48. Z. Zou, J. Ye, K. Sayama, H. Arakawa, *Nature*, **414**, 625 (2001).

49. K. Kalyanasundaram, E. Borgarello, M. Grätzel, *Helv. Chim. Acta.*, **64**, 362 (1981).

50. J. Yoshimura, Y. Ebina, J. N. Kondo, K. Dome, A. Tanaka, *J. Phys. Chem.*, **97**, 1970 (1993).

51. A. Kudo, K. Ueda, I. Mikami, *Catal. Lett.*, **391** (1998).

52. H. G. Kim, D. W. Hwang, J. S. Lee, *J. Am. Chem. Soc.*, **126**, 8912 (2004).

53. H. Kato, H. Kobayashi, A. Kudo, *J. Phys. Chem. B*, **106**, 12441 (2002).

54. R. Konta, H. Kato, H. Kobayashi, A. Kudo, *Phys. Chem. Chem. Phys.*, **5**, 3061 (2003).

55. Y. Hosogi, K. Tanabe, H. Kato, H. Kobayashi, A. Kudo, *Chem. Lett.*, **33**, 28 (2004).

56. M. Hara, G. Hitoki, T. Takata, J. N. Kondo, H. Kobayashi, K. Domen, *Stud. Surf. Sci. Catal.*, **145**, 169 (2003).

57. M. Hara, G. Hitoki, T. Takata, J. N. Kondo, H. Kobayashi, K. Domen, *Catal. Today*, **78**, 555 (2003).

58. A. Kasahara, N. Nukumizu, T. Takata, J. N. Kondo, M. Hara, H. Kobayashi, K. Domen, *J. Phys. Chem. B*, **107**, 791 (2003).

59. A. Ishikawa, T. Takata, J. N. Kondo, M. Hara, H. Kobayashi, K. Domen, *J. Am. Chem. Soc.* **124**, 13547 (2002).

60. R. Konta, T. Ishii, H. Kato, A. Kudo, *J. Phys. Chem. B*, **108**, 8992 (2004).

61. T. Ishii, H. Kato, A. Kudo, *J. Photochem. Photobiol. A*, **163**, 181 (2004).

62. D. W. Hwang, H. G. Kim, J. S. Lee, J. Kim, W. Li, S. H. Oh., *J. Phys. Chem. B*, **109**, 2093 (2005).

63. S. M. Ji, P.H. Borse, H. G. Kim, D. W. Hwang, J. S. Jang, S. W. Bae, J. S. Lee, *Phys. Chem. Chem. Phys.*, **7**, 1315 (2005).

64. A. Kudo, M. Sekizawa, *Catal. Lett.*, **58**, 241 (1999).

65. A. Harriman, J. M. Thomas, W. Zhou, D. A. Jefferson, *J. Solid State Chem.,* **72**, 126 (1988).

66. A. Kudo, I. Mikami, *J. Chem. Soc., Faraday. Trans.*, **94**, 2929 (1998).

67. H. Kato, A. Kudo, *J. Photochem. Photobiol. A*, **145**, 129 (2001).

68. J. Lin, J. C. Yu, D. Lo, S. K. Lam, *J. Catal.*, **183**, 368 (1999).

69. J. F. Reber, M. Rusek, *J. Phys. Chem.*, **90**, 824 (1986).

70. S. Kambe, M. Fujii, T. Kawai, S. Kawai, *Chem. Phys. Lett.*, **109**, 105 (1984).

71. K. Maeda, K. Teramura, D. Lu, T. Takata, N. Saito, Y. Inoue, K. Domen, *Nature*, **440**, 295 (2006).

72. Y. Lee, H. Terashima, Y. Shimodaira, K. Teramura, M. Hara, H. Kobayashi, K. Domen, M. Yashima, *J. Phys. Chem. C*, **111**, 1042 (2007).

73. A. Ishikawa, Y. Yamada, T. Takata, J. N. Kondo, M. Hara, H. Kobayashi, K. Domen, *Chem. Mater.* **15**, 4442 (2003).

Chapter 2

Preparation and Photocatalytic Properties of Oxysulfides Based on Metal Ions (Cu^{+}, Zn^{2+}, In^{3+}, Ga^{3+}, Ge^{4+}, and Sn^{4+}) with d^{10} Electronic Configuration

2-1. Introduction

Sulfides such as CdS, ZnS, and $(AgIn)_xZn_{2(1-x)}S_2$ exhibit good absorption in the visible light region and function as visible light-driven photocatalysts for water reduction to form H_2 in the presence of sacrificial electron donors (e.g., Na_2S).[1-4] However, they are not stable for the oxidation of water to form O_2 due to dominance of the more favorable oxidation of S^{2-} by photogenerated holes. Recently, $Sm_2Ti_2S_2O_5$ and other $Ln_2Ti_2S_2O_5$ (Ln = Sm, Gd,…) oxysulfides have been demonstrated to catalyze H^+ reduction to form H_2 and water oxidation to form O_2 under visible irradiation in the presence of a sacrificial electron donor (methanol, Na_2S-Na_2SO_3) and acceptor (Ag^+), respectively.[5-7] Oxysulfides have received considerable attention in recent years as materials with interesting physical and structural properties, including paramagnetic susceptibility, transparent p-type semiconductor properties, and layered structures.[8-11] Density functional theory (DFT) calculations suggest that the relatively high stability of oxysulfides compared to sulfides with respect to oxidation reactions is due to differences in the electronic band structure, where the valence band of oxysulfides consists of O 2p and S 3p hybridized orbitals.[5]

In the present study, d^{10} metal ions (Cu^+, Zn^{2+}, In^{3+}, Ga^{3+}, Ge^{4+}, and Sn^{4+}) based oxysulfides which absorb visible light were investigated as potential photocatalytic materials for water splitting under visible light. Although d^{10} metal ion based oxynitride photocatalysts for overall water splitting have been already reported to show good photocatalytic activity,[12-14] d^{10} metal ion based oxysulfides have not been investigated. It was found that In and Ga based oxysulfides showed promising

performance and were thus investigated more in details.

2-2. Experimental Section

2-2-1.Synthesis of Typical Metal Ion (Cu^{+}, Zn^{2+}, In^{3+}, Ga^{3+}, Ge^{4+} and Sn^{4+}) Based Oxysulfides

The oxysulfide materials containing metal ions (Cu^{+}, Zn^{2+}, In^{3+}, Ga^{3+}, Ge^{4+} and Sn^{4+}) were synthesized by solid state reaction. The starting materials were loaded into a quartz tube (outer diameter, 8 mm), then the reactor was evacuated at ambient temperature and heated at 473 K for 5 h to remove adsorbed water. The tube was then sealed, and the mixture was heated to a required temperature. The further details of each synthesis condition are described in the following sections when needed.

(a) $La_3CuS_3O_2$

$La_3CuS_3O_2$ was obtained by the reaction of La_2S_3 (99.9%, High Purity Chemicals) and CuO (98.0%, Kanto Chemical) with the molar ratio of 4:3 in a sealed quartz tube. The sample was heated under vacuum at a rate of 15 K h^{-1} up to 1223 K, and kept at 1223 K for 120 h, and cooled to ambient temperature.[15]

(b) $LaInS_2O$ ($La_5In_3S_9O_3$)

According to the synthesis method demonstrated by Kabbour et al.,[16] $LaInS_2O$ was prepared by heating a mixture of La_2S_3 (99.9%, High Purity Chemicals), La_2O_3 (99.99%, Kanto Chemical, prepared at 1273 K for 5 h at 10 K min^{-1}), and In_2S_3 (99.9%, High Purity Chemicals) with the molar ratio of 1:2:3 in a sealed quartz tube. The sample was heated under vacuum at a rate of 100 K min-1

up to 873-1273 K, and kept for 6-24 h, and then cooled at 100 K h^{-1} to room temperature.

(c) $LaGaS_2O$, La_3GaS_5O and $La_2ZnGa_2S_6O$

$LaGaS_2O$[17] and La_3GaS_5O[18] were synthesized by solid state reactions with starting materials of Ga_2O_3 (99.9%, High Purity Chemicals, pretreated at 1273 K for 5 h at 10 K min^{-1}), La_2O_2S (99.9%, Soekawa Chemical), Ga_2S_3 (99.99%, High Purity Chemicals), and La_2S_3 (99.9%, High Purity Chemicals). $LaGaS_2O$ was prepared from the reaction of La_2O_2S and Ga_2S_3 with the molar ratio of 1:1 in a sealed quartz tube. The sample was heated under vacuum at a rate of 100 K h^{-1} up to 1273 K, and kept for 72 h, and then cooled at 100 K h^{-1} to room temperature. La_3GaS_5O was prepared from the reaction of La_2S_3, Ga_2S_3, and La_2O_2S with the molar ratio of 2:1:1 in a sealed quartz tube. The sample was heated under vacuum at a rate of 100 K h^{-1} up to 1073-1273 K, and kept for 0.5-48 h to give a variety of samples with various particle sizes and surface areas, and then cooled at 100 K h^{-1} to room temperature. Furthermore, $La_2ZnGa_2S_6O$ was prepared from the reaction of La_2S_3, ZnO (99.0%, Kanto Chemical, prepared at 1273 K for 5 h at 10 K min^{-1}), and Ga_2S_3 with the molar ratio of 1:1:1 in a sealed quartz tube. The sample was heated under vacuum at a rate of 100 K min^{-1} up to 1173 K, and kept for 48 h,[19] and then cooled at 100 K h^{-1} to room temperature. As a reference material, $LaGaO_3$ was prepared from the reaction of of La_2O_3 (99.99%, Kanto Chemical, pretreated at 1273 K for 5 h at 10 K min^{-1}) and Ga_2O_3 with a molar ratio of 1:1 in air. The sample was heated at 1173 K for 24 h, cooled to room temperature, re-grinded, and then heated again at 1373 K for 48 h. After a final re-grinding, the sample was annealed at 1623 K for 24 h, and then cooled at 100 K h^{-1} to room temperature (10 K min^{-1}).[20]

(d) $(LaO)_4Ge_{1.5}S_5$

$(LaO)_4Ge_{1.5}S_5$ was prepared from the reaction of La_2O_2S (99.9%, Soekawa Chemical) and GeS_2 (99.9%, Soekawa Chemical) with a molar ratio of 4:3 in a sealed quartz tube.[21] The sample was heated under vacuum at a rate of 100 K h^{-1} up to 1273 K, and kept for 48 h, and then cooled at 100 K h^{-1} to room temperature.

(e) $(LaO)_4Sn_2S_6$

$(LaO)_4Sn_2S_6$ was prepared from the reaction of La_2O_2S (99.9%, Soekawa Chemical) and SnS_2 (99.9%, High Purity Chemicals) with a molar ratio of 2:2 in a sealed quartz tube.[21] The sample was heated under vacuum at a rate of 100 K h^{-1} up to 1273 K, and kept for 48 h, and then cooled to room temperature.

2-2-2. Characterization

The crystal structures of the obtained materials were examined by powder X-ray diffraction (XRD) using a Rigaku Gergerflex RAD-B instrument with Cu Kα radiation. Ultraviolet–visible diffuse reflectance spectra were obtained using a Jasco V-560 spectrometer and were converted from reflection to absorbance by the Kubelka –Munk method. The binding energies were estimated using X-ray photoelectron spectroscopy (XPS) in reference to the C 1s (284.6 eV) due to surface contamination carbon for each sample. The Burner, Emmett, Teller (BET) surface area was measured with a Coulter SA-3100 instrument at 77 K. Particle size and morphology of photocatalyst powder

was observed by scanning electron microscopy (SEM; Hitachi S-4700) and transmission electron microscopy (TEM; JEOL JEM-2010F). Chemical composition was determined by elemental analysis and energy-dispersive X-ray spectroscopy (EDX; Horiba Emax-7000).

2-2-3. Computational Methods

Plane-wave-based density functional method calculations were performed for $LaGaO_3$, $LaGaS_2O$, and La_3GaS_5O using the CASTEP program.[22] The initial crystal parameters indicated in the Inorganic Crystal Structure Database (ICSD)[17,18,20] were optimized by the Broyden, Fletcher, Goldfarb, Shanno (BFGS) method using a starting Hessian that was recursively updated during geometry optimization.[23] Symmetry treatment of atomic positions according to the space group was applied during geometry optimization, and lattice parameters were imposed as general linear constraints on the unit cell. The number of plane waves in the pseudopotential approximation was reduced by replacing core electrons with ultra-soft core potentials,[24] corresponding to valence electronic configurations of $5s^25p^65d^16s^2$ for lanthanum, $3d^{10}4s^24p^1$ for gallium, $3s^23p^4$ for sulfur, and $2s^22p^4$ for oxygen. The DFT calculations were carried out using primitive unit cells of $[LaGaO_3]_6$, $[LaGaS_2O]_4$, and $[LaGaS_5O]_4$. The total numbers of electrons were 252, 168, and 328, and the numbers of occupied molecular orbitals were 126, 84, and 164, respectively. A plane-wave basis set with a kinetic-energy cutoff of 300 eV was employed as implemented in CASTEP. The generalized gradient approximation (GGA)[25] with Perdew, Bruke, Enzerhof (PBE) functional[26] was employed for the DFT exchange-correlation potential in spin-polarized calculations.

2-2-4. Preparation and Deposition of Cocatalyst

Metal cocatalysts (Ni, Ru, Rh, Pd, and Pt) were loaded to the obtained oxysulfides by photodeposition in the presence of the sacrificial electron donors (0.01 M Na_2S, 0.01 M Na_2SO_3) using $Ni(NO_3)_2{\cdot}6H_2O$ (Kanto Chemical; >99.95%), $RuCl_3{\cdot}nH_2O$ (Kanto Chemical; >99.9%), $RhCl_3{\cdot}3H_2O$ (Kanto Chemical; ≥74.0% as $RhCl_3$), $(NH_4)_2PdCl_4$ (Kanto Chemical; ≥37.0% as Pd), and $H_2PtCl_6{\cdot}6H_2O$ (Aldrich; ≥37.50% as Pt). Platinum was also loaded by impregnation from H_2PtCl_6 aqueous solution followed by reduction under H_2 at 473 K for 2 h.

IrO_2 was used as a cocatalyst in attempt to enhance O_2 evolution rates. Colloidal IrO_2 solutiion was prepared by hydrolysis of $Na_2IrCl_6{\cdot}6H_2O$ (Kanto Chemical; >97.0%) in a basic aqueous solution (pH 12). The adsorption of IrO_2 colloids was performed by adding 0.1 g of La_3GaS_5O and 0.24–12.47 cm^3 of colloidal solution (0.11–5.80 mg) to distilled water (50 mL) under vigorous stirring. After stirring for 0.5 h, the transparent supernatant solution was decanted, and the IrO_2-adsorbed sample thus obtained was rinsed three times in distilled water. The sample was then dried at 353 K, in some cases followed by heating in air at 573 K for 1 h. The amount of colloidal IrO_2 adsorbed on the sample was estimated by measuring the 500-700 nm absorbances of the supernatant rinse solutions.

2-2-5. Photocatalytic Reactions

The photocatalytic reaction was carried out in a Pyrex reaction vessel connected to a closed gas

circulation and evacuation system as shown in Figure 2-1. The photocatalyst powder was dispersed in aqueous solutions by a magnetic stirrer in the Pyrex reaction vessel. Photoreduction of H^+ to H_2 and photooxidation of H_2O to O_2 in the presence of a sacrificial electron donors or acceptors were examined as test photoreactions. H_2 evolution was typically examined in 200 mL aqueous solution containing 0.1 g of catalyst and sacrificial electron donors (0.01 M Na_2S-Na_2SO_3). The photooxidation of water to O_2 was performed in 200 mL of 0.01 M $AgNO_3$ solution (Ag^+ : sacrificial electron acceptor) containing 0.1 g catalyst and 0.2 g La_2O_3 powder. In the presence of La_2O_3, the pH of the solution during the photoreaction is buffered at pH = 8-9 by the dissolution of La_2O_3 or $La(OH)_3$. To remove air from the reactor, the solution was evacuated several times and then irradiated with visible light ($\lambda \geq 420$ nm) through a cut-off filter (HOYA, L42) from a 300 W Xe lamp (ILC technology; CERMAX LX-300). The amount of evolved H_2 or O_2 was determined using a on-line gas chromatography (Shimadzu; GC-8A, MS-5A column, TCD, Ar carrier). The number of photons reaching the solution was measured with a Si photo-diode. Quantum efficiencies (Φ) were calculated using the following equation:

$$\Phi(\%) = \frac{\text{number of reacted electrons}}{\text{number of incident photons}} \times 100 = \frac{\text{number of evolved molecules}\,(H_2 \text{ or } O_2) \times (2 \text{ or } 4)}{\text{number of incident photons}} \times 100$$
$$= \frac{AR}{I} \times 100$$

A, R, and I represent the coefficients based on the reactions (H_2 evolution: 2, O_2 evolution: 4), the H_2 or O_2 evolution rate (mol h^{-1}) and the rate of absorption of incident photons, respectively. Here, Φ is the apparent quantum efficiency because we assume that all incident photons are absorbed by the suspension.

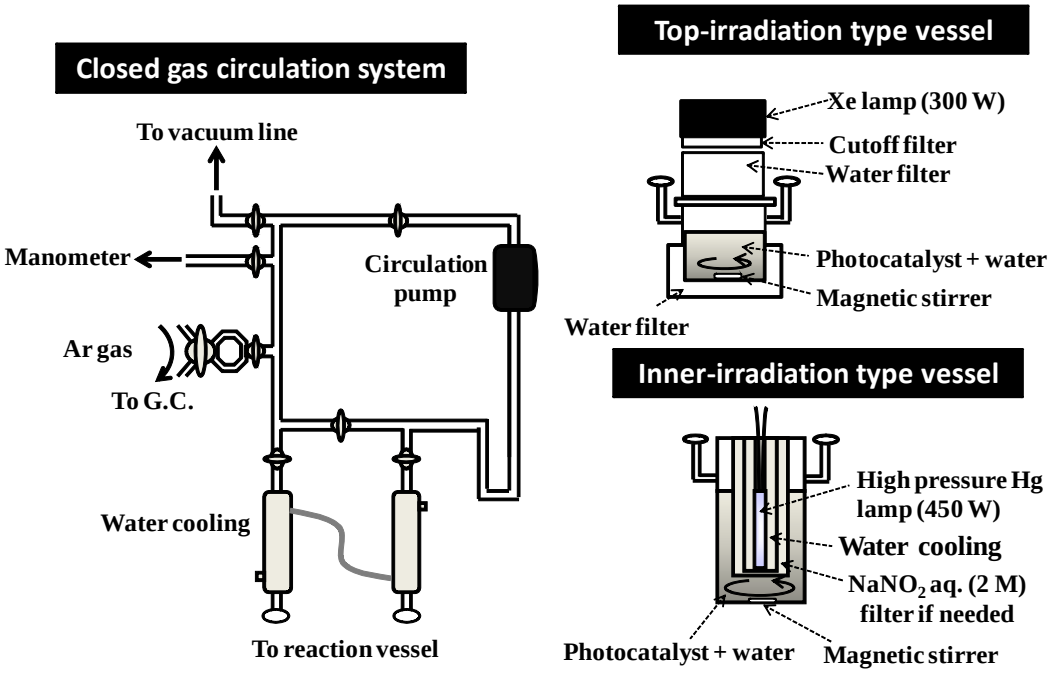

Figure 2-1. Scheme of gas closed circulation system for photocatalytic reaction system

2-2-6. Photoelectrochemical Measurements

Some oxysulfide electrodes were fabricated by spreading viscous slurry of the obtained powder on fluorine-doped tin oxide (FTO) transparent conductive glass (ca. 20 Ω; Asahi Glass). Before spreading the slurry, the substrates were ultrasonicated in acetone and then distilled water. The slurry consisted of the as-prepared sample (0.1 g), water (1 cm^3), acetylacetone (0.05 cm^3), and a small amount of surfactant (Triton X-100, Aldrich). The electrode (coated area, 1×4 cm^2) was heated in air at 573 K for 1 h in order to remove organic solvent and surfactant and to enhance the attachment of particles to the substrate.

Current–voltage and current–time curves were measured using conventional Pyrex electrochemical cell with a planar side window. The cell consisted of a prepared electrode, a platinum wire as counter electrode (1 mm diameter, 250 mm length), and an Ag/AgCl reference

electrode. Aqueous solutions of 0.1 M Na_2SO_4 or 0.01 M Na_2S–Na_2SO_3 were used as electrolytes, and the pH of the solution was adjusted by adding a small amount of NaOH or H_2SO_4 as necessary. The electrolyte was saturated with argon prior to electrochemical measurements, and the potential of the electrode was controlled via a potentiostat (HZ-5000, Hokuto Denko or SDPS-501C, SYRINX). Irradiation was performed using a 300 W xenon lamp with cut-off filters.

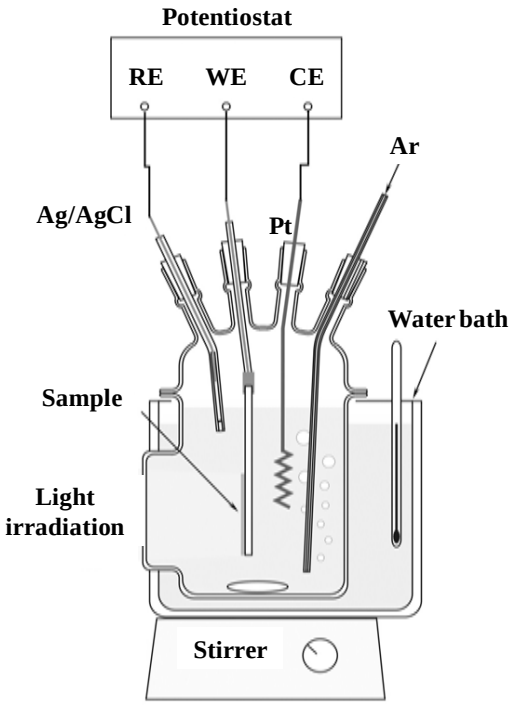

Figure 2-2. Scheme of photoelectrochemical measurement system

2-3. Results and Discussion

2-3-1. Physicochemical Properties

XRD was used to identify the crystal structure and reference patterns were obtained from Inorganic Crystal Structure Database (ICSD)*. The band gap energies were estimated from observed absorption band edge in UV-Vis DRS. The schematic of crystal structures were drawn using the

crystallographic parameter of ICSD.

(a) $La_3CuS_3O_2$

Figure 2-3 (A) compares the XRD patterns of (b) as-prepared $La_3CuS_3O_2$ with (a) reference from ICSD file ($La_3CuS_3O_2$, #96438).[15] The obtained sample consisted of $La_3CuS_3O_2$ as main phase and LaCuOS as sub-phase. The other peak at 2θ=22° was unidentified. UV-Vis DR spectrum of the obtained sample is shown in Figure 2-3 (B). The absorption edge is observed at 650 nm and the band gap energy is estimated to be 1.9 eV.

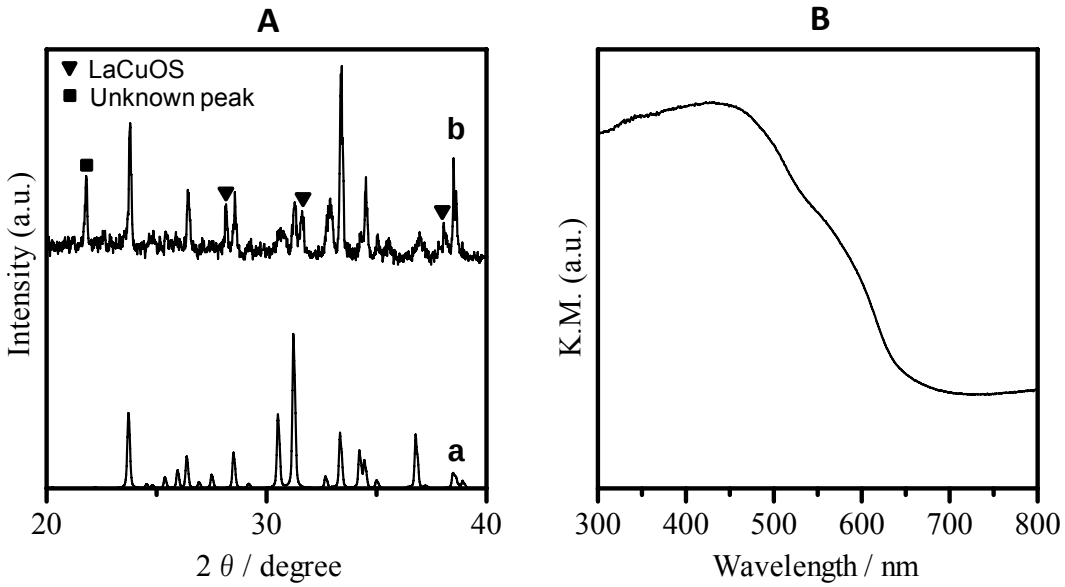

Figure 2-3. (A) XRD patterns for (a) ICSD file ($La_3CuS_3O_2$, #96438) and obtained sample (1223 K, 120 h) and (B) UV-Vis DR spectrum for $La_3CuS_3O_2$.

(b) $La_5In_3S_9O_3$($LaInS_2O$)

Figure 2-4 (A) compares the XRD patterns of (b) as-prepared sample with (a) reference from $LaInS_2O$ reported by Kabbour et al.[16] Most of the crystalline peaks produced by the present samples matched with those for the reported peaks.[16] However, the exact crystal structure and XRD pattern

for $LaInS_2O$ phase are unknown. The obtained XRD pattern shows minor peaks assignable to In_2O_3. Therefore, the oxysulfide obtained by this preparation procedure is considered to lack In from $La_5In_3S_9O_3$ stoichiometry and to contain other minor phases, such as $La_{1.33}In_{1.33}S_4$,[27] and $LaIn_2S_4$.[28] $La_5In_3S_9O_3$ is a metastable phase and could be obtained in an overall In-rich (La:In = 1:1) system.

Figure 2-4 (B) shows the UV–vis diffuse reflectance spectra for the present La-In oxysulfide and $LaInO_3$. The absorption edge of the La-In oxysulfide is shifted to the longer wavelengths (480 nm) than that of $LaInO_3$. The band-gap energy is estimated to be ca. 2.6 eV based on the absorption band edge. As in the case of $Sm_2Ti_2S_2O_5$,[5] the reason for visible light response is that the top of the valence band (E_{VB}) of the La-In oxysulfide may be located at a more negative potential than the E_{VB} of $LaInO_3$ due to the incorporation of S^{2-} and hybridization of S 3p and O 2p.

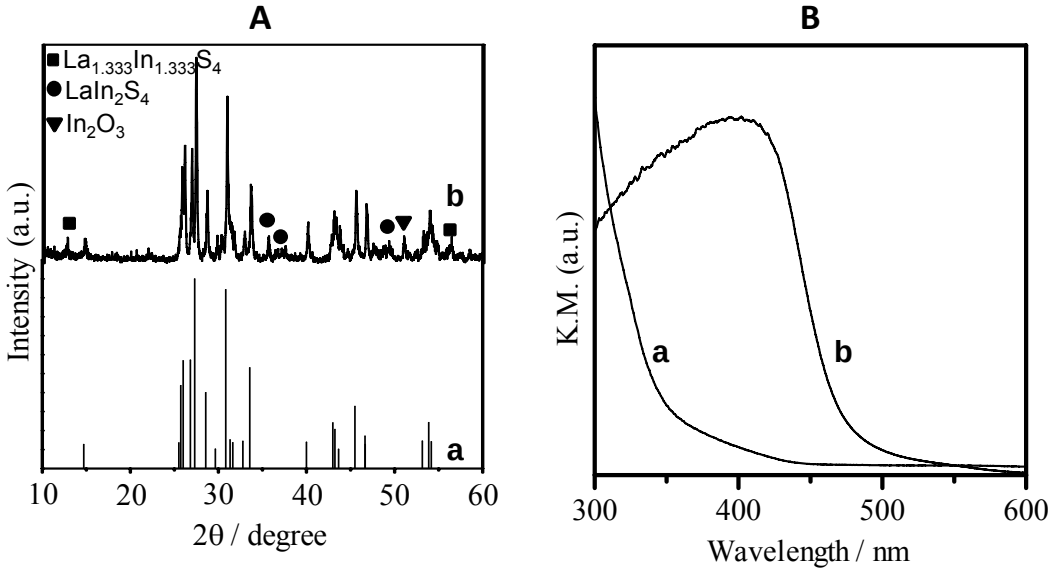

Figure 2-4. (A) XRD patterns for (a) $LaInS_2O$ reported by Kabbour et al. and (b) obtained sample (1073 K, 12 h) and (B) UV-Vis DR spectrum for La-In based oxysulfide.

(c) $LaGaS_2O$ and La_3GaS_5O

Figure 2-5 (A) compares the XRD patterns of (b) as-prepared $LaGaS_2O$ with (a) a reference obtained from ICSD file ($LaGaS_2O$, #2238).[17] The obtained sample consisted of $LaGaS_2O$ as main phase and La_2O_3 as sub-phase. Figure 2-5 (B) compares the XRD patterns of (b) as-prepared La_3GaS_5O with (a) a reference obtained from ICSD file (La_3GaS_5O, #38067).[18] A small amount of the unreacted precursors (La_2S_3 and La_2O_2S) was observed in the XRD pattern of La_3GaS_5O prepared at 1073 K for 24 h. The peak associated with the impurity phase of La_2S_3 species weakens with increasing treatment temperature. However, the peaks attributable to La_2O_2S phase was observed even for the samples treated at 1273 K for 48 h. A single-phase La_3GaS_5O powder sample thus could not be obtained in this study, containing a small amount of La_2S_2O. La_2O_2S is not responsive to visible irradiation and thus is not expected to affect the electrochemical or photocatalytic properties of the La_3GaS_5O compound. Figure 2-6 shows the schematic structure of La-Ga based materials. $LaGaO_3$ has a distorted perovskite structure with tilted GaO_6 octahedra resulting in an orthorhombic unit cell,[20] while $LaGaS_2O$ has a KVO_3-type structure[17] and La_3GaS_5O has a shear structure,[18] both with an orthorhombic unit cell.

UV-Vis DR spectra results for $LaGaO_3$, $LaGaS_2O$, and La_3GaS_5O are shown in Figure 2-7 (A). Figure 2-7 (B) shows photographs of La-Ga based materials as a reference. The estimated absorption band edges are ca. 280, 420, and 540 nm, and the samples had colors of white, light yellow, and yellow, respectively. The band-gap energies thus decrease in the sequence $LaGaO_3$ (4.4 eV) > $LaGaS_2O$ (3.0 eV) > La_3GaS_5O (2.3 eV), indicating that the band-gap energy decreases with sulfur

content.

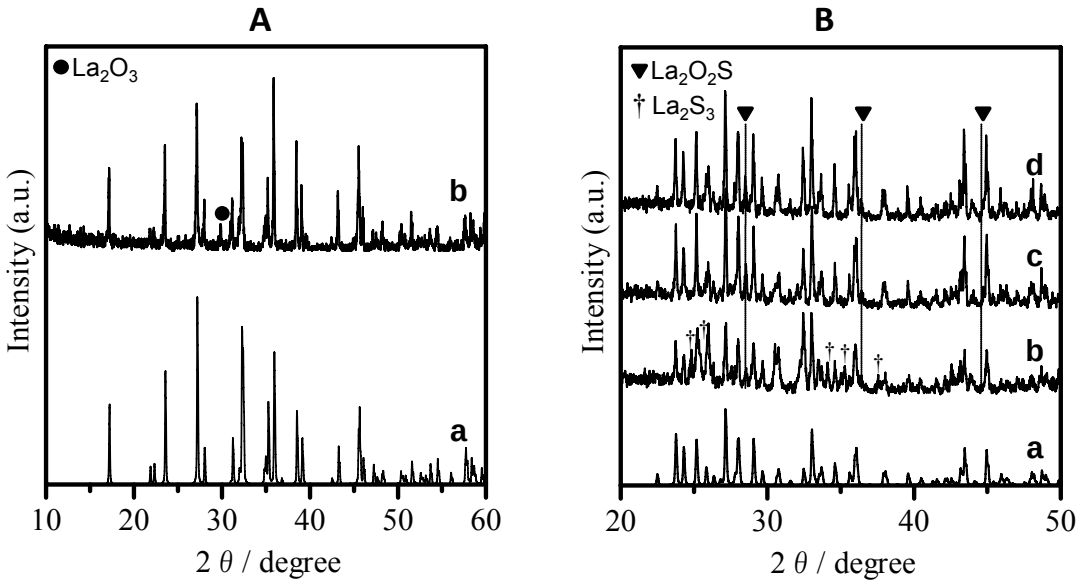

Figure 2-5. (A) XRD patterns for (a) ICSD file ($LaGaS_2O$, #2238) and (b) obtained sample (1273 K, 72 h) and (B) XRD patterns for $LaGaS_2O$ (a) ICSD (La3GaS5O, #38067), (b) obtained sample (1073 K, 24 h), (c) obtained sample (1173 K, 24 h), and (d) obtained sample (1273 K, 24 h).

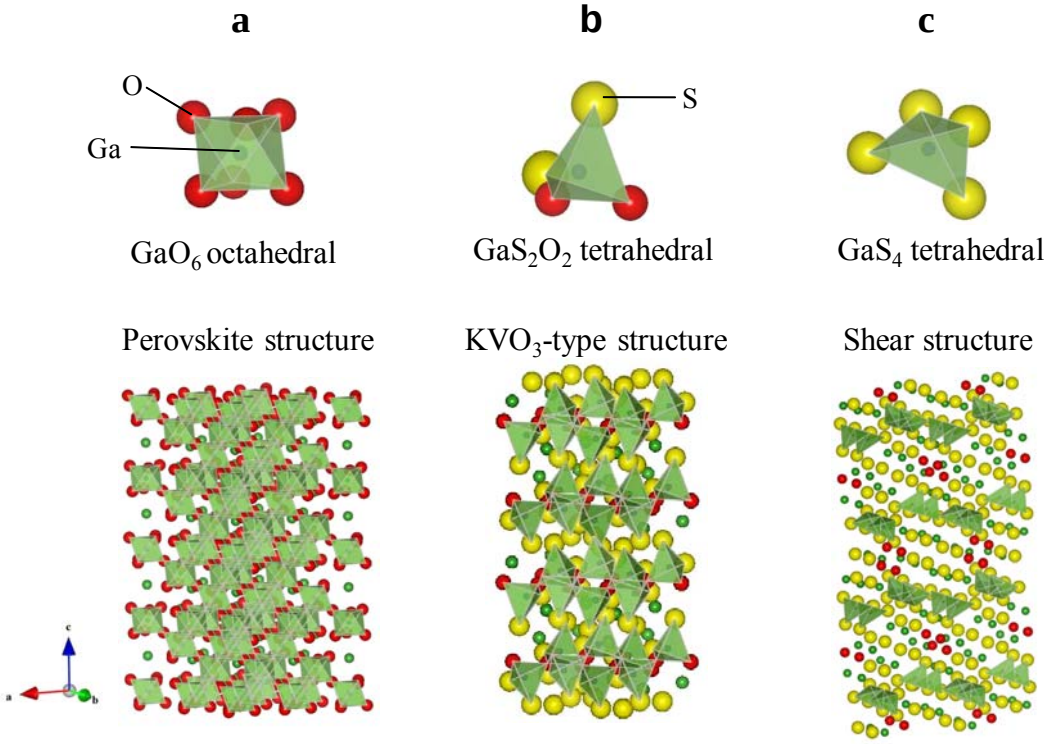

Figure 2-6. Schematic structure of La-Ga based materials (a) $LaGaO_3$, (b) $LaGaS_2O$, and (c) La_3GaS_5O

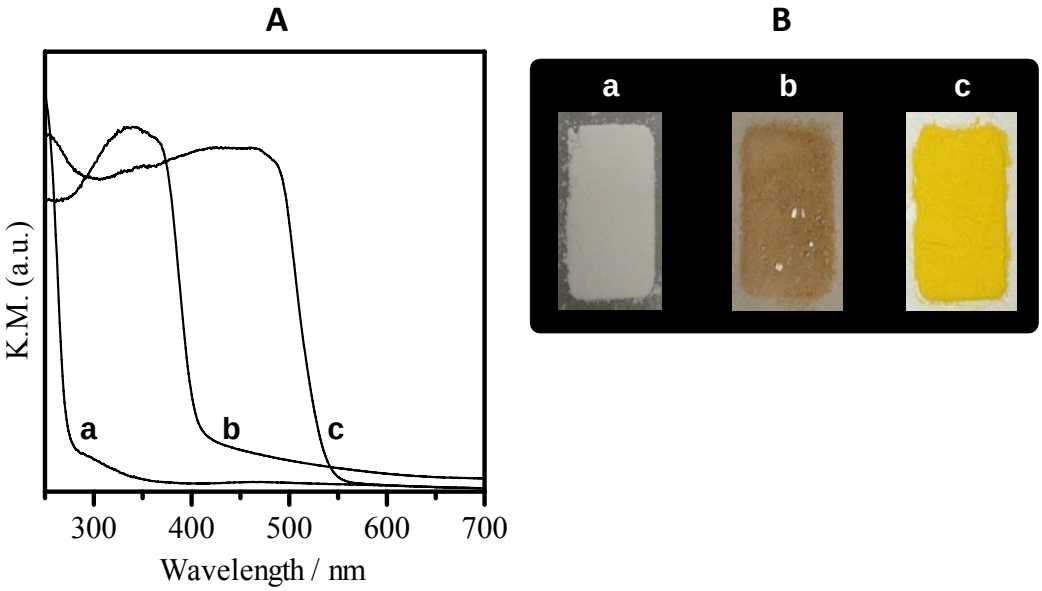

Figure 2-7. (A) UV-Vis DR spectra for (a) $LaGaO_3$, (b) $LaGaS_2O$, and (c) La_3GaS_5O.

(d) $La_2ZnGa_2S_6O$

Figure 2-8 (A) compares the XRD patterns of (b) as-prepared $La_2ZnGa_2S_6O$ with (a) a reference obtained from ICSD file ($La_2ZnGa_2S_6O$, #61044).[19] The obtained sample consisted of $La_2ZnGa_2S_6O$ as a main phase and La_3GaS_5O as a minor phase. UV-Vis DR spectrum of the obtained sample is shown Figure 2-3 (B). The absorption edge of $La_2ZnGa_2S_6O$ is at 420 nm with a shoulder up to 500 nm, and the band gap energy is estimated to be 3.0 eV (or 2.5 eV).

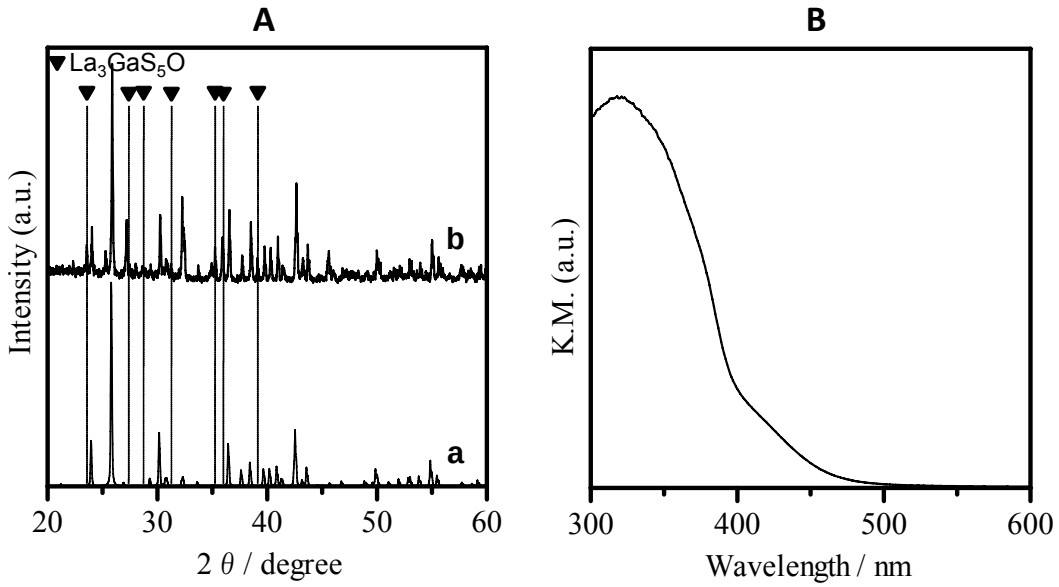

Figure 2-8. (A) XRD patterns for (a) ICSD file ($La_2ZnGa_2S_6O$, #61044) and (b) obtained sample (1273 K, 24 h) and (B) UV-Vis DR spectrum for $La_2ZnGa_2S_6O$.

(e) $(LaO)_4Ge_{1.5}S_5$

XRD patterns for as-prepared $(LaO)_4Ge_{1.5}S_5$ are shown in Figure 2-9 (A). The exact assignment of the peaks has not been employed due to lack of the reference patterns for $(LaO)_4Ge_{1.5}S_5$. UV-Vis DR spectrum of the obtained sample is shown Figure 2-9 (B). The absorption edge of the sample is at 370 nm, and the band gap energy is estimated to be 3.4 eV.

(f) $(LaO)_4Sn_2S_6$

Figure 2-10 (A) compares the XRD patterns of (b) as-prepared $(LaO)_4Sn_2S_6$ with (a) a reference obtained from ICSD file ($(LaO)_4Sn_2S_6$, #48199).[21] X-ray analysis showed that the obtained sample consisted of $(LaO)_4Sn_2S_6$ as main phase and SnS_2 as impurity phase. UV-Vis DR spectrum of the obtained sample is shown in Figure 2-10 (B). The absorption edge of $(LaO)_4Sn_2S_6$ is at 460 nm, and the band gap energy is estimated to be 2.7 eV.

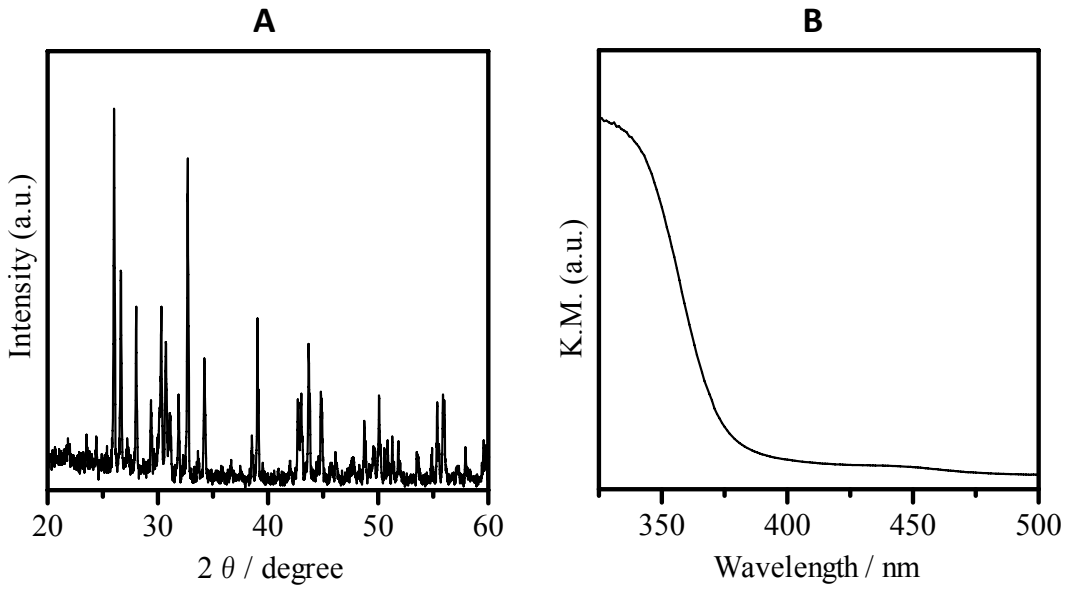

Figure 2-9. (A) XRD patterns for $(LaO)_4Ge_{1.5}S_5$ sample obtained in this study (1273 K, 48 h) and (B) UV-Vis DR spectrum for La-Ge based oxysulfide.

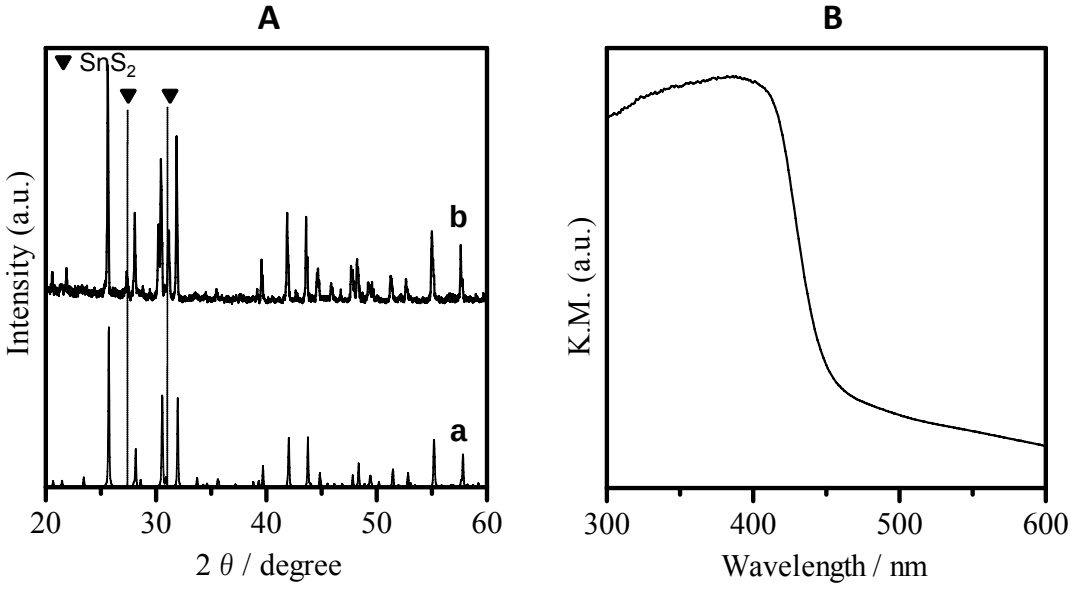

Figure 2-10. (A) XRD patterns for (a) ICSD file ($(LaO)_4Sn_2S_6$, #48199) and (b) obtained sample (1273 K, 48 h) and (B) UV-Vis DR spectrum for $(LaO)_4Sn_2S_6$.

2-3-2. Band Structure Calculation

The author estimated the band structure of $LaGaO_3$, $LaGaS_2O$, and La_3GaS_5O through plane-wave-based DFT calculations and examined the cause of visible light response. The Plane-wave-based density function theory (DFT) calculations showed that the valence band (E_{VB}) of $Sm_2Ti_2S_2O_5$ is made up of the O2p and S3p hybridized orbitals and the conduction band (E_{CB}) consists of Ti3d. As a result, $Sm_2Ti_2S_2O_5$ has a smaller band gap energy (≈2.1 eV) compared with that of $Sm_2Ti_2O_7$ (≈3.5 eV). Figure 2-11 shows the band structure and density of states (DOS) for $LaGaO_3$. The energy level of the band structure and the DOS obtained by plane-wave DFT calculations do not provide absolute values because the top end of the occupied orbitals was set as zero. The valence band region from –7 to 0 eV is mainly composed of O 2p orbitals, although the Ga 4s4p orbitals also have a small but non-negligible contribution. The occupied bands mainly consist of La 5s (#1–6), O 2s + La 5p (#7–24), La 5p (#25–42), Ga 3d (#43–72), Ga 4s + O 2p (#73–78), and O 2p (#79-126) orbitals in the order of increasing energy. The unoccupied bands are composed of empty La 5d and Ga 4s4p orbitals. The band-gap transition from the top of the valence band (highest occupied molecular orbital; HOMO) to the bottom of the conduction band (lowest unoccupied molecular orbital; LUMO) mainly occurs from the filled O 2p orbitals to the empty La 5d and Ga 4s orbitals. Figures 2-12 and 2-13 show the band structures and DOS for $LaGaS_2O$ and La_3GaS_5O. The occupied bands in the valence band region mainly consist of Ga 4s, Ga 4p, O 2p, and S 3p orbitals for both oxysulfides. The main orbitals of the conduction band are La 5d and Ga 4s4p, as determined for $LaGaO_3$. The order of the calculated band gaps ($LaGaO_3$, 3.74 eV; $LaGaS_2O$,

2.20 eV; La_3GaS_5O, 1.13 eV) is consistent with the order determined from the DRS results in Fig. 2 (i.e., 4.4, 3.0, and 2.3 eV). The valence bands of $LaGaS_2O$ and La_3GaS_5O involve overlap of the O 2p and S 3p orbitals, where the higher-energy region mainly consists of S 3p orbitals and the lower-energy region is mainly comprised of O 2p orbitals. The contribution of S 3p to the top of the valence band is greater for La_3GaS_5O due to the higher sulfur content.

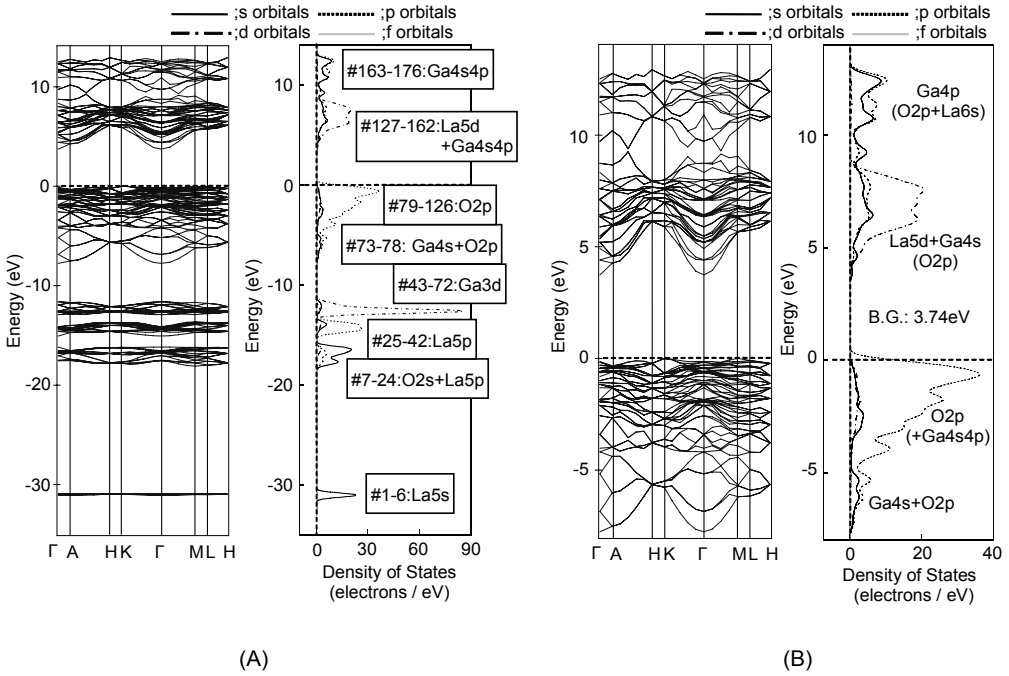

Figure 2-11. Band structure and density of states for $[LaGaO_3]_6$ unit cell: (A) Full scale, and (B) Magnified.

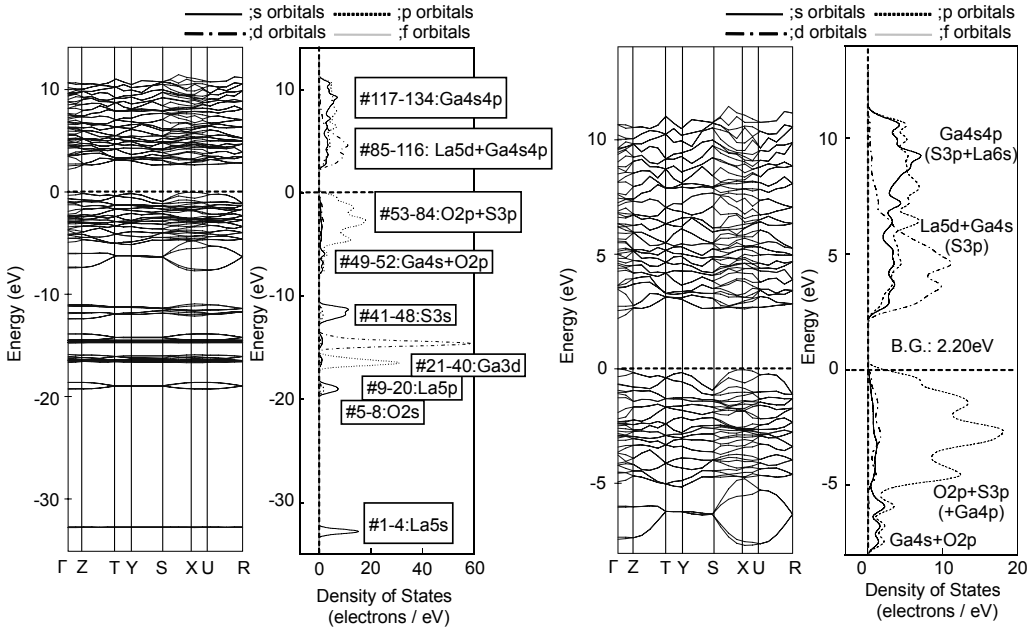

Figure 2-12. Band structure and density of states for $[LaGaS_2O]_4$ unit cell: (A) Full scale, and (B) Magnified.

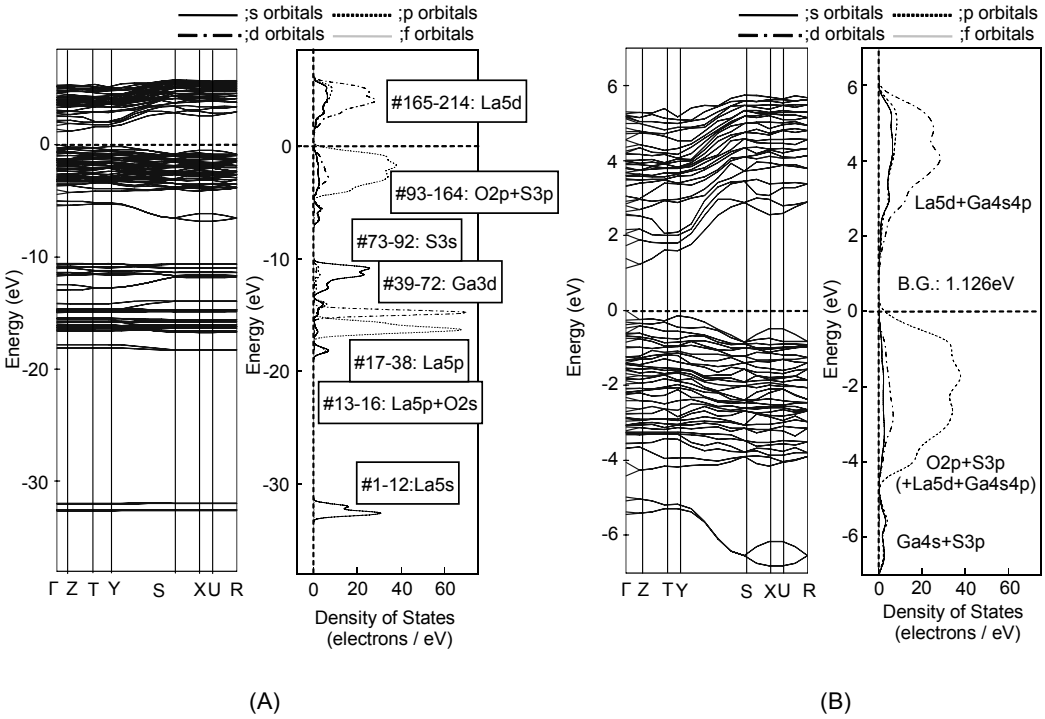

Figure 2-13. Band structure and density of states for $[La_3GaS_5O]_4$ unit cell: (A) Full scale, and (B) Magnified.

2-3-3. Photocatalytic Reactions

Table 2-1 lists the photocatalytic activities of d^{10} metal ions (Cu^{+}, Zn^{2+}, In^{3+}, Ga^{3+}, Ge^{4+}, and Sn^{4+}) based oxysulfides for the reduction of H^{+} to H_2 and oxidation of H_2O to O_2 in the presence of sacrificial electron (Na_2S-Na_2SO_3) donor or acceptor (Ag^{+}). O_2 evolution was examined in a basic solution (pH = 8) buffered with La_2O_3. In the reaction, the rate of O_2 evolution decreased with reaction time due to the deposition of metallic silver on the surface of the catalyst, effectively shielding the catalyst from incident light. Therefore, the initial rate of O_2 evolution was regarded to determine the photocatalytic activity. In d^{10} metal ions (Cu^{+}, Zn^{2+}, In^{3+}, Ga^{3+}, Ge^{4+}, and Sn^{4+}) based oxysulfides, $La_3CuS_3O_2$, $La_5In_3S_9O_3$, La_3GaS_5O, La_2ZnGaS_6O, and $(LaO)_4Sn_2S_6$ have energy gap adequate to absorb visible light, but $LaGaS_2O$ and $(LaO)_4Ge_{1.5}S_5$ respond to only UV light. H_2 and O_2 evolution were not observed for $La_3CuS_3O_2$ and $(LaO)_4Sn_2S_6$. $La_3CuS_3O_2$ and the $(LaO)_4Sn_2S_6$ was soluble in water. La_2ZnGaS_6O and $(LaO)_4Ge_{1.5}S_5$ evolved H_2 but did not function for oxidation of water to O_2. The results suggested that La_2ZnGaS_6O and $(LaO)_4Ge_{1.5}S_5$ are not stable in aqueous solution under irradiation and undergo anodic dissolution as well as Chalcogenide materials such as CdS and ZnS. $La_5In_3S_9O_3$ and La_3GaS_5O absorb visible light and are demonstrated to evolve H_2 or O_2 from water containing sacrificial reagents. Therefore, $La_5In_3S_9O_3$ and La_3GaS_5O were furthermore examined as a photocatalyst candidate for overall water splitting reaction.

Table 2-1. Photocatalytic activity of d^{10} metal ions (Cu^{+}, Zn^{2+}, In^{3+}, Ga^{3+}, Ge^{4+}, and Sn^{4+}) based oxysulfides

photocatalyst	B. G. / eV	steady rate of H_2 evolution[a] / μmol h^{-1}	initial rate of O_2 evolution[b] / μmol h^{-1}
$La_3CuS_3O_2$	1.9	0	0
$La_5In_3S_9O_3$	2.6	11	2
$LaGaS_2O$*	3.0	10	0
La_3GaS_5O	2.3	45	0.5
La_2ZnGaS_6O	3.0 (2.5)	24	0
$(LaO)_4Ge_{1.5}S_5$*	3.4	1	0
$(LaO)_4Sn_2S_6$	2.7	0	0

a. Catalyst (0.1 g): Pt (1 wt%) - loaded sample, Reactant solution (200 mL): Na_2S (0.01 M) and Na_2SO_3 (0.01 M) /distilled water, Light source: 300 W Xe Lamp with a cutoff filter ($\lambda > 420$ nm).
b. Catalyst (0.1 g), Reactant solution (200 mL): $AgNO_3$ (2 mmol) and La_2O_3 (0.2 g) / distilled water, Light source: 300 W Xe Lamp with a cutoff filter ($\lambda > 420$ nm)
*. Irradiation wavelength: $\lambda > 300$ nm

(1) $LaInS_2O$ ($La_5In_3S_9O_3$)

The effects of cocatalysts with other metals than Pt on H_2 evolution rates were investigated as shown in Table 2-2. Ni, Cu, Ru, Rh, Pd, Ir, and Pt cocatalysts were deposited by conventional wet impregnation method and treated at 573 K for 1 h, or photodeposited under visible light irradiation (except for RuO_2). The $LaInS_2O$ showed photocatalytic activity for H_2 evolution without a cocatalyst (0.6 μmol h^{-1}). Rates of the photocatalytic H_2 evolution were enhanced in the presence of the metals investigated, except for the Ni sample. The Pt loaded photocatalyst showed the highest photocatalytic activity.

Table 2-2. Effect of cocatalyst loaded La-In oxysulfide photocatalysts on water splitting

cocatalyst	rate of H_2 evolution / μmol h^{-1}
—	0.6
Ni	0.2
Cu	1.1
Ru	4.8
RuO_2	-
Rh	2.1
Pd	4.5
Ir	1.5
Pt	11

Catalyst (0.1 g): cocatalyst (1 wt%) - loaded sample, Reactant solution (200 mL): Na_2S (0.01 M) and Na_2SO_3 (0.01 M) /distilled water, Light source: 300 W Xe Lamp with a cutoff filter ($\lambda > 420$ nm).

Figure 2-14 shows the time course of repeated H_2 evolution over La-In oxysulfide loaded with 1.0 wt% Pt under visible-light irradiation ($\lambda > 420$ nm) in the presence of Na_2S–Na_2SO_3. The reaction system was evacuated every 5 h. In the early stage of the reaction (2 h), H_2PtCl_6 was reduced to Pt as an H_2 evolution promoter on the catalyst surface. The rate of H_2 evolution remained essentially stable after this induction period. The XRD pattern of the catalyst after the H_2 evolution reaction was the same as that before the reaction. The Pt-loaded La-In oxysulfide therefore functions as a stable photocatalyst for the reduction of H^+ to H_2 under visible-light irradiation.

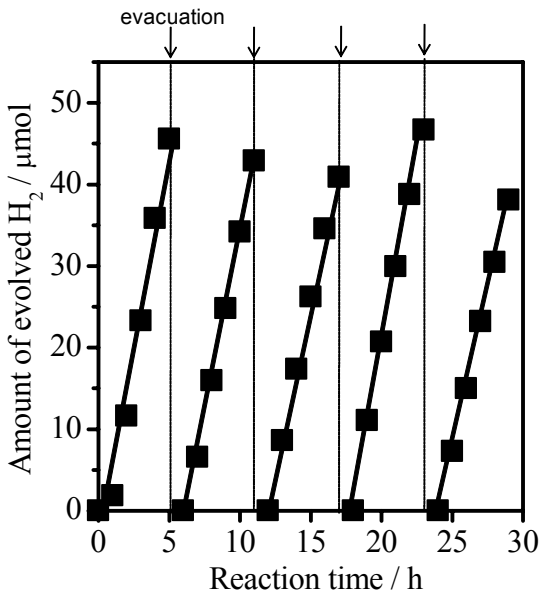

Figure 2-14. Time course of repeated H_2 evolution over La-In oxysulfide (Catalyst (0.1 g): Pt (1 wt%)-loaded sample, Reactant solution (200 mL): Na_2S (0.01 M) and Na_2SO_3 (0.01 M) /distilled water, Light source: 300 W Xe Lamp with a cutoff filter ($\lambda > 420$ nm).)

Figure 2-15 shows the time courses of O_2 evolution over bare and IrO_2-loaded La-In oxysulfide, and over CdS for comparison. O_2 evolution was not observed over CdS but CdS was photodecomposed CdS by photogenerated holes. On contrary, over the bare La-In oxysulfide, O_2 evolution was observed immediately after the start of irradiation. Loading with 2 wt% IrO_2 increased the evolution rate by approximately three-fold, indicating that IrO_2 is an effective O_2 evolution promoter for the La-In oxysulfide. After an initial period (1 h), La-In oxysulfide in $AgNO_3$ solution turned gray due to the deposition of metallic silver on the surface of the catalyst, resulting in the rate of O_2 evolution decreased with time.

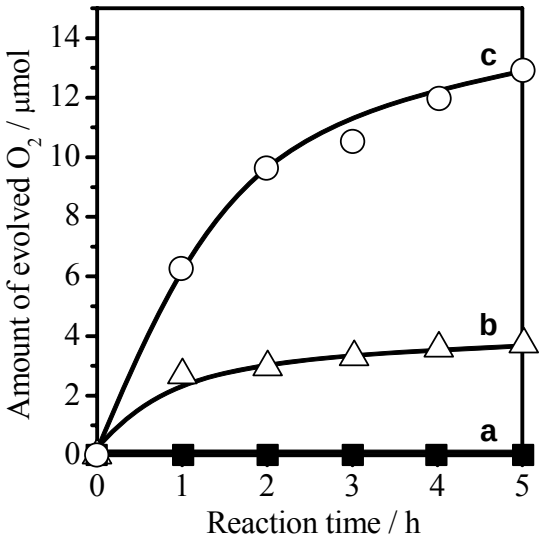

Figure 2-15. Time course of O_2 evolution over (a) CdS, (b) La-In oxysulfide, and (c) 2 wt% IrO_2 / La-In oxysulfide under visible light irradiation ($\lambda > 420$ nm) (Catalyst (0.1 g), Reactant solution (200 mL): $AgNO_3$ (2 mmol) and La_2O_3 (0.2 g) / distilled water, Light source: 300 W Xe Lamp with a cutoff filter ($\lambda > 420$ nm)) The lines B and C were drawn freehand.

Figure 2-16 shows the relationship between the H_2 and O_2 evolution rates and the cutoff wavelength of incident light. The steady rate of H_2 evolution and the initial rate of O_2 evolution decreased with increasing cutoff wavelength, confirming the position of the absorption edge of the La-In oxysulfide and the procession of these photocatalytic reactions via band-gap transitions. The apparent quantum efficiencies (QE) of H_2 and O_2 for La-In oxysulfide (Figure 2-14 and Figure 2-15) were estimated to be ~0.2 and ~0.1% (7.4×10^{21} photons h^{-1} at 420 nm < λ < 600 nm), respectively, indicating that La-In oxysulfide exhibited superior QE for H_2 evolution and lower QE for O_2 evolution in contrast to those of $Sm_2Ti_2S_2O_5$ [QE: 0.1% (H_2), 0.2% (O_2)].[5] These differences might arise from the fact that E_{CB} of In5s5p orbitals with large dispersion[29] mainly led to the higher QE of

H_2 evolution and the purity of La-In oxysulfide containing sulfide phases influenced the QE for O_2 evolution.

Next, overall water splitting reaction over La-In based oxysulfide was investigated. Table 2-3 shows the photocatalytic activities of La-In oxysulfide loaded with effective cocatalysts for overall water splitting. Overall water splitting reaction did not proceed for all the catalysts investigated, but only negligible amount of H_2 was observed. Even the H_2 produced may be due to the photooxidation of catalysts. The further attempts to load different amount of cocatalysts and to control pH of the solution were not successful to improve photocatalytic reaction rates.

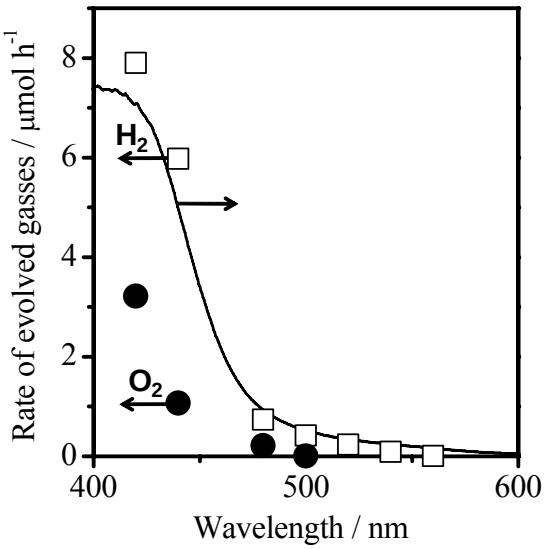

Figure 2-16. Dependence of rate of H_2 and O_2 evolution on cutoff wavelength of incident light, and UV-Vis DR spectrum of La-In oxysulfide, squares denote H_2 evolution and triangles denote O_2 evolution. (H_2 evolution reaction; Catalyst (0.1 g): Pt (1 wt%)-loaded sample, Reactant solution (200 mL): Na_2S (0.01 M) and Na_2SO_3 (0.01 M) / distilled water, Light source: 300 W Xe Lamp with a cutoff filter ($\lambda > 420$ nm). O_2 evolution reaction; Catalyst (0.1 g), Reactant solution (200 mL): $AgNO_3$ (2 mmol) and La_2O_3 (0.2 g) / distilled water, Light source: 300 W Xe Lamp with a cutoff filter ($\lambda > 420$ nm))

Table 2-3. Effect of co-catalyst loaded La-In oxysulfide photocatalyst on water splitting

cocatalyst	activity / μmol h^{-1}	
(loading amount / wt%)	H_2	O_2
—	1.3	0
NiO (1)	0.3	0
RuO_2 (1)	2.4	0
NiO(1)-Cr_2O_3(1)	0.1	0
Rh(3)-Cr_2O_3(1)	0.8	0

a. Catalyst (0.3 g): cocatalyst - loaded sample, Reactant solution (400 mL): distilled water, Light source: 450 W high pressure Hg Lamp (λ > 290 nm).

(2) La_3GaS_5O ($LaGaO_3$, $LaGaS_2O$)

Table 2-4 lists the steady-state H_2 evolution rates using La_3GaS_5O prepared at different temperatures (1073, 1173, and 1273 K) and loaded with 1.0 wt% Pt. The specific surface areas measured by N_2 adsorption at 77 K are also listed. Both the H_2 evolution rate and BET specific surface area decrease with increasing preparation temperature. The reduction in photocatalytic activity is therefore attributable to the decrease reaction site for H_2 evolution with decreasing surface area. The sample prepared at 1073 K for 24 h, which displayed the highest photocatalytic activity, was further tested under various reaction conditions.

Table 2-5 shows the steady-state H_2 evolution rate on La_3GaS_5O loaded with various metals as cocatalysts for H_2 evolution. Cocatalysts were photodeposited from metal complexes in the reaction solutions as indicated in Table 2-5 resulting in metal nanoparticles on the surface of the La_3GaS_5O powder. For comparison, Pt/La_3GaS_5O prepared by wet impregnation was also examined. H_2 was evolved under irradiation for all samples, even for the samples which a cocatalyst was not loaded.

The rate of H_2 evolution increased in the order of cocatalysts: Ru > Pt >> Rh > Pd > Ni. The rates of H_2 evolution using the ruthenium- and platinum-loaded samples increased with increasing metal loading, reaching a maximum of 106 μmol h^{-1} (Ru) or 108 μmol h^{-1} (Pt) at 3.0 wt%. Loading with other metals at more than 1.0 wt% did not result in any further increase in H_2 evolution rate. The La_3GaS_5O sample loaded with 3.0 wt% Pt achieved the highest H_2 evolution rate of the samples examined in the present study, corresponding to an apparent quantum efficiency for H_2 evolution of ca 2.5% (5.3×10^{21} photons h^{-1} at 420 nm < λ < 540 nm).

Table 2-4. Properties and rate of H_2 evolution for La_3GaS_5O synthesized at various temperatures

synthesis temperature / K	BET surface area / m^2 g^{-1}	rate of H_2 evolution / μmol h^{-1}
1073	2.0	45.1
1173	0.7	35.6
1273	0.2	13.3

Catalyst (0.1 g): Pt (1 wt%) - loaded sample, Reactant solution (200 mL): Na_2S (0.01 M) and Na_2SO_3 (0.01 M) /distilled water, Light source: 300 W Xe Lamp with a cutoff filter (λ > 420 nm).

Table 2-5. Photocatalytic H_2 evolution rates over La_3GaS_5O loaded with various cocatalysts

cocatalyst	Precursor	Rate of H_2 evolution / μmol h^{-1}
—	—	0.2
Ni	$Ni(NO_3)_2\cdot6H_2O$	2.4
Ru	$RuCl_3\cdot3H_2O$	80.7
Rh	$Na_3RhCl_6\cdot2H_2O$	6.4
Pd	$(NH_4)_2PdCl_4$	4.0
Pt	$H_2PtCl_6\cdot6H_2O$	54.1

Catalyst (0.1 g): cocatalyst (1 wt%) - loaded sample, Reactant solution (200 mL): Na_2S (0.01 M) and Na_2SO_3 (0.01 M) /distilled water, Light source: 300 W Xe Lamp with a cutoff filter (λ > 420 nm).

O_2 evolution rates were measured for La_3GaS_5O by conducting photocatalytic reactions in the presence of Ag^+ under visible irradiation. Figure 2-17 shows time courses of O_2 evolution. The discovery of the O_2 evolution activity of La_3GaS_5O under visible light reinforces the potential of oxysulfide compounds as visible light-driven photocatalysts. However, the O_2 evolution rate using as-prepared La_3GaS_5O remains much lower than that achieved by $Sm_2Ti_2S_2O_5$ (22 μmol h^{-1})[1] under visible light.

Figure 2-17 also shows the O_2 evolution rates over IrO_2-loaded La_3GaS_5O. The evolution rates are higher than achieved by the as-prepared La_3GaS_5O, indicating that the IrO_2 colloid functions as an effective O_2 evolution promoter for La_3GaS_5O. Interestingly, the IrO_2/La_3GaS_5O sample post-treated at 573 K exhibits a steady rate of O_2 evolution, whereas the evolution rate over the untreated IrO_2/La_3GaS_5O sample gradually decreased with time. Heat treatment of IrO_2-loaded La_3GaS_5O therefore has a positive effect on the stability of photocatalytic activity.

Figure 2-18 shows SEM and TEM images of the La_3GaS_5O and IrO_2/La_3GaS_5O powders. The La_3GaS_5O sample consists of aggregates and sintered particles with flat surfaces. The loaded IrO_2 nanoparticles (< ca. 50 nm) are uniformly dispersed on the La_3GaS_5O particle surfaces. Without post-treatment, the IrO_2 particles are porous and loosely packed. The following heat treatment 573 K for 1 h aggregates of IrO_2 particles (ca. 1 nm) are transformed into dense and sintered IrO_2 particles of ca. 20 nm in size. The post calcination beyond 573 K decreased O_2 evolution rate due to decomposition of La_3GaS_5O. The rate of O_2 evolution increased with increasing loaded IrO_2 colloid, reaching a maximum at 2 wt%, and decreased with further deposition of IrO_2 colloid beyond 2 wt%.

Iridium metal clusters (average particle size, ca. 1 nm) supported on SiO_2 have been reported to form a tetragonal bulk oxide with a rutile structure upon heating at above 573 K under a flow of 1%O_2/He based on TEM and selected-area electron diffraction (SAED) observations.[30] The number of oxide ions coordinated around iridium ions has also been found to be changed by treatment between 623 K and 673 K.[31] The observed change in morphology for the loading IrO_2 colloid is therefore considered to reflect the sintering of small IrO_2 particles (ca. 1 nm) at 573 K. As the O_2 evolution rates over the untreated and post-treated IrO_2/La_3GaS_5O samples were similar, both porous IrO_2 and sintered IrO_2 appear to function as effective O_2 evolution promotion sites. However, the O_2 evolution rate over the porous IrO_2 decreased with reaction time, indicating a progressive loss of the cocatalyst effect. This suggests that IrO_2 is desorbed from the surface to solution or the deactivation of IrO_2 during the reaction.

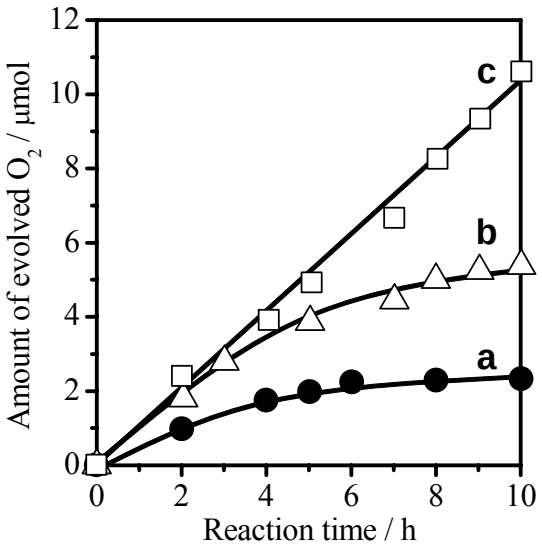

Figure 2-17. Time course of O_2 evolution over La_3GaS_5O loaded with 2 wt% IrO_2 (Catalyst (0.1 g), Reactant solution (200 mL): $AgNO_3$ (2 mmol) and La_2O_3 (0.2 g) / distilled water, Light source: 300 W Xe Lamp with a cutoff filter (λ > 420 nm)) (a) La_3GaS_5O, (b) IrO_2/La_3GaS_5O, (c) post-treated IrO_2/La_3GaS_5O

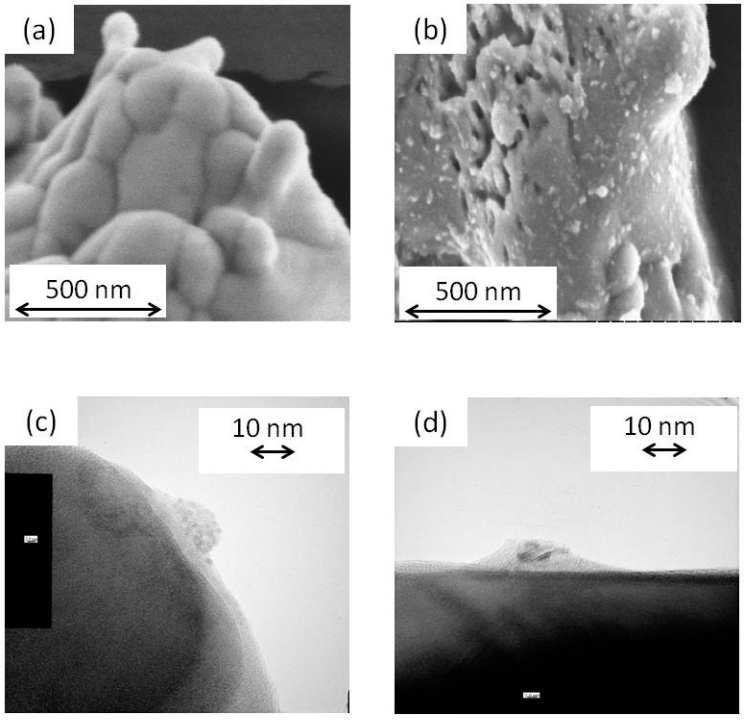

Figure 2-18. SEM images of (a) La_3GaS_5O and (b) IrO_2/La_3GaS_5O, and TEM images of (c) IrO_2/La_3GaS_5O and (d) post-treated IrO_2/La_3GaS_5O

Figure 2-19 shows the wavelength dependence of photocatalytic H_2 evolution from aqueous Na_2S (0.01 M) and Na_2SO_3 (0.01 M) solution over Pt/La_3GaS_5O (3.0 wt% photodeposited Pt) and O_2 evolution from aqueous $AgNO_3$ solution (0.01 M) over IrO_2/La_3GaS_5O (post-treated, 2 wt% deposited IrO_2). The rate of H_2 or O_2 evolution decreases with increasing cutoff wavelength to extinction at the absorption edge of La_3GaS_5O. These photocatalytic reactions thus proceed by the photogeneration of electrons and holes under visible light, consistent with photoelectrochemical measurements (vide infra).

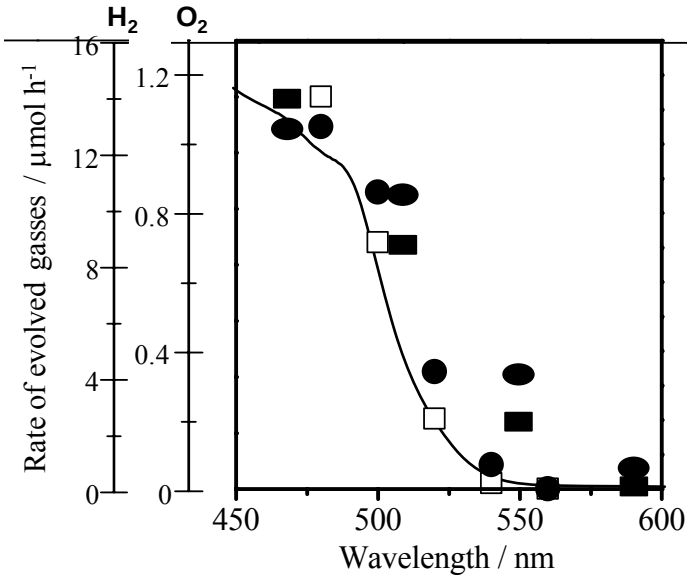

Figure 2-19. Wavelength dependence of initial rate of H_2 (□) and O_2 (●) evolution and UV-Vis DR spectrum results for La_3GaS_5O (H_2 evolution reaction; Catalyst (0.1 g): Pt (1 wt%)-loaded sample, Reactant solution (200 mL): Na_2S (0.01 M) and Na_2SO_3 (0.01 M) / distilled water, Light source: 300 W Xe Lamp with a cutoff filter ($\lambda > 420$ nm). O_2 evolution reaction; Catalyst (0.1 g): IrO_2 (2 wt%)-loaded sample, Reactant solution (200 mL): $AgNO_3$ (2 mmol) and La_2O_3 (0.2 g) / distilled water, Light source: 300 W Xe Lamp with a cutoff filter ($\lambda > 420$ nm))

La_3GaS_5O also exhibits an activity for photo-electrochemical the oxidation of S^{2-}-SO_3^{2-} species and water under visible irradiation. This oxysulfide also exhibits photocatalytic activity for H_2 and O_2 evolution form water containing sacrificial reagents. The apparent quantum efficiencies (5.3×10^{21} photons h^{-1} at 420 nm < λ < 540 nm) of Pt/La_3GaS_5O and IrO_2/La_3GaS_5O for H_2 and O_2 evolution are estimated to be 2.5% (H_2) and 0.2% (O_2). La_3GaS_5O thus exhibits superior quantum efficiency for H_2 evolution and comparable O_2 evolution to $Sm_2Ti_2S_2O_5$ (0.1% for H_2, 0.2% for O_2).[5,6] However, overall water splitting has yet to be achieved using La_3GaS_5O. As La_3GaS_5O was synthesized in the present study in evacuated quartz tubes from starting materials of La_2O_3, La_2S_3, and Ga_2S_3 at 1273 K, the surface of the La_3GaS_5O powder is likely to have been oxidized due to the presence of trace amounts of water in the precursors, and then produced H_2S, resulting in introducing sulfur vacancies into the crystalline product It is therefore expected that improvements in photocatalytic activity may be achieved by refining the procedures for preparation and cocatalyst modification.

2-3-4. Photoelectrochemical Measurements

Figure 2-20 shows the current–potential curves for the $LaGaS_2O$/FTO and La_3GaS_5O/FTO electrodes in a solution containing Na_2S and Na_2SO_3 as sacrificial electron donors under intermittent irradiation at wavelengths longer than 300 nm (UV–Vis) or 420 nm (Vis). The measurements were conducted by scanning the potential from –1.2 to 0.2 V vs. Ag/AgCl, above which Na_2S and Na_2SO_3 undergo electrochemical oxidation on the FTO surface. A response to visible irradiation was only

observed for the La_3GaS_5O/FTO electrode (Figure 2-20 (a)), consistent with the band-gap energies estimated from the UV-Vis DRS results (Figure 2-7 (A)). The $LaGaS_2O$/FTO electrode gave a response under UV irradiation at wavelengths longer than ca. 300 nm (Figure 2-7 (A)), while the $LaGaO_3$/FTO electrode did not respond to irradiation at any wavelengths in the range examined.

The $LaGaS_2O$ and La_3GaS_5O electrodes produced small cathodic currents when irradiated at wavelengths longer than those corresponding to the respective band gaps, indicative of the response by thermal excitation. Anodic photocurrent was also observed, attributable to oxidation of S^{2-}, SO_3^{2-}, and H_2O as shown schematic representation (Figure 2-20 (B)) indicating that the $LaGaS_2O$ and La_3GaS_5O electrodes functioned as n-type semiconductors. Figure 2-21 shows the dependence of photocurrent (0.2 V vs. Ag/AgCl) on the cut-off wavelength of incident light for the La_3GaS_5O electrode and the UV-vis DR specrum. These measurements were carried out by inserting various wavelength cut-off filters between the lamp and cell window. Photocurrent was observed at up to 540 nm, and the variation in photocurrent with respect to wavelength is in good agreement with UV-vis DRS results. The observed photocurrent can thus be attributed to a photoelectrochemical oxidation reaction via the band-gap transition of La_3GaS_5O.

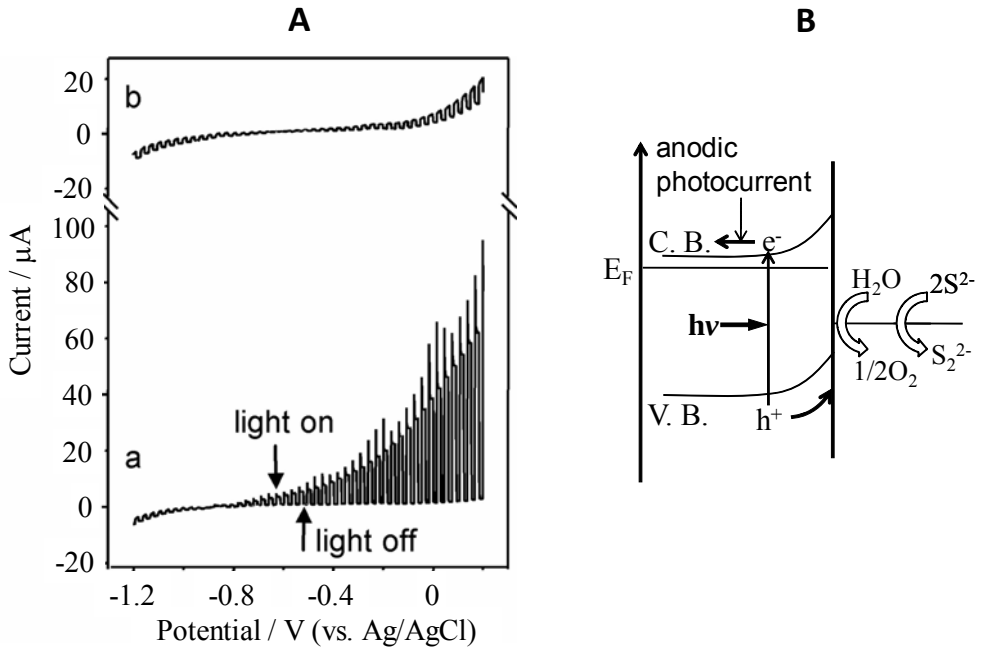

Figure 2-20. (A) Current-potential curves for (a) La_3GaS_5O/FTO and (b) $LaGaS_2O$/FTO electrodes under intermittent irradiation (Reactant solution (200 mL): Na_2S (0.01 M) and Na_2SO_3 (0.01 M) /distilled water, Light source: 300 W Xe Lamp with a cutoff filter ($\lambda > 420$ nm).) (B) Schematic representation of the mechanism of photoanodic reaction on La_3GaS_5O/FTO and $LaGaS_2O$/FTO

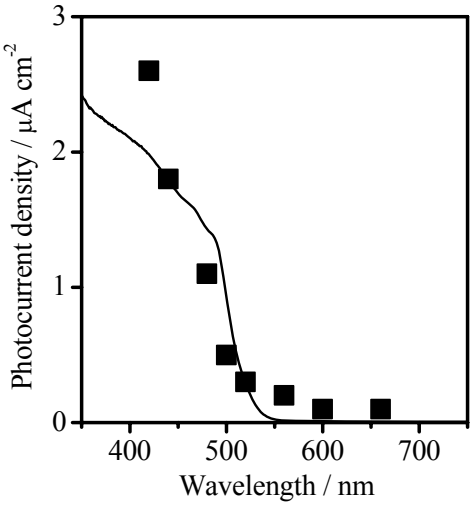

Figure 2-21. Wavelength dependence of photocurrent and UV-Vis DRS results for La_3GaS_5O at 0.2 V vs. Ag/AgCl (Reactant solution (200 mL): Na_2S (0.01 M) and Na_2SO_3 (0.01 M) /distilled water, Light source: 300 W Xe Lamp with a cutoff filter ($\lambda > 420$ nm).)

As the observed anodic photocurrents are deemed to be related to the band-gap transition, the band-gap positions of La_3GaS_5O were evaluated by measuring the onset potentials of anodic photocurrent on the La_3GaS_5O/FTO electrode in solutions with various pH values. The onset potentials of anodic photocurrent were also determined in this manner for the $LaGaS_2O$/FTO electrode. Current–potential curves were measured in darkness and under irradiation and from negative potential to positive potential using Na_2S–Na_2SO_3 solutions with pH of 10.0, 11.0, and 11.5 (adjusted by addition of 0.01 M NaOH to 0.1 M Na_2SO_4 solution), and pH of 4.0 and 6.0 (adjusted by addition of 0.01 M H_2SO_4 to 0.01 M NaOH solution). Although the observed anodic photocurrent in 0.1 M Na_2SO_4 solution may be associated with both the oxidation of water and the La-Ga oxysulfides themselves, the reactions could not be distinguished due to the relatively low photocurrent. However, as the $LaGaS_2O$ and La_3GaS_5O powders function as photocatalysts for water oxidation in the presence of Ag^+ (see below), the observed anodic photocurrent in both cases appears to be associated with water oxidation.

Figure 2-22 shows the estimated onset potential values as a function of pH. The estimated onset potential contains ±0.05 V experimental error bars due to the relatively small difference between anodic photocurrent and dark current around the onset potential. For single-semiconductor electrodes, the onset potential of photocurrent corresponds to the flat-band potential (E_{FB}) of the semiconductor.[32] The E_{FB} values estimated from the onset potential of anodic photocurrent for TiO_2[33] and WO_3[34] electrodes prepared on FTO are also consistent with those observed for single-semiconductor electrodes. It therefore appears reasonable to estimate E_{FB} from the onset

potential of anodic photocurrent for $LaGaS_2O$ and La_3GaS_5O, both of which act as n-type semiconductors. The E_{FB} of $LaGaS_2O$ and La_3GaS_5O shift almost linearly with changing pH of the electrolyte solution, with slopes of –66±10 and –33±10 mV/ΔpH, respectively. The potential of the conduction band edge (E_{CB}) is assumed in the present study to be –0.3 V more negative than E_{FB} due to the insulating n-type semiconducting properties of La_3GaS_5O and $LaGaS_2O$.[32] Using the band-gap energies estimated from the UV-Vis DRS results, the valence band edge potentials (E_{VB}) for $LaGaS_2O$ and La_3GaS_5O are estimated to be 3.0 and 2.3 V more positive than E_{CB}.

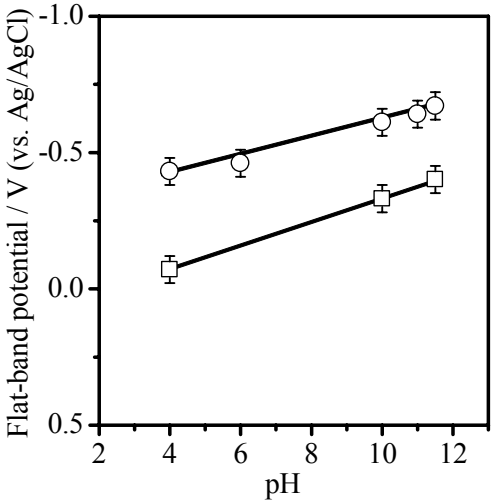

Figure 2-22. Flat-band potential of (a) $LaGaS_2O$ and (b) La_3GaS_5O as a function of pH

Figure 2-23 shows a schematic of the band positions for $LaGaS_2O$ and La_3GaS_5O at pH 11.5. The E_{CB} values for $LaGaS_2O$ and La_3GaS_5O are similar, whereas the E_{VB} value of La_3GaS_5O is much higher than that of $LaGaS_2O$. The similarity of E_{CB} values is reasonable considering that the conduction bands of both materials consist mainly of Ga 4s and 4p orbitals, as indicated by DFT calculations. However, the DFT calculations also showed that the contribution of S 3p orbitals to the valence band affects the value of E_{VB}. Similar results have been reported for tantalum-based (Ta_2O_5,

TaON, Ta_3N_5)[35] and gallium-based (GaN, GaN:ZnO) materials.[36] In the cases of these tantalum-based and gallium-based materials, the E_{CB} values are similar among materials in their respective groups, while changes in orbitals lead to marked changes in E_{VB}.

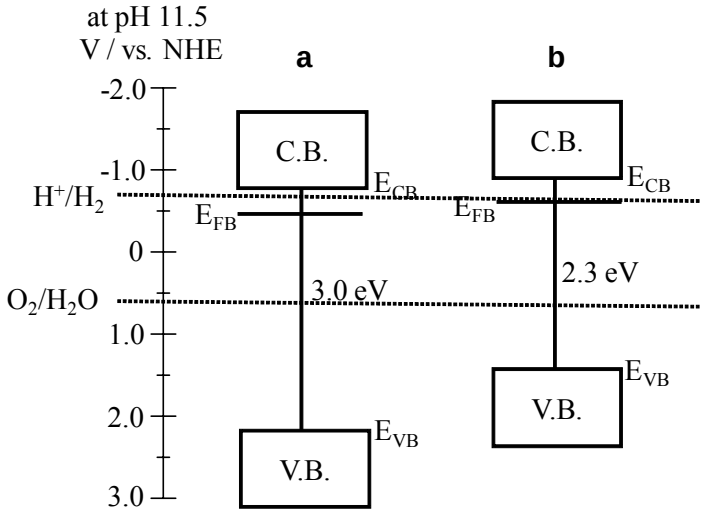

Figure 2-23. Schematic band structure of (a) $LaGaS_2O$ and (b) La_3GaS_5O at pH 11.5

The levels of E_{CB} and E_{VB} for $LaGaS_2O$ and La_3GaS_5O are sufficient for the reduction of H^+ to H_2 and the oxidation of water to O_2 via band-gap irradiation. In photocatalytic reactions, H_2 evolution was observed for $LaGaO_3$ loaded with 1 wt% Pt (3809.6 μmol) and $LaGaS_2O$ loaded with 1 wt% Pt (4089.6 μmol) in the first hour of reaction in a solution containing 0.01 M Na_2S–Na_2SO_3 under UV irradiation ($\lambda \geq 190$ nm) using a 450 W mercury lamp. However, no gas evolution was observed under visible irradiation ($\lambda \geq 420$ nm) using a 300 W xenon lamp, consistent with the results of photoelectrochemical measurements.

Finally, overall water splitting reaction over La-Ga based materials was investigated. Figure

2-24 shows the time course of overall water splitting reaction over $LaGaO_3$, $LaGaS_2O$, and La_3GaS_5O. $LaGaO_3$ has a potential for water splitting, on the other hand, as yet we have not successfully achieved overall water splitting using La-Ga based oxysulfide such as $LaGaS_2O$ and La_3GaS_5O. Overall water splitting reaction did not proceed for loading NiO, RuO_2, and Rh/Cr_2O_3 cocatalyst as shown in Table 2-6, and only tiny amount of H_2 was observed. The further investigation of control loading amount of cocatalysts and pH of the solution were not successful. The rate of H_2 evolution decreased with reaction time and was reduced to almost zero after 48 h. The crystallinity of the catalyst after the overall water splitting reaction for 2d decreased as compared with that before the reaction as shown in Figure 2-25 (B). These results indicate that evolved H_2 may be due to the photooxidation of catalyst.

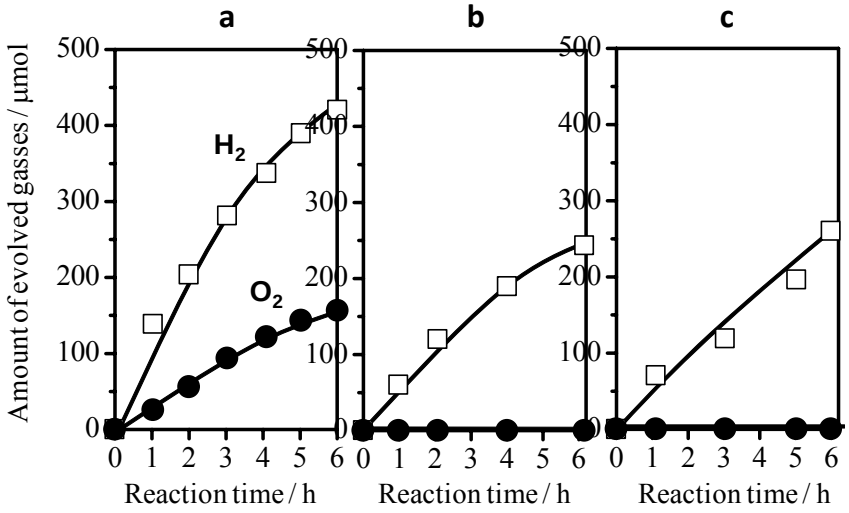

Figure 2-24. Time course of overall water splitting over (a) RuO_2(1wt%)/$LaGaO_3$, (b) RuO_2(1wt%)$LaGaS_2O$, (c) RuO_2(1wt%)La_3GaS_5O (Catalyst (0.2 g): RuO_2 (1 wt%) - loaded sample, Reactant solution (400 mL): distilled water, Light source: 450 W Hg Lamp ($\lambda > 190$ nm))

Table 2-6. Effect of co-catalyst loaded La-In oxysulfide photocatalyst on water splitting

cocatalyst	activity / μmol h^{-1}	
(loading amount / wt%)	H_2	O_2
—	1.3	0
NiO (1)	2.8	0
RuO_2 (1)	12	0
Rh(3)-Cr_2O_3(1)	2.9	0

a. Catalyst (0.2 g): cocatalyst - loaded sample, Reactant solution (400 mL): distilled water, Light source: 450 W high pressure Hg Lamp (λ > 290 nm).

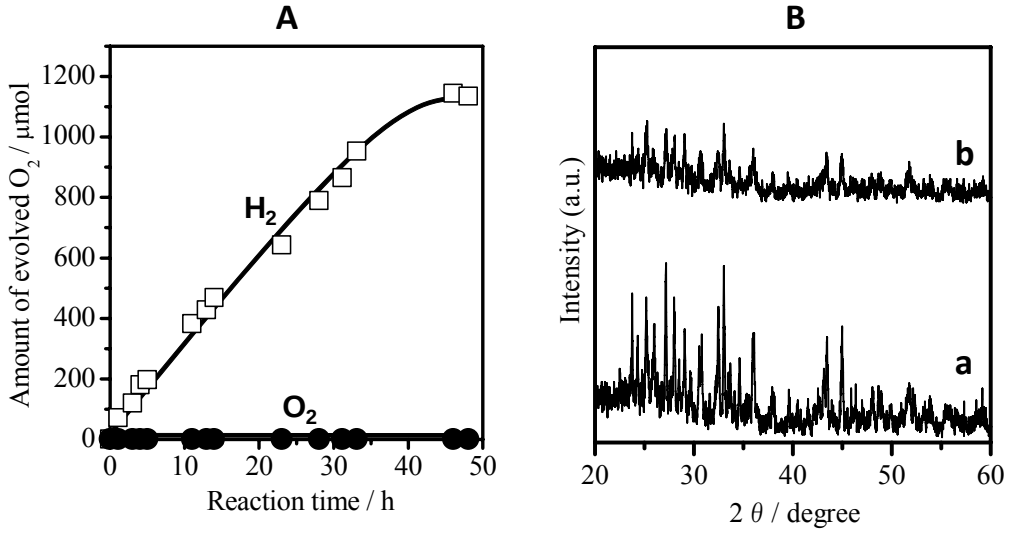

Figure 2-25 (A) Time course of overall water splitting over RuO_2(1wt%)/La_3GaS_5O (Catalyst (0.2 g): RuO_2 (1 wt%) - loaded sample, Reactant solution (400 mL): distilled water, Light source: 450 W Hg Lamp (λ > 190 nm)) (B) XRD patterns of La_3GaS_5O before the reaction and after the overall water splitting reaction for 48 h.

2-4. Conclusion

This chapter describes development of novel oxysulfides as visible light driven photocatalysts, which consist of metal ions (Cu^+, Zn^{2+}, Ga^{3+}, In^{3+}, Ge^{4+}, and Sn^{4+}) with d^{10} electronic configuration. In particular, La-In based materials and La-Ga based materials; $LaGaO_3$, $LaGaS_2O$, and La_3GaS_5O are focused.

La–In oxysulfide was demonstrated to photocatalyze the reduction of H^+ to H_2 and the oxidation of H_2O to O_2 under visible-light irradiation in the presence of a sacrificial electron donor (Na_2S–Na_2SO_3) or acceptor (Ag^+), respectively. This oxysulfide, with a band gap of 2.6 eV, was thus confirmed to be a photocatalyst with reduction and oxidation abilities, having conduction and valence bands at suitable potentials for the reduction of H^+ and oxidation of H_2O. O_2 evolution was effectively enhanced by loading with IrO_2, while Pt was proved to be suitable as a cocatalyst for H_2 evolution.

The La-Ga-based oxysulfides $LaGaS_2O$ and La_3GaS_5O were prepared and characterized as potential photocatalysts for water oxidation and reduction. Photoelectrochemical measurements showed that both materials have similar bottom levels of the respective conduction bands, whereas La_3GaS_5O has a higher valence band top than $LaGaS_2O$. The estimation of the electronic band structure revealed that the upper part of the valence band is composed of S 3p orbitals, contributing to the narrowing of the band gap of La_3GaS_5O in comparison to $LaGaO_3$ and $LaGaS_2O$. The band-gap positions of these oxysulfides are located at suitable potentials for the reduction and oxidation of water in the pH range of 4–12. The photocatalytic activity of these La-Ga-based

oxysulfides in the presence of sacrificial reagents was also investigated. The photodeposition of nanoparticulate ruthenium and platinum on La_3GaS_5O was found to promote the evolution of H_2, whereas loading with other metals (Rh, Pd, and Ni) was found to be not as effective as Ru and Pt. The deposition of colloidal IrO_2 on La_3GaS_5O also promoted O_2 evolution by a factor of approximately 5 times. The positive effect of post-preparation heat treatment of IrO_2 loaded samples at 573 K on photocatalytic activities was also demonstrated. The improved stability of photocatalytic activity realized by post-treatment appears to be related to a change in the morphology of IrO_2 particles upon heating.

References

1. N. Bühler, K. Meier, J.-F. Reber, *J. Phys. Chem.*, **88**, 3261 (1984).
2. M. Matsumura, S. Furukawa, Y. Saho, H. Tsubomura, *J. Phys. Chem.*, **89**, 1327 (1985).
3. J.-F. Reber, K. Meier, *J. Phys. Chem.*, **88**, 5903 (1984).
4. I. Tsuji, H. Kato, H. Kobayashi, A. Kudo, *J. Am. Chem. Soc.*, **126**, 13406 (2004).
5. A. Ishikawa, T. Takata, J. N. Kondo, M. Hara, H. Kobayashi, K. Domen, *J. Am. Chem. Soc.*, **124**, 13547 (2002).
6. A. Ishikawa, Y. Yamada, T. Takata, J. N. Kondo, M. Hara, H. Kobayashi, K. Domen, *Chem. Mater.*, **15**, 4442 (2003).
7. A. Ishikawa, T. Takata, T. Matsumura, J. N. Kondo, M. Hara, H. Kobayashi, K. Domen, *J. Phys. Chem. B*, **108**, 2637 (2004).
8. D. S. Ginley, C. Bright. *Transparent conducting oxides, MRS Bull.*, **25**, 15 (2000).
9. K. Ueda, S. Inoue, S. Hirose, H. Kawazoe, H. Hosono, *Appl. Phys. Lett.*, **78**, 2333 (2001).
10. M. Palazzi, *C. R. Acad. Sci. Paris*, **292**, 789 (1981).
11. S. Inoue, K. Ueda, H. Hosono, N. Hamada, *Phys. Rev. B*, **64**, 1 (2001).
12. J. Sato, N. Saito, Y. Yamada, K. Maeda, T. Takata, J. N. Kondo, M. Hara, H. Kobayashi, K. Domen, Y. Inoue, *J. Am. Chem. Soc.* **127**, 4150 (2005).
13. K. Maeda, K. Teramura, D. Lu, T. Takata, N. Saito, Y. Inoue, K. Domen, *Nature*, **440**, 295 (2006).
14. Y. Lee, H. Terashima, Y. Shimodaira, K. Teramura, M. Hara, H. Kobayashi, K. Domen, M.

Yashima, *J. Phys. Chem. C*, **111**, 1042 (2007).

15. I. Ijjaali, C. L. Haynes, A. D. Mcfarland, R. P. V. Duyne, J. A. Ibers, *J. Solid State Chem*., **172**, 257 (2003).
16. H. Kabbour, L. Cario, Y. Moëlo, A. Meerschaut, *J. Solid State Chem*., **177**, 1053 (2004).
17. S. Jaulmes, *Acta. Cryst. B*, **34**, 2610 (1978).
18. S. Jaulmes, M. Mazurier, M. Guittard, *Acta. Cryst. C*, **39**, 1594 (1983).
19. C. L. Teske, *Z. Anorg. Allg. Chem.*, **531**, 52 (1985).
20. C. J. Howard, B. J. Kennedy, *J. Phys.: Condens. Matter*, **11**, 3229 (1999).
21. M. Guittard, S. Benazeth, J. Dugué, S. Jaulmes, M. Palazzi, P. Laruelle, J. Flahaut, *J. Solid State Chem*. **51**, 227 (1984).
22. M. C. Payne, M. P. Teter, D. C. Allan, T. A. Arias, J. D. Joannopoulos, *Rev. Mod. Phys*. **64**, 1045 (1992).
23. B. G. Pfommer, M. Cote, S. G. Louie, M. L. Cohen, *J. Comput. Phys.*, **131**, 133 (1997).
24. D. Vanderbilt, *Phys. Rev. B*, **41**, 7982 (1990).
25. J. A. White, D. M. Bird, *Phys. Rev. B.* **50**, 4954 (1994).
26. J. P. Perdew, K. Bruke, M. Ernzerhof, *Phys. Rev. Lett.*, **77**, 3865 (1996).
27. A. Likforman, M. Cuittard, *Acta Crystallogr., Sect. C*, **49**, 1270 (1993).
28. S. A. Amirov, N. A. Shnulin, G. G. Guseinov, S. Kh, Mamedov, *Kristallografiya*, **29**, 787 (1984).
29. J. Sato, H. Kobayashi, Y. Inoue, *J. Phys. Chem. B*, **107**, 7970 (2003).
30. K. Foger, H. Jaeger, *J. Cat.,* **70**, 53 (1981).

31. T. Arikawa, Y. Takasu, Y. Murakami, K. Asakawa, Y. Iwasawa, *J. Phys. Chem. B,* **102**, 3736 (1998).

32. D. Vanderbilt, *Phys. Rev. B*, **41**, 7982 (1990).

33. J. A. White, D. M. Bird, *Phys. Rev. B*, **50**, 4954 (1994).

34. J. P. Perdew, K. Bruke, M. Ernzerhof, *Phys. Rev. Lett*., **77**, 3865 (1996).

35. W. J. Chun, A. Ishikawa, H. Fujisawa, T. Takata, J. N. Kondo, M. Hara, M. Kawai, Y. Matsumoto, K. Domen, *J. Phys. Chem. B*, **107**, 1798, (2003).

36. H. Hashiguchi, K. Maeda, R. Abe, A. Ishikawa, J. Kubota, K. Domen, *Bull. Chem. Soc. Jpn.*, in press (2008).

Chapter 3

Preparation and Photocatalytic Properties of Oxysulfides Based on Metal Ions (Ti^{4+}, Nb^{5+}, and Ta^{5+}) with d^0 Electronic Configuration

3-1. Introduction

Transition metal based materials, in particular oxides, have no electron in the d-orbital of the third (Ti^{4+} such as TiO_2), fourth (Nb^{5+} such as Nb_2O_5), and fifth (Ta^{5+} such as Ta_2O_5) shells. In previous research, Ishikawa et al. reported that $Ln_2Ti_2S_2O_5$ oxysulfide (Ln = Pr, Nd, Sm, Gd, Tb, Dy, Ho, and Er) functions as a stable photocatalysts for the reduction of H^+ to H_2 and oxidation of H_2O to O_2 in the presence of a sacrificial electron donor and acceptor under visible-light irradiation.[1-3] Our group, and Kudo and co-workers mainly studied and demonstrated that transition metal based oxides such as $SrTiO_3$,[4] $K_4Nb_6O_{17}$,[5] $K_2La_2Ti_3O_{10}$,[6] and $NaTaO_3$[7]etc. work as photocatalysts with high activity under the UV irradiation. Therefore, transition metal based oxysulfides are hopeful promising photocatalysts similar to typical metal based oxysulfide (Chapter 2). This chapter discusses development of novel transition metal based oxysulfides shown in Table 3-1 (except for $Ln_2Ti_2S_2O_5$) for overall water splitting reaction: Up to date, $Sm_2Ti_2S_2O_5$ was found to show the highest photocatalytic activity for H_2 or O_2 evolution reaction in the presence of sacrificial reagents among the oxysulfide photocatalysts.

Table 3-1. Transition metal based Oxysulfides

Cation	Photocatalyst
Ti^{4+}	$La_6Ti_2S_8O_5$
	$La_4Ti_3S_4O_8$
	$Sm_2Ti_2S_2O_5$
Nb^{5+}	$La_2ANbS_2O_5$ (A=Sc, Y, La)
	$A_3NbS_3O_4$ (A=Y, Sm, Gd, Dy, Er)
Ta^{5+}	$La_2ATaS_2O_5$ (A=Sc, Y, La)
	$A_3TaS_3O_4$ (A=Y, Sm, Gd, Dy, Er)

3-2.Experimental Section

3-2-1.Synthesis of Transition Metal (Ti^{4+}, Nb^{5+}, and Ta^{5+}) Based Oxysulfides

3-2-1-1.Ti Based Oxysulfides

The transition metal (Ti^{4+}, Nb^{5+}, and Ta^{5+}) based oxysulfide materials were synthesized by solid state reaction. In general, the starting materials were loaded in a quartz tube (outer diameter: 7.5±0.5 mm, tube wall thickness: 0.8±0.3 mm, length: 100 mm) then evacuated at ambient temperature and heated at 473 K for 5 h in order to remove adsorbed water. The tube was then sealed and heated to the required temperature. The respective synthesis procedure for each photocatalyst will be described below in detail.

(a) $La_6Ti_2S_8O_5$

$La_6Ti_2S_8O_5$ was prepared from the reaction of La_2S_3 (99.9%, High Purity Chemicals), La_2O_3 (99.99%, Kanto Chemical, pretreated at 1273 K for 5 h at 10 K min^{-1}), and TiO_2 (99.0%, Kanto Chemical, pretreated at 1273 K for 5 h at 10 K min^{-1}) with the molar ratio of 8:1:6 in a sealed quartz

tube. The sample was heated under vacuum at a rate of 10 K min^{-1} up to 673 K, then at a rate of 10 K h^{-1} up to 1273 K, and kept for 96 h, and then cooled at 100 K h^{-1} to room temperature.[8]

(b) $La_4Ti_3S_4O_8$

$La_4Ti_3S_4O_8$ was prepared from the reaction of La_2S_3 (99.9%, High Purity Chemicals), La_2O_3 (99.99%, Kanto Chemical, pretreated at 1273 K for 5 h at 10 K min^{-1}), and TiO_2 (99.0%, Kanto Chemical, pretreated at 1273 K for 5 h at 10 K min^{-1}) with the molar ratio of 4:2:9 in a sealed quartz tube. The sample was heated under vacuum at a rate of 10 K min^{-1} up to 673 K, then at a rate of 10 K h^{-1} up to 1273 K, and kept for 96 h, and then cooled at 100 K h^{-1} to room temperature.[8]

(c) $Sm_2Ti_2S_2O_5$

$Sm_2Ti_2S_2O_5$ was prepared by solid state reaction and H_2S gas sulfurization. In the case of solid state reaction, $Sm_2Ti_2S_2O_5$ samples were obtained by heating a mixture of TiO_2 (99.0%, Kanto Chemical, pretreated at 1273 K for 5 h at 10 K min^{-1}), TiS_2 (99.9%, High Purity Chemicals), and Sm_2O_3 (99.95%, Wako Chemical, pretreated at 1273 K for 5 h at 10 K min^{-1}) with the molar ratio of 1:1:1 in a sealed quartz tube. The sample was heated under vacuum at a rate of 10 K min^{-1} up to 673 K, then at a rate of 10 K h^{-1} up to 1273 K, kept for 168 h, and then cooled at 100 K h^{-1} to room temperature.

In the case of H_2S gas sulfurization[2], precursor oxide $Sm_2Ti_2O_7$ was prepared by the polymerized complex method using $Ti(O\mathit{i}Pr)_4$ (97%, Kanto Chemical) and $Sm(NO_3)_3{\cdot}6H_2O$ (99.5%, Wako Chemical) as string materials. Ethylene glycol (99.5%, Kanto Chemical) and methanol (99.8%, Kanto Chemical) were employed as solvents, and anhydrous critic acid (98%, Wako Chemical) was

employed as complexing agent to immobilize Ti and Sm ions. After polymerization of a mixture containing stoichiometric amounts of Sm and Ti (Sm/Ti=1:1) according to the method in the literature, $Sm_2Ti_2O_7$ were obtained by calcination at 773 K for 10 h in air. $Sm_2Ti_2S_2O_5$ was prepared from the oxide precursor (1.0 g) by calcination under flowing H_2S (flow rate: 10 mL min^{-1}) at 1173 K for 1 h. The heating treatment in detail was raised at a rate of 10 K min^{-1} up to 1173 K, was kept for 1 h, and was then cooled at 10 K min^{-1} to room temperature.

3-2-1-2.Nb and Ta Based Oxysulfides

(d) $La_2AMS_2O_5$ (M = Nb, Ta; A = Sc, Y, La)

$La_3MS_2O_5$ (M = Nb, Ta) were prepared by the reaction between La_2O_3 (99.99%, Kanto Chemical, pretreated at 1273 K for 5 h at 10 K min^{-1}), La_2S_3 (99.9%, High Purity Chemicals), and M_2O_5 (Nb_2O_5:99.95%, Kanto Chemical; Ta_2O_5:99.95%, Wako Chemical, pretreated at 1273 K for 5 h at 10 K min^{-1}) with the molar ratio of 5:4:3 in a sealed quartz tube. The sample was heated under vacuum at a rate of 10 K min^{-1} up to 673 K, then at a rate of 10 K h^{-1} up to 1273 K, and kept for 96 h, and then cooled at 100 K h^{-1} to room temperature.

$La_2AMS_2O_5$ (M = Nb, Ta; A=Sc, Y) were prepared by the reaction between La_2O_3 (99.99%, Kanto Chemical, pretreated at 1273 K for 5 h at 10 K min^{-1}), A_2O_3 (Sc_2O_3: 99.95%, Kanto Chemical; Y_2O_3: 99.99%, Kanto Chemical, pretreated at 1273 K for 5 h at 10 K min^{-1}), La_2S_3 (99.9%, High Purity Chemicals), and M_2O_5 (Nb_2O_5:99.95%, Kanto Chemical; Ta_2O_5:99.95%, Wako Chemical, pretreatment at 1273 K for 5 h, pretreated at 1273 K for 5 h at 10 K min^{-1}) with the molar ratio of

2:3:4:3 in a sealed quartz tube. The sample was heated under vacuum at a rate of 10 K min^{-1} up to 673 K, then at a rate of 10 K h^{-1} up to 1273 K, and kept for 96 h, and then cooled at 100 K h^{-1} to room temperature.[9]

(e) $A_3MS_3O_4$ (A = Y, Sm, Gd, Dy, Er; M = Nb, Ta)

$A_3MS_3O_4$ (A = Y, Sm, Gd, Dy, Er; M = Nb, Ta) were prepared by the reaction between A_2S_3 (Y_2S_3: 99.9%, High Purity Chemicals; Sm_2S_3: 99.9%, Soekawa Chemical; Gd_2S_3: 99.9%, Mitsuwa Chemical; Dy_2S_3: 99.95%, Mitsuwa Chemical; Er_2S_3: 99.9%, Mitsuwa Chemical), A_2O_3 (Y_2O_3: 99.99%, Kanto Chemical; Sm_2O_3: 99.95%, Kanto Chemical; Gd_2O_3: 99.95%, Kanto Chemical; Dy_2O_3: 99.95%, Kanto Chemical; Er_2O_3: 99.95%, Kanto Chemical, pretreated at 1273 K for 5 h at 10 K min^{-1}), and M_2O_5 (Nb_2O_5:99.95%, Kanto Chemical; Ta_2O_5:99.95%, Wako Chemical, pretreated at 1273 K for 5 h at 10 K min^{-1}) with the molar ratio 2:1:1 in a sealed quartz tube. The sample was heated under vacuum at a rate of 10 K min^{-1} up to 673 K, then at a rate of 10 K h^{-1} up to 1273 K, and kept for 96 h, and then cooled at 100 K h^{-1} to room temperature.[10]

3-2-2.Preparation and Deposition of Cocatalyst

3-2-2-1. Loading of H_2 Evolution Cocatalyst

Metal (Ni, Ru, Rh, and Pt) and metal (Pt, Ru, and Rh) / Cr_2O_3 as cocatalysts in attempt to enhance H_2 evolution were loaded on the oxysulfide by in-situ photodeposition using $Ni(NO_3)_2 \cdot 6H_2O$ (99.95%, Kanto Chemical), $RuCl_3 \cdot nH_2O$ (99.9%, Kanto Chemical), $RhCl_3 \cdot 3H_2O$ (74.0 % as $RhCl_3$, Kanto Chemical), $(NH_4)_2PdCl_4$ (37.0% as Pd, Kanto Chemical), $H_2PtCl_6 \cdot 6H_2O$ (37.50% as Pt,

Aldrich), and $Cr(NO_3)_3 \cdot 9H_2O$ (99.9%, Wako Chemical) in the presence of the sacrificial electron donors (0.01 M Na_2S, 0.01 M Na_2SO_3). Oxysulfides except for $Sm_2Ti_2S_2O_5$ were modified with Pt as H_2 evolution cocatalyst. In the case of metal (Pt, Ru, and Rh) / Cr_2O_3, $Sm_2Ti_2S_2O_5$ was first modified with noble metal (Pt, Ru, and Rh) by photodeposition under UV irradiation ($\lambda > 290$ nm) for 5 h. The noble metal loaded sample was then dispersed in aqueous $Cr(NO_3)_3$ solution. After evacuation to remove remaining air from the reactor, the solution was exposed to UV irradiation ($\lambda > 290$ nm) for 5 h to reduce $Cr(NO_3)_3$ into Cr_2O_3 to obtain noble metal / Cr_2O_3 (core/shell) nanoparticles loaded $Sm_2Ti_2S_2O_5$ sample.

3-2-2-2. Loading of O_2 Evolution Cocatalyst

MnO_2, Co_3O_4, NiO_x, RuO_2, and IrO_2 as cocatalyst in attempt to enhance O_2 evolution were loaded on the oxysulfide by impregnation using $NaMnO_4 \cdot H_2O$ (97%, Aldrich), $Co(NO_3)_2 \cdot 6H_2O$ (97%, Kanto Chemical), $Ni(NO_3)_2 \cdot 6H_2O$ (99.95%, Kanto Chemical), $RuCl_3 \cdot nH_2O$ (99.9%, Kanto Chemical) and $Na_2IrCl_6 \cdot 6H_2O$ (97.0%, Kanto Chemical), respectively. The samples were heated at 523 K in static air. IrO_2 was also loaded by adsorption from a IrO_2 colloidal solution, which were prepared by hydrolysis of $Na_2IrCl_6 \cdot 6H_2O$ (97.0%, Kanto Chemical) in a basic aqueous solution (pH 12) controlled by 0.1 M NaOH solution. The adsorption was performed by adding 0.5 g of La_3GaS_5O and several amount of colloidal solution to distilled water under vigorous stirring. After stirring for 0.5 h, the transparent supernatant solution was decanted, and the IrO_2-adsorbed sample thus obtained was rinsed three times in distilled water. The sample was then dried at 353 K, in some

cases followed by heating in air at 523 K for 1 h. The amount of colloidal IrO_2 adsorbed by the sample was estimated by measuring the 500–700 nm absorbances of the supernatant rinse solutions.

3-2-2-3. Loading of Both H_2 Evolution and O_2 Evolution Cocatalyst

$Sm_2Ti_2S_2O_5$ samples were loaded with both Rh / Cr_2O_3 and IrO_2 colloid or Co_3O_4 or MnO_2 cocatalysts in attempt to enhance H_2 and O_2 evolution. Rh was first loaded by photodeposition, followed by loading of Cr_2O_3 by photodeposition, and finally modified IrO_2, Co_3O_4, and MnO_2. IrO_2 colloid was deposited; Co_3O_4 and MnO_2 were loaded by impregnation method at 523 K for 1 h.

3-2-3.Characterization

The crystal structure of the resulting material was examined by powder X-ray diffraction (XRD) using a Rigaku Gergerflex RAD-B instrument with Cu Kα radiation. Ultraviolet–visible diffuse reflectance spectra were obtained using a Jasco V-560 spectrometer and were converted from reflection to absorbance by the Kubelka –Munk method. The binding energies determined by XPS were corrected in reference to the C 1s (284.6 eV) due to surface contamination carbon for each sample. The Burner, Emmett, Teller (BET) surface area was measured with a Coulter SA-3100 instrument at liquid nitrogen temperature. Particle size and morphology of photocatalyst powder was observed by scanning electron microscopy (SEM; Hitachi S-4700) and transmission electron microscopy (TEM; JEOL JEM-2010F). Chemical composition was determined by elemental analysis and energy-dispersive X-ray spectroscopy (EDX; Horiba Emax-7000).

3-2-4.Photocatalytic Reactions

The photocatalytic reaction was carried out in a Pyrex reaction vessel connected to a closed gas circulation and evacuation system as shown in Figure 2-1. The photocatalyst powder was dispersed in aqueous solutions by a magnetic stirrer in a Pyrex reaction vessel. Photoreduction of H^+ to H_2 and photooxidation of H_2O to O_2 in the presence of a sacrificial electron donor and acceptor was examined as test photoreactions. H_2 evolution was typically examined 200 mL aqueous solution containing 0.1 g of catalyst and sacrificial electron donors (0.01 M Na_2S-Na_2SO_3). The photooxidation of water to O_2 was performed in 200 mL of 0.01 M $AgNO_3$ solution (Ag^+ : sacrificial electron acceptor) containing 0.1 g catalyst and 0.2 g La_2O_3 powder. Due to the presence of La_2O_3, the pH of the solution during the photoreaction was buffered at pH = 8-9 by the dissolution of La_2O_3 or $La(OH)_3$. To remove air from the reactor, the solution was evacuated several times and then irradiated with visible light ($\lambda \geq 420$ nm) through a cut-off filter (HOYA, L42) from a 300 W Xe lamp (ILC technology; CERMAX LX-300). The amount of H_2 or O_2 evolved was determined using a on-line gas chromatography (Shimadzu; GC-8A, MS-5A column, TCD, Ar carrier).

3-3.Results and Discussion

3-3-1. Physicochemical Properties

X-ray diffraction was used to identify the crystal structure, and compared to Inorganic Crystal Structure Database (ICSD) file*. The band gap energies were estimated from observed absorption band edge in UV-Vis DRS. Crystal structures were drawn using the crystallographic parameter of ICSD. Each crystal structure analysis and estimation of band gap energy is shown as follows.

3-3-1-1.Ti based Oxysulfides

(a) $La_6Ti_2S_8O_5$

Figure 3-1 (A) compares the XRD patterns of (b) as-prepared $La_6Ti_2S_8O_5$ with (a) ICSD file ($La_6Ti_2S_8O_5$, #79367).[8] X-ray analysis showed that the obtained sample consisted of $La_6Ti_2S_8O_5$ as main phase and La_2S_3 as impurity phase. UV-Vis DR spectrum of the obtained sample is shown Figure 3-1 (B). The absorption edge is observed at 650 nm with a shoulder up to 700 nm, and the band gap energy is estimated to be 1.9 eV or 1.8 eV.

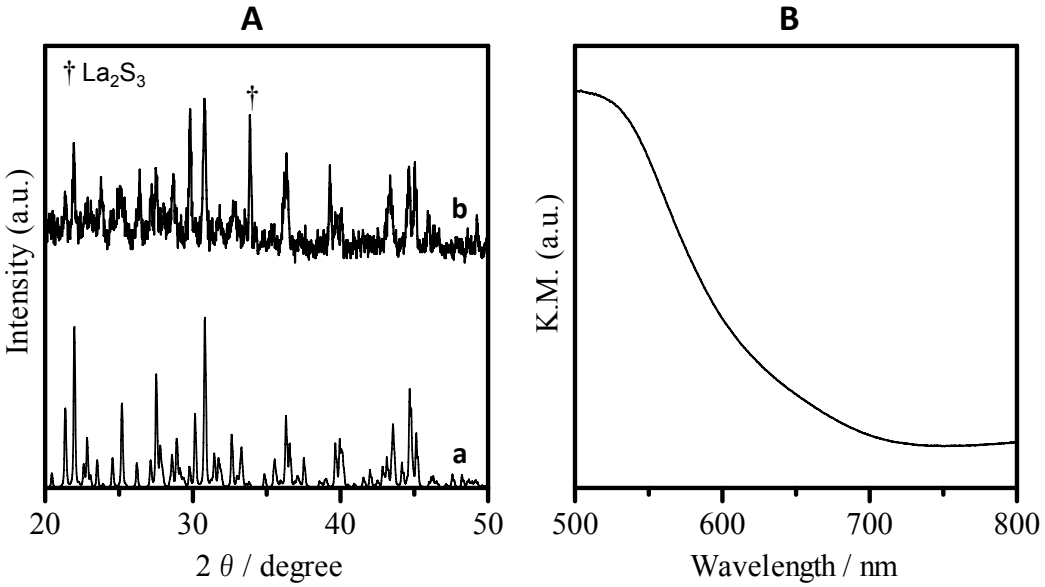

Figure 3-1. (A) XRD patterns for (a) ICSD file ($La_6Ti_2S_8O_5$, #79367) and (b) obtained sample (1273 K, 96 h) and (B) UV-Vis DR spectrum for $La_6Ti_2S_8O_5$.

(b) $La_4Ti_3S_4O_8$

Figure 3-2 (A) compares the XRD patterns of (b) as-prepared $La_4Ti_3S_4O_8$ with (a) ICSD file ($La_4Ti_3S_4O_8$, #79368).[8] X-ray analysis showed that the obtained sample consisted of $La_4Ti_3S_4O_8$. UV-Vis DR spectrum of obtained sample is shown in Figure 3-2 (B). The absorption edge is observed at 750 nm and the band gap energy is estimated to be 1.7 eV. The absorption beyond absorption edge can be attributed to the existence of a small amount of Ti^{3+} species in the sample.

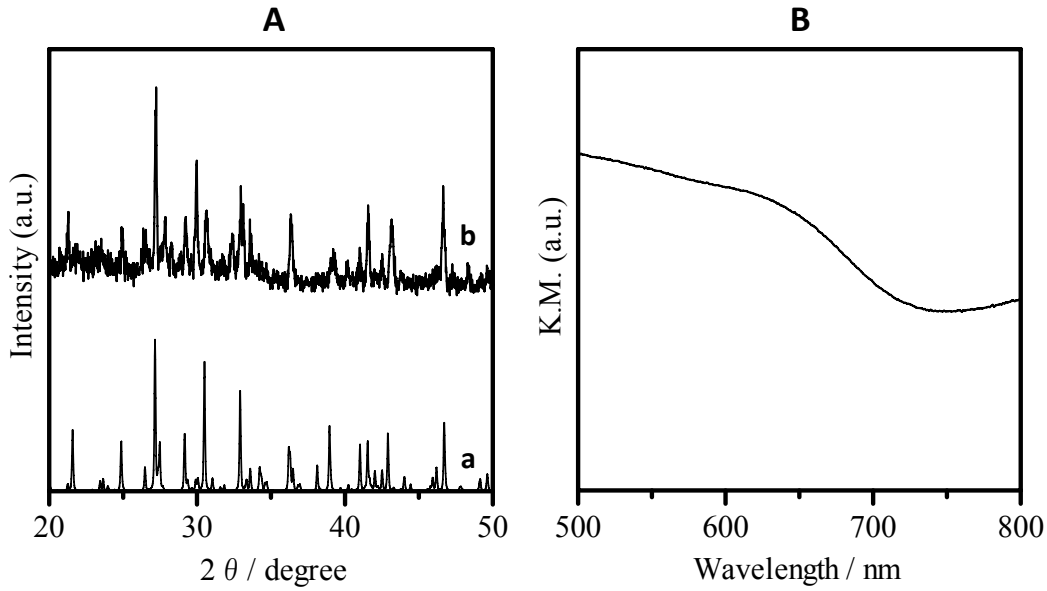

Figure 3-2. (A) XRD patterns for (a) ICSD file ($La_4Ti_3S_4O_8$, #79368) and (b) obtained sample (1273 K, 96 h) and (B) UV-Vis DR spectrum for $La_4Ti_3S_4O_8$.

(c) $Sm_2Ti_2S_2O_5$

Figure 3-3 (A) compares the XRD patterns of (b) $Sm_2Ti_2S_2O_5$ by solid state reaction H_2S gas sulfurization and (c) $Sm_2Ti_2S_2O_5$ with (a) ICSD file ($Sm_2Ti_2S_2O_5$, #91764).[11] X-ray analysis showed that the obtained sample consisted of $Sm_2Ti_2S_2O_5$. UV-Vis DR spectrum of the obtained sample is shown Figure 3-3 (B). The absorption edge at 600 nm was observed for both samples. The band gap energy is estimated to be 2.1 eV accordingly. The absorption beyond absorption edge can be attributed to the existence of a small amount of Ti^{3+} species in the sample.

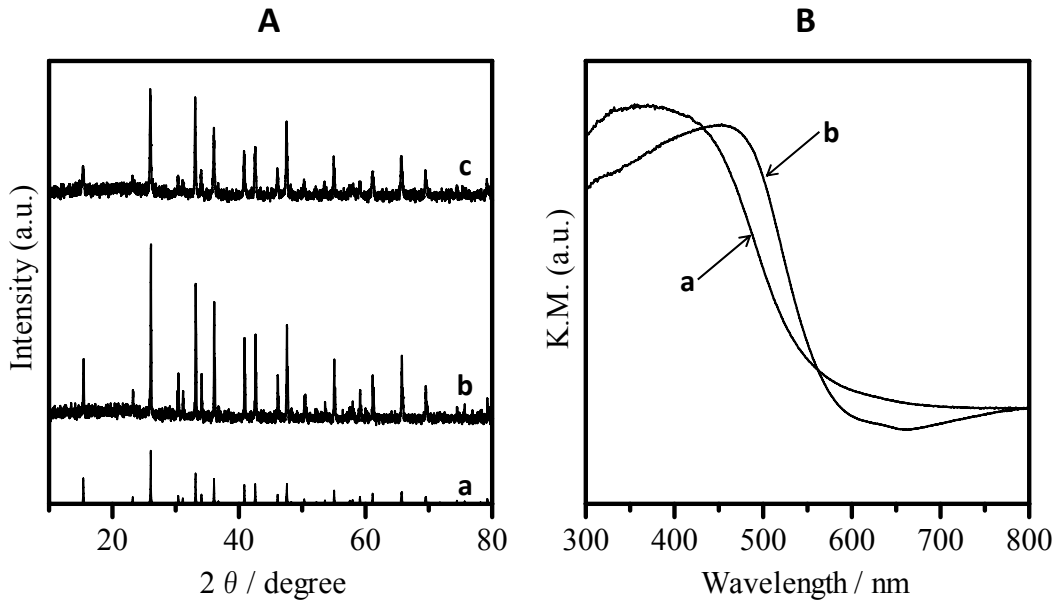

Figure 3-3. (A) XRD patterns for (a) ICSD file ($Sm_2Ti_2S_2O_5$, #91764), (b) obtained sample (solid state reaction at 1273 K for 168 h), (c) obtained sample (H_2S gas sulfurization at 1173 K for 1 h) (B) UV-Vis DR spectra for $Sm_2Ti_2S_2O_5$ by (a) solid state reaction at 1273 K for 1 h and (b) H_2S gas sulfurization at 1173 K for 1 h

3-3-1-2.Nb based Oxysulfides

(d) $La_2ANbS_2O_5$ (A = Sc, Y, La)

Figure 3-4 (A) compares the XRD patterns of as-prepared $La_2ANbS_2O_5$ (A = Sc (b), Y (c), La (d)) with (a) ICSD file ($Sm_2Ti_2S_2O_5$, #91764).[11] X-ray analysis showed that the structures of these compounds have similar to that of $Sm_2Ti_2S_2O_5$. XRD patterns of $La_2YNbS_2O_5$ and $La_3NbS_2O_5$ have been already reported but that of $La_2ScNbS_2O_5$ have not been reported. $La_2ANbS_2O_5$ (A = Sc, Y, La) exhibits an intergrowth structure with NaCl-type slabs [La_2S_2] alternating regularly with perovskite-type oxide slabs [AMO_5 (A = Sc, Y, La)]. The [AMO_5] block is derived from the ideal [Ti_2O_5] blocks found in $Ln_2Ti_2S_2O_5$ (Ln = Nd-Er, Y) by the formal substitution of two Ti^{4+} ions with one A^{3+} and one M^{5+} ion. UV-Vis DR spectra of the obtained samples are shown Figure 3-4 (B). The

band gap energy of $La_2ANbS_2O_5$ (A = Sc (a), Y (b), La (c)) are estimated to be 2.9 eV (Sc), 2.6 eV (Y) and 2.4 eV (La) from each absorption band edge.

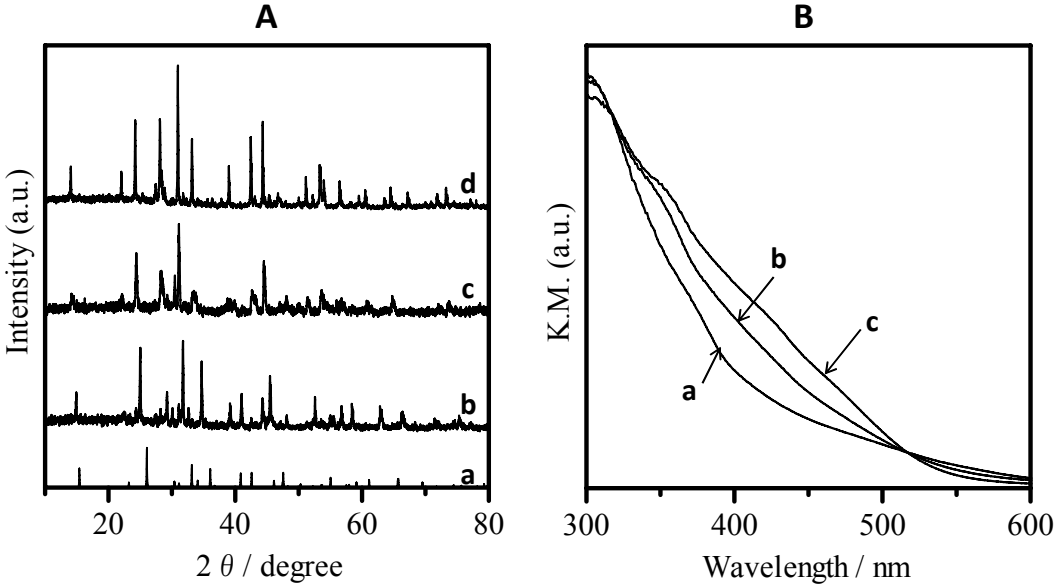

Figure 3-4. (A) XRD patterns for (a) ICSD file ($Sm_2Ti_2S_2O_5$, #91764) and $La_2ANbS_2O_5$ (A = Sc (b), Y (c), La (d)) and (B) UV-Vis DR spectra for $La_2ANbS_2O_5$ (A = Sc (a), Y (b), La (c))

(e) $A_3NbS_3O_4$ (A = Y, Sm, Gd, Dy, Er)

Figure 3-5 (A) compares the XRD patterns of as-prepared $A_3NbS_3O_4$ (A = Y (b), Sm (c), Gd (d), Dy (e), Er (f)) with (a) ICSD file ($Sm_3NbS_3O_4$, #91764).[10] X-ray analysis showed that the structures of these compounds have similar to that of $Sm_3NbS_3O_4$. UV-Vis DR spectra of obtained samples are shown in Figure 3-5 (B). The band gap energy of $A_3NbS_3O_4$ (A = Y (a), Sm (b), Gd (c), Dy (d), Er (e)) are estimated to be 2.7 eV (Y, Sm, Gd) and 3.2 eV (Er) from each absorption band edge. In the case of $Dy_3NbS_3O_4$, the absorption band edge could not be observed. The peaks arising from f-f transition were observed for $Dy_3NbS_3O_4$ and $Er_3NbS_3O_4$.

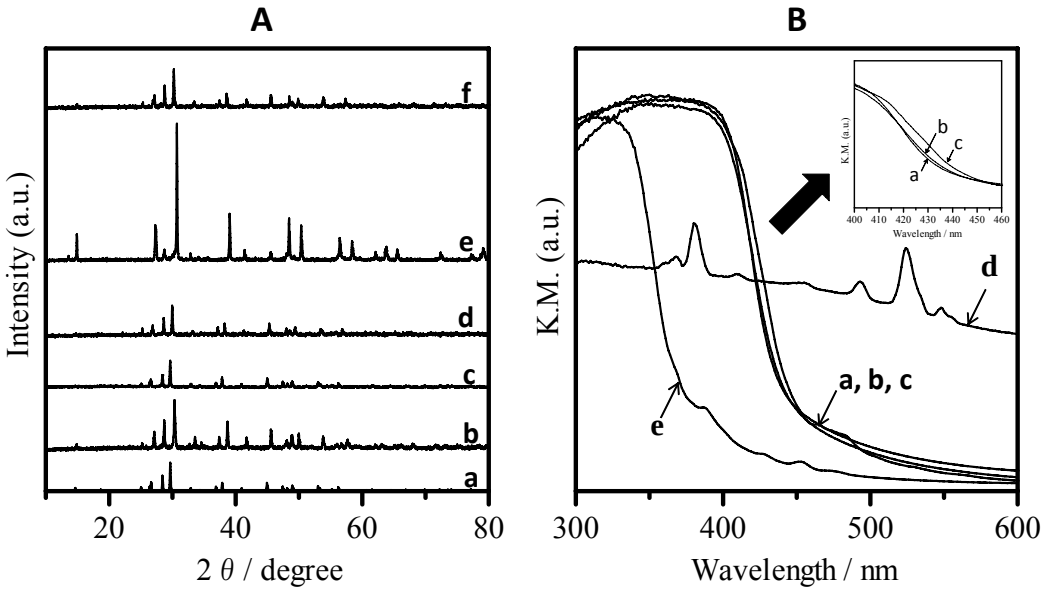

Figure 3-5. (A) XRD patterns for (a) ICSD file ($Sm_3NbS_3O_4$, #91764) and $A_3NbS_3O_4$ (A = Y (b), Sm (c), Gd (d), Dy (e), Er (f)) and (B) UV-Vis DR spectra for $A_3NbS_3O_4$ (A = Y (a), Sm (b), Gd (c), Dy (d), Er (e)).

3-3-1-3.Ta based Oxysulfides

(f) $La_2ATaS_2O_5$ (A = Sc, Y, La)

Figure 3-6 (A) compares the XRD patterns of as-prepared $La_2ATaS_2O_5$ (A = Sc (b), Y (c), La (d)) with (a) ICSD file ($Sm_2Ti_2S_2O_5$, #91764).[11] X-ray analysis showed that the structures of these compounds have similar to that of $Sm_2Ti_2S_2O_5$. The XRD patterns for $La_2YTaS_2O_5$ and $La_3TaS_2O_5$ have been already reported but that for $La_2ScTaS_2O_5$ has not. The XRD patterns shows the $Sm_2Ti_2S_2O_5$ structure as major phase, containing $[Ti_2O_5]$ perovskite blocks by the formal substitution of La^{3+} and Ta^{5+} for 2 Ti^{4+}. UV-Vis DR spectra of the obtained samples are shown Figure 3-6 (B). The band gap energies of $La_2ATaS_2O_5$ (A = Sc (a), Y (b), La (c)) are estimated to be 3.1 or 2.7 eV (Sc), 3.0 or 2.7 eV (Y) and 3.4 or 2.6 eV (La) from the observed absorption band edges.

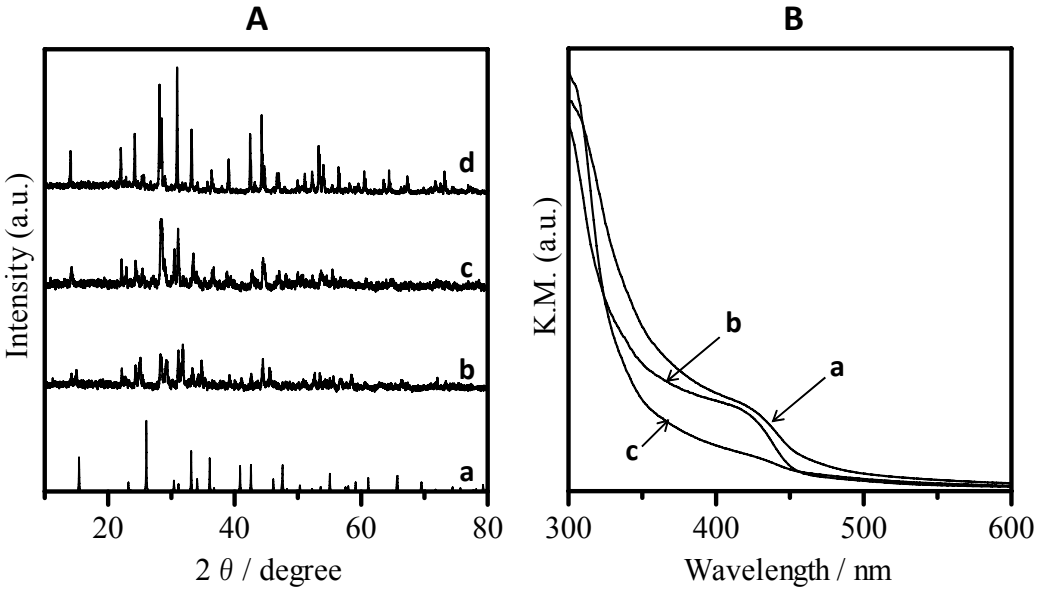

Figure 3-6. (A) XRD patterns for (a) ICSD file ($Sm_2Ti_2S_2O_5$, #91764) and $La_2ATaS_2O_5$ (A = Sc (b), Y (c), La (d)) and (B) UV-Vis DR spectra for $La_2ATaS_2O_5$ (A = Sc (a), Y (b), La (c))

(g) $A_3TaS_3O_4$ (A = Y, Sm, Gd, Dy, Er)

Figure 3-7 (A) shows comparisons between the XRD patterns of as-prepared $A_3TaS_3O_4$ (A = Y (b), Sm (c), Gd (d), Dy (e), Er (f)) and (a) ICSD file ($Sm_3NbS_3O_4$, #91764).[10] X-ray analysis showed that the structures of these compounds have similar to $Sm_3NbS_3O_4$. UV-Vis DR spectra of the obtained samples are shown in Figure 3-7 (B). The band gap energies of $A_3TaS_3O_4$ (A = Y (a), Sm (b), Gd (c), Dy (d), Er (e)) are estimated to be 3.3 eV (Y, Gd) , 3.0 or 2.4 eV (Sm) and 2.7 eV (Er) from the measured absorption band edges. In the case of $Dy_3TaS_3O_4$, the absorption band edge could not be determined. The peaks arising from f-f transition were observed for $Sm_3TaS_3O_4$ and $Dy_3TaS_3O_4$.

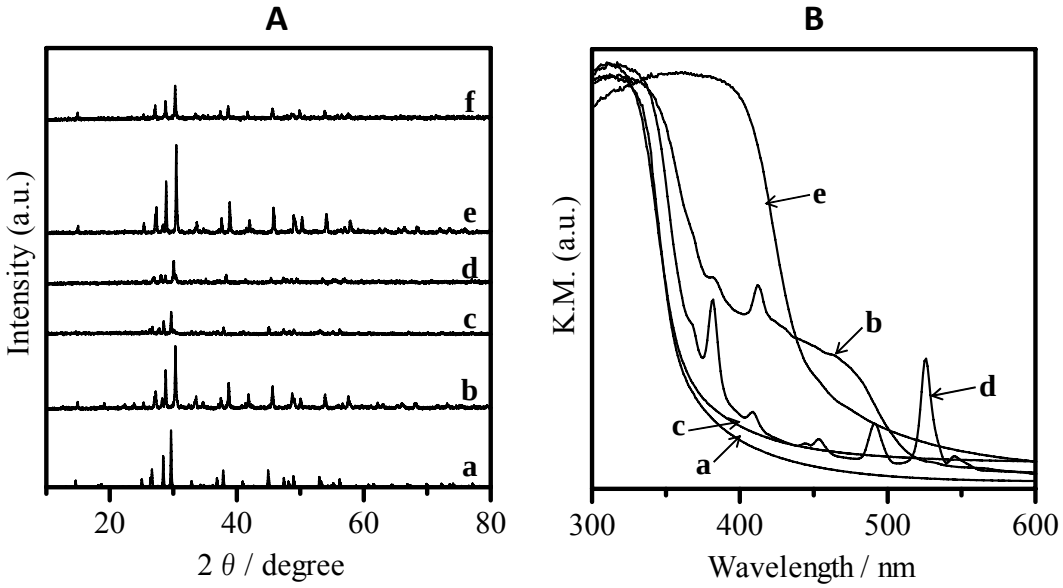

Figure 3-7. (A) XRD patterns for (a) ICSD file ($Sm_3NbS_3O_4$, #91764) and $A_3TaS_3O_4$ (A = Y (b), Sm (c), Gd (d), Dy (e), Er (f)) and (B) UV-Vis DR spectra for $A_3TaS_3O_4$ (A = Y (a), Sm (b), Gd (c), Dy (d), Er (e)).

3-3-2.Photocatalytic Reactions

Table 3-2 lists the photocatalytic activities of d^0 metal ions (Ti^{4+}, Nb^{5+}, and Ta^{5+}) based oxysulfides for the reduction of H^+ to H_2 and oxidation of H_2O to O_2 in the presence of sacrificial electron (Na_2S-Na_2SO_3) donor or acceptor (Ag^+). O_2 evolution was examined in a basic solution (pH = 8) buffered with La_2O_3. In the reaction, the rate of O_2 evolution decreased with reaction time due to the deposition of metallic silver on the surface of the catalyst, effectively shielding the catalyst from incident light. Therefore, the initial rate of O_2 evolution was regarded as the activity. Ti based oxysulfide ($La_6Ti_2S_8O_5$, $La_4Ti_3S_4O_8$ and $Sm_2Ti_2S_2O_5$) and Nb based oxysulfide ($A_3NbS_3O_4$ (A = Y, Sm, Gd) and $La_2ANbS_2O_5$ (A = Sc, Y, La)) have energy gap enough to absorb visible light, and, on the other hand, Ta based oxysulfide ($A_3TaS_3O_4$ (A = Y, Sm, Gd) and $La_2ATaS_2O_5$ (A = Sc, Y, La))

response to only UV light. Oxysulfides except for $Sm_2Ti_2S_2O_5$ have not sufficient for the reduction of H^+ and the oxidation of H_2O under visible light irradiation ($\lambda > 420$ nm) with 300 W Xe lamp. However, in the case of irradiation of UV light or visible light using high-pressure Hg lamp, Pt or IrO_2-loaded $La_2AMS_2O_5$ (A = Sc, Y, La; M = Nb, Ta and $Gd_3NbS_3O_4$) was demonstrated to have a potential for the reduction of H^+ to H_2 and the oxidation of H_2O to O_2 in the presence of a sacrificial electron donor (Na_2S-Na_2SO_3) or acceptor (Ag^+) as shown in Table 3-3. $Sm_2Ti_2S_2O_5$ has the highest photocatalytic activity for water splitting reaction in d^0 metal ion (Ti^{4+}, Nb^{5+}, Ta^{5+}) based oxysulfide photocatalysts and showed high photocatalytic activity for O_2 evolution even without an O_2 evolution cocatalyst such as IrO_2. Therefore, surface modification of $Sm_2Ti_2S_2O_5$ using cocatalysts was investigated in attempt to achieve overall water splitting reaction.

Table 3-2. Photocatalytic activity of d^0 metal ion (Ti^{4+}, Nb^{5+}, and Ta^{5+}) based oxysulfides under visible light irradiation

photocatalyst	B. G. / eV	steady rate of H_2 evolution[a] / μmol h^{-1}	initial rate of O_2 evolution[b] / μmol h^{-1}
$La_6Ti_2S_8O_5$	1.7	3	0
$La_4Ti_3S_4O_8$	2.1	0.2	0
$Sm_2Ti_2S_2O_5$ (SSR)	1.9	4	2
$Sm_2Ti_2S_2O_5$ (HGS)	1.9	13	16
$La_3NbS_2O_5$	2.4	0.3	0
$Gd_3NbS_3O_4$	2.7	0.7	0
$La_3TaS_2O_5$	3.4 (2.6)	1	0
$Gd_3TaS_3O_4$	3.3	0	0

a. Catalyst (0.2 g): Pt (1 wt%) - loaded sample, Reactant solution (200 mL): Na_2S (2 mmol) and Na_2SO_3 (2 mmol) /distilled water, Light source: 300 W Xe Lamp with a cutoff filter ($\lambda > 420$ nm).
b. Catalyst (0.2 g), Reactant solution (200 mL): $AgNO_3$ (2 mmol) and La_2O_3 (0.2 g) / distilled water, Light source: 300 W Xe Lamp with a cutoff filter ($\lambda > 420$ nm)

Table 3-3. Photocatalytic activity of Nb^{5+} and Ta^{5+} ion based oxysulfides

catalyst	rate of evolved gasses / μmol h^{-1}		
	H_2[a]		O_2[b]
	> 290 nm	> 400 nm	> 400 nm
$La_2ScNbS_2O_5$	78	8	17
$La_2YNbS_2O_5$	22	3	1
$La_3NbS_2O_5$	16	2	1
$La_2ScTaS_2O_5$	66	7	9
$La_2YTaS_2O_5$	49	7	2
$La_3TaS_2O_5$	13	3	1
$Gd_3NbS_3O_4$	56	28	1

a. Catalyst (0.2 g): Pt (1 wt%) - loaded sample, Reactant solution (440 mL): Na_2S (2 mmol) and Na_2SO_3 (2 mmol) /distilled water, Light source: 450 W high-pressure Hg Lamp ($\lambda > 290$ nm).
b. Catalyst (0.2 g), Reactant solution (440 mL): $AgNO_3$ (2 mmol) and La_2O_3 (0.2 g) / distilled water, Light source: 450 W high-pressure Hg Lamp ($\lambda > 290$ nm).

3-3-3.Overall Water Splitting Reaction over $Sm_2Ti_2S_2O_5$

3-3-3-1. Cocatalyst for H_2 Evolution Loaded on $Sm_2Ti_2S_2O_5$

It has been reported that the flat band potential of $Sm_2Ti_2S_2O_5$ is almost dependent of pH as shown in Figure 3-8.[1] As shown in Figure 3-8, $Sm_2Ti_2S_2O_5$ does not have the ability to oxidize H_2O to O_2 in the pH 0 to 4 region and is not stable in acidic aqueous solution (pH < 7). Therefore, the following overall water splitting reaction was examined in alkali aqueous solution adjusted to pH 12 by 0.1 M NaOH.

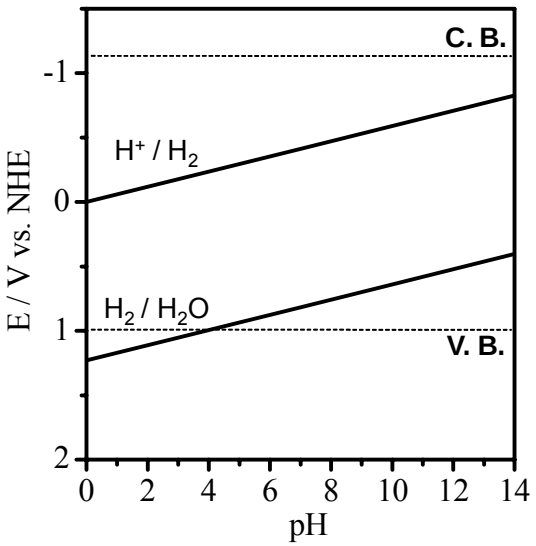

Figure 3-8. Band positions of $Sm_2Ti_2S_2O_5$ with pH.

Firstly, overall water splitting reactions were examined after loading cocatalysts (Pt, NiO_x, RuO_2, IrO_2, and Rh/Cr_2O_3) on the $Sm_2Ti_2S_2O_5$. These cocatalysts have been widely used as effective cocatalysts for photocatalytic overall water splitting. Especially, NiO_x[4-7]and Rh/Cr_2O_3[12, 13] were reported that the reverse reaction from H_2 and O_2 to form H_2O is suppressed. Figure 3-9 shows the

schematic model of overall water splitting reaction over cocatalyst (NiO_x, RuO_2, IrO_2, and Rh/Cr_2O_3) for H_2 evolution-loaded $Sm_2Ti_2S_2O_5$. In this system, it is considered that H_2 evolution happens on the cocatalyst and O_2 evolution happens on the catalyst surface.

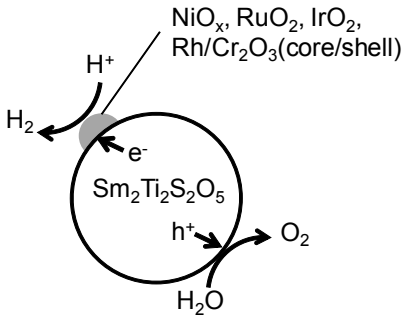

Figure 3-9. Schematic model of overall water splitting reaction over cocatalyst (NiO_x, RuO_2, IrO_2, Rh/Cr_2O_3) for H_2 evolution-loaded $Sm_2Ti_2S_2O_5$

Table 3-4 shows the photocatalytic activity of $Sm_2Ti_2S_2O_5$ loaded with various cocatalysts for overall water splitting reaction. Figure 3-10 shows the time course of overall water splitting reaction over Rh/Cr_2O_3 (core/shell)-loaded $Sm_2Ti_2S_2O_5$. Overall water splitting reaction did not proceed, which gives H_2 to O_2 ratio of 2, and tiny amount of H_2 was only detected. These results indicate that any cocatalysts were not effective for overall water splitting. However, for H_2 evolution reaction in the presence of Na_2S-Na_2SO_3, Rh and Ru are more effective than Pt as cocatalysts. In the case of metal (Pt, Ru, Rh)/Cr_2O_3-loaded $Sm_2Ti_2S_2O_5$, the H_2 evolution rate was maintained around 60-70 % of the photocatalytic activity for metal (Pt, Ru, Rh)-loaded $Sm_2Ti_2S_2O_5$. There is a possibility that the difference between the oxidation potential of water the valence band level is small, so that the oxidation of water is not efficient, therefore, O_2 evolution cocatalysts should also be essential.

Table 3-4. Photocatalytic activity of $Sm_2Ti_2S_2O_5$ loaded with various cocatalysts for overall water splitting reaction

cocatalyst	rate of evolved gasses [a] / μmol h^{-1}	
	H_2	O_2
No loading	0.1	0
Pt	1.1	0
NiO_x	0	0
RuO_2	0.7	0
IrO_2	0	0
Rh/Cr_2O_3 (core/shell)	0.5	0

a. Catalyst (0.2 g): cocatalyst (1 wt%) - loaded sample, Reactant solution (440 mL): distilled water (pH 12), Light source: 450 W high-pressure Hg Lamp. (λ > 290 nm)

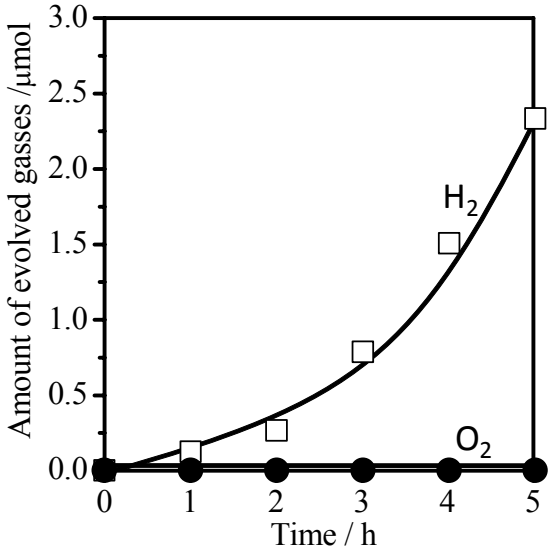

Figure 3-10. Time course of overall water splitting reaction over Rh/Cr_2O_3 (core/shell)-loaded $Sm_2Ti_2S_2O_5$ (Catalyst (0.2 g), Reactant solution (440 mL): an aqueous solution adjusted to pH 12 by NaOH, Light source: 450 W high-pressure Hg Lamp (λ > 290 nm).)

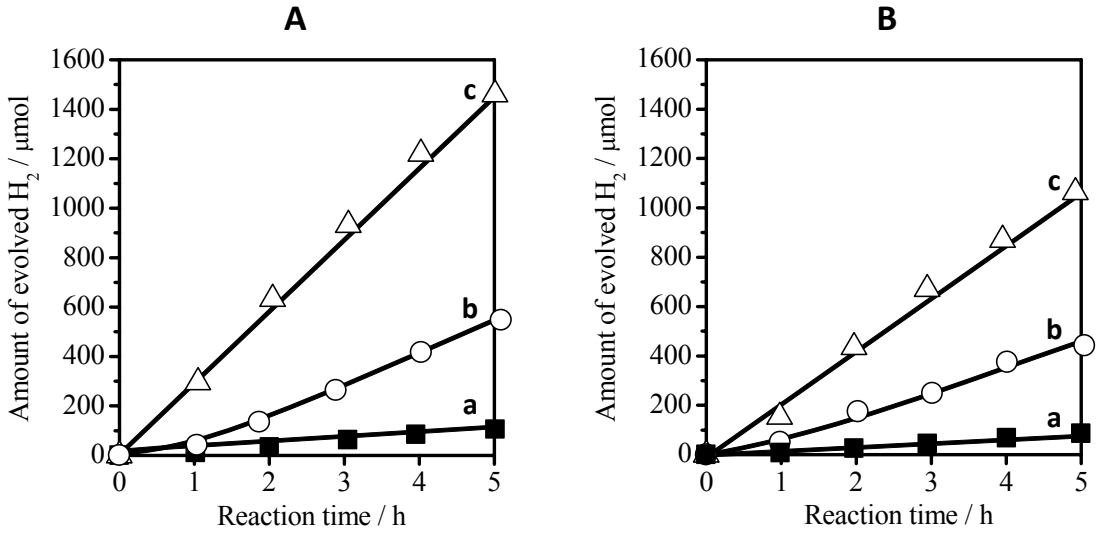

Figure 3-11. (A) Time course of H_2 evolution over Metal (Pt(a), Ru(b), Rh(c))-loaded $Sm_2Ti_2S_2O_5$ (B) Time course of H_2 evolution over Metal (Pt(a), Ru(b), Rh(c))/Cr_2O_3-loaded $Sm_2Ti_2S_2O_5$ (Catalyst (0.2 g), Reactant solution (440 mL): Na_2S (2 mmol) and Na_2SO_3 (2 mmol) /distilled water, Light source: 450 W high-pressure Hg Lamp ($\lambda > 290$ nm)).

3-3-3-2.Both H_2 Evolution Cocatalyst and O_2 Evolution Cocatalyst Loaded on $Sm_2Ti_2S_2O_5$

Modification with two different functioning materials for H_2 and O_2 evolution, respectively, have been designed in order to promote both H_2 and O_2 evolution reactions simultaneously during overall water splitting reaction. Figure 3-12 shows the schematic model of overall water splitting reaction over both H_2 evolution cocatalyst (Rh/Cr_2O_3) and O_2 evolution cocatalyst (IrO_2) loaded on $Sm_2Ti_2S_2O_5$. In this system, it may be ideal that H_2 evolution happens on the surface of Rh/Cr_2O_3 while O_2 evolution happens on the surface of IrO_2.

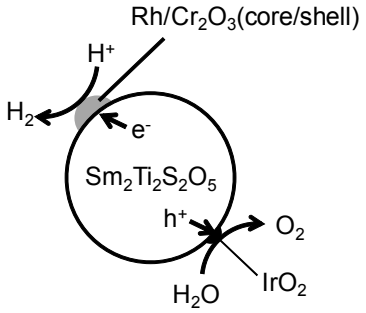

Figure 3-12. Schematic model of overall water splitting reaction over both H_2 evolution cocatalyst (Rh/Cr_2O_3) and O_2 evolution cocatalyst (IrO_2) loaded on $Sm_2Ti_2S_2O_5$

Figure 3-13 shows the time course of overall water splitting reaction over Rh/Cr_2O_3 (core/shell) and IrO_2-loaded $Sm_2Ti_2S_2O_5$. Tiny amount of H_2 was only observed whereas no O_2 evolution was observed. To investigate the role of the Rh/Cr_2O_3 and IrO_2, the photocatalytic activity of Rh/Cr_2O_3 and/or IrO_2-loaded $Sm_2Ti_2S_2O_5$ for H_2 and O_2 evolution from aqueous solutions containing Na_2S-Na_2SO_3 and silver nitrate were examined. Rh/Cr_2O_3 and/or IrO_2 drastically enhanced the activity for H_2 and O_2 evolution reaction. However, it remains the possibility that IrO_2 works as a H_2 evolution sites to improve not only O_2 evolution but also H_2 evolution. XPS spectra for Ir 4f of IrO_2 on $Sm_2Ti_2S_2O_5$ before (a) and after (b) H_2 evolution reaction are shown in Figure 3-14 (A). The Ir $4f_{7/2}$ peak arising from IrO_2 was shifted from 62.2 to 61.8 eV. The result indicates that IrO_2 may be reduced by photogenerated electron as shown in Figure 3-14 (B).

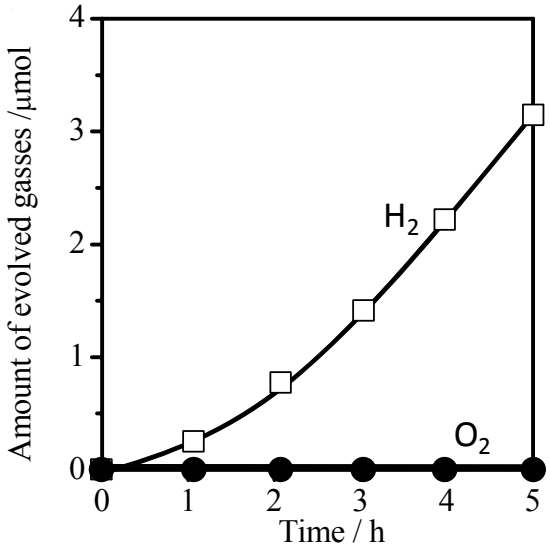

Figure 3-13. Time course of overall water splitting reaction over Rh/Cr_2O_3 (core/shell) and IrO_2-loaded $Sm_2Ti_2S_2O_5$ (Catalyst (0.2 g), Reactant solution (440 mL): an aqueous solution adjusted to pH 12 by 0.1 M NaOH, Light source: 450 W high-pressure Hg Lamp ($\lambda > 290$ nm).)

Table 3-5. Photocatalytic activity of cocatalyst (Rh/Cr_2O_3 and/or IrO_2)-loaded $Sm_2Ti_2S_2O_5$

Cocatalyst	H_2 [a] / μmol h^{-1}	O_2 [b] / μmol h^{-1}
No loading	1	4
Rh (2 wt%)/Cr_2O_3 (1 wt%)	104	16
IrO_2 colloid (2 wt%)	17	173
Rh (2 wt%)/Cr_2O_3 (1 wt%) + IrO_2 col. (2 wt%)	103	62

a. Catalyst (0.2 g): cocatalyst - loaded sample, Reactant solution (440 mL): Na_2S (2 mmol) and Na_2SO_3 (2 mmol) /distilled water, Light source: 450 W high-pressure Hg Lamp ($\lambda > 290$ nm).
b. Catalyst (0.2 g): cocatalyst - loaded sample, Reactant solution (440 mL): $AgNO_3$ (2 mmol) and La_2O_3 (0.2 g) / distilled water, Light source: 450 W high-pressure Hg Lamp ($\lambda > 290$ nm).

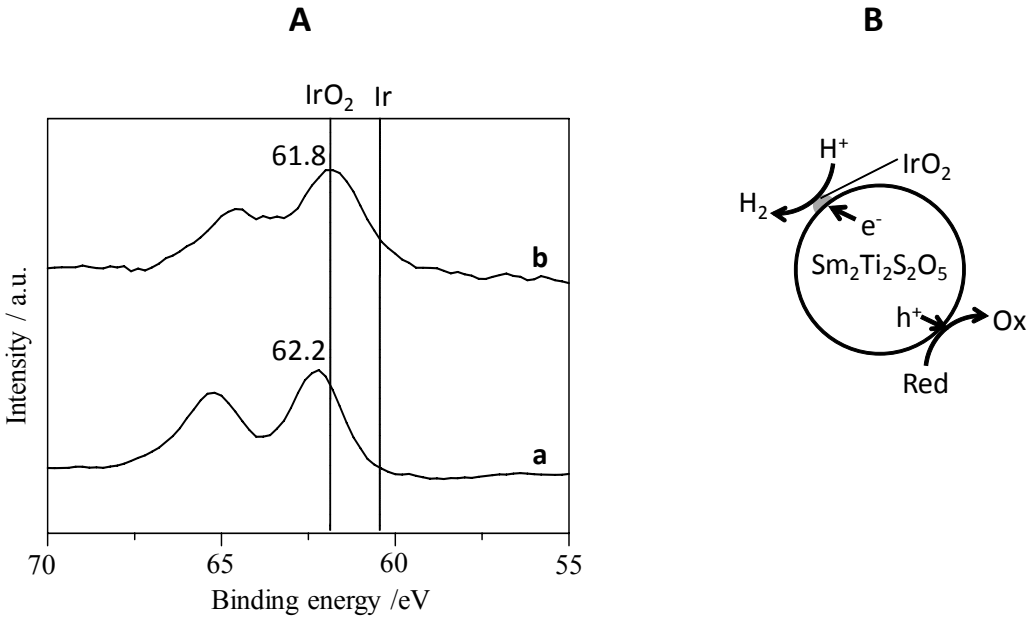

Figure 3-14. (A) XPS spectra for Ir 4f of IrO_2 on $Sm_2Ti_2S_2O_5$ before (a) and after (b) H_2 evolution reaction (B) Schematic model of H_2 evolution reaction over IrO_2-loaded $Sm_2Ti_2S_2O_5$

We investigated that O_2 evolution cocatalyst instead of IrO_2 selectively works only O_2 evolution cocatalyst. Table 3-6 shows the photocatalytic activity of O_2 evolution cocatalyst-loaded $Sm_2Ti_2S_2O_5$. MnO_2 and Co_3O_4 also functioned as O_2 evolution cocatalyst, and inhibited the H_2 evolution. Next, MnO_2 was used instead of IrO_2 (Figure 3-15). Figure 3-16 shows the time course of overall water splitting reaction over Rh/Cr_2O_3 (core/shell) and MnO_2-loaded $Sm_2Ti_2S_2O_5$. Overall water splitting reaction also did not proceed, and tiny amount of H_2 was only observed. To investigate the role of MnO_2, the photocatalytic activity of Rh/Cr_2O_3 and/or MnO_2-loaded $Sm_2Ti_2S_2O_5$ for H_2 and O_2 evolution from aqueous solutions containing Na_2S-Na_2SO_3 and silver nitrate were examined. MnO_2 and/or Rh/Cr_2O_3 enhanced the activity for O_2 evolution reaction. Figure 3-17 shows the XPS spectra for Mn 2p of MnO_2 before (a) and after (b) H_2 evolution reaction. The Mn $2p_{3/2}$ peak arising from

MnO_2 was slightly shifted from 642.1 to 642.4 eV. The result indicates that MnO_2 may be oxidized by photogenerated hole after H_2 evolution reaction, therefore, MnO_2 is not considered to work as a H_2 evolution cocatalyst. On the other hand, the H_2 evolution rate was drastically decreased. These results appear to be due to poor and randomly dispersion of loaded cocatalysts, resulting in low efficiency of electron transfer to H^+ and hole transfer to H_2O. Appropriate surface modification by both H_2 and O_2 cocatalysts might achieve overall water splitting reaction.

Table 3-6. Photocatalytic activity of O_2 evolution cocatalyst-loaded $Sm_2Ti_2S_2O_5$

Cocatalyst	H_2 [a] / μmol h^{-1}	O_2 [b] / μmol h^{-1}
No loading	1	4
IrO_2 (2 wt%)	17	173
MnO_2 (1 wt%)	2	44
Co_3O_4 (1 wt%)	7	22

a. Catalyst (0.2 g): cocatalyst - loaded sample, Reactant solution (440 mL): Na_2S (2 mmol) and Na_2SO_3 (2 mmol) /distilled water, Light source: 450 W high-pressure Hg Lamp ($\lambda > 290$ nm).
b. Catalyst (0.2 g): cocatalyst - loaded sample, Reactant solution (440 mL): $AgNO_3$ (2 mmol) and La_2O_3 (0.2 g) / distilled water, Light source: 450 W high-pressure Hg Lamp ($\lambda > 290$ nm).

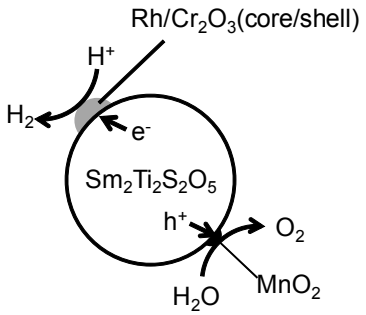

Figure 3-15. Schematic model of overall water splitting reaction over both H_2 evolution cocatalyst (Rh/Cr_2O_3) and O_2 evolution cocatalyst (MnO_2) loaded on $Sm_2Ti_2S_2O_5$

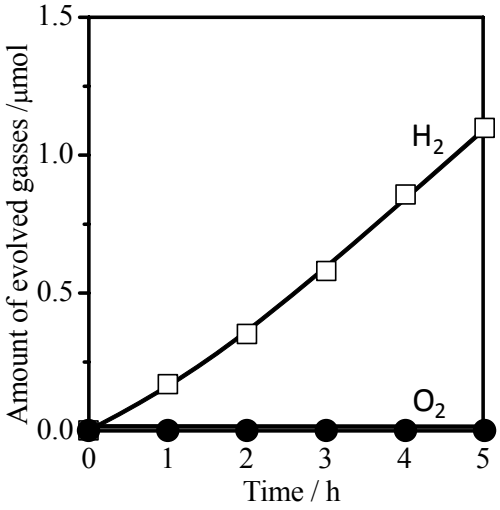

Figure 3-16. Time course of overall water splitting reaction over Rh/Cr_2O_3 (core/shell) and MnO_2-loaded $Sm_2Ti_2S_2O_5$ (Catalyst (0.2 g), Reactant solution (440 mL): an aqueous solution adjusted to pH 12 by 0.1 M NaOH, Light source: 450 W high-pressure Hg Lamp ($\lambda > 290$ nm).)

Table 3-7. Photocatalytic activity of cocatalyst (Rh/Cr_2O_3 and/or MnO_2)-loaded $Sm_2Ti_2S_2O_5$

Co-catalyst	H_2 [a] / μmol h^{-1}	O_2 [b] / μmol h^{-1}
No loading	1	4
Rh (2 wt%)/Cr_2O_3 (1 wt%)	104	16
MnO_2 (1 wt%)	2	44
Rh (2 wt%)/Cr_2O_3 (1 wt%) + MnO_2 (1 wt%)	3	69

a. Catalyst (0.2 g): cocatalyst - loaded sample, Reactant solution (440 mL): Na_2S (2 mmol) and Na_2SO_3 (2 mmol) /distilled water, Light source: 450 W high-pressure Hg Lamp ($\lambda > 290$ nm).
b. Catalyst (0.2 g): cocatalyst - loaded sample, Reactant solution (440 mL): $AgNO_3$ (2 mmol) and La_2O_3 (0.2 g) / distilled water, Light source: 450 W high-pressure Hg Lamp ($\lambda > 290$ nm).

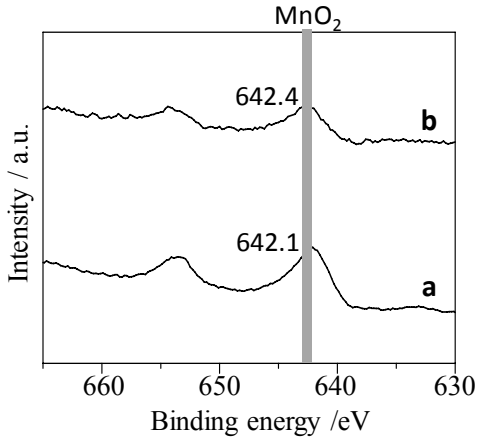

Figure 3-17. XPS spectra for Mn 2p of MnO_2 before (a) and after (b) H_2 evolution reaction

3-4.Conclusion

This chapter discusses development of novel oxysulfides as visible light driven photocatalysts which consist of metal ions (Ti^{4+}, Nb^{5+} and Ta^{5+}) with d^0 electronic configuration. Novel Nb and Ta based oxysulfide materials were synthesized and showed activity for the reduction of H^+ to H_2 and the oxidation of H_2O to O_2 in the presence of sacrificial reagents. However, these new photocatalysts have limited absorption in visible light region. On the other hand, $Sm_2Ti_2S_2O_5$ can absorb light up to ~ 600 nm and has the highest activity among d^0 metal ion based materials reported.

During overall water splitting reactions on the $Sm_2Ti_2S_2O_5$ in the presence of NiO_x or Rh/Cr_2O_3 cocatalysts, tiny amount of H_2 was only observed whereas no O_2 was formed. The modification with Rh/Cr_2O_3 cocatalyst shows highest rates for H_2 evolution in the presence of Na_2S-Na_2SO_3 sacrificial reagents. IrO_2, MnO_2, and Co_3O_4 cocatalysts promote O_2 evolution in the presence of Ag^+ sacrificial reagent. When the modification of Rh/Cr_2O_3 together with IrO_2, MnO_2 or Co_3O_4, H_2 and O_2 evolution reactions in the presence of sacrificial reagents proceeded effectively on the

modified-$Sm_2Ti_2S_2O_5$: however, overall water splitting reaction was not achieved (no O_2 was produced). Further investigations for appropriate and selective surface modification of both H_2 and O_2 evolution cocatalysts are still required.

References

1. A. Ishikawa, T. Takata, J. N. Kondo, M. Hara, H. Kobayashi, K. Domen, *J. Am. Chem. Soc.*, **124**, 13547 (2002).
2. A. Ishikawa, Y. Yamada, T. Takata, J. N. Kondo, M. Hara, H. Kobayashi, K. Domen, *Chem. Mater.*, **15**, 4442 (2003).
3. A. Ishikawa, T. Takata, T. Matsumura, J. N. Kondo, M. Hara, H. Kobayashi, K. Domen, *J. Phys. Chem. B*, **108**, 2637 (2004).
4. K. Domen, S. Naito, M. Soma, T. Onishi, K. Tamaru, *J. Chem. Soc., Chem. Commun.*, 543 (1980).
5. K. Domen, A. Kudo, A. Shinozaki, A. Tanaka, K. Maruya, T. Onishi, *J. Chem. Soc., Chem. Commun.,* 356 (1986).
6. T. Takata, Y. Furumi, K. Shinohara, A. Tanaka, M. Hara, J. N. Kondo, K. Domen, *Chem. Mater.,* **9**, 1063 (1997).
7. H. Kato, A. Kudo, *Chem. Phys. Lett.* **295**, 487 (1998).
8. J. A. Cody, J. A. Ibers, *J. Solid State Chem.*, **114**, 406 (1995).
9. L. Cario, A. F. Popa, A. Lafond, C. G. Deudon, H. Kabbour, A. Meerschaut, S. J. Clarke, P Adamson, *Inorg. Chem.* **46**, 9584 (2007).
10. C. B. Candan, A. Meerschaut, P. Palvadeau, *Materials Research Bulletin*, **35**, 1593 (2000).
11. C. B. Candalen, A. Meerschaut, *Comp. Rend. Acad. Sci. Série IIC* **2**, 93 (1994).

Chapter 4

Photocatalysis and Photoelectrolysis of CdS Nanoparticles Dispersed on TiO_2 Exhibiting Quantum Size Effect

4-1. Introduction

Hydrogen production from water using solar energies and semiconductor photocatalysts is a key technology for achieving sustainable energy conversion. Some oxides, such as TiO_2[1], $SrTiO_3$[2], and $NaTaO_3$[3], function as highly efficient photoelectrodes and photocatalysts under UV irradiation. To utilize sunlight, however, a candidate material must possess appropriate visible light absorption properties. Several chalcogenide materials, such as CdS[4], $NaInS_2$[5], and $(AgIn)_xZn_{2(1-x)}S_2$[6], are promising photocatalysts because they exhibit appropriate absorption of visible light.

Among these chalcogenide materials, CdS has received particular attention as a photocatalyst in recent years.[4] It has potential as an efficient photocatalyst for water splitting because of its visible-light absorption (B.G.=2.4 eV) and the position of its band edges.[4] The material itself, however, is unable to split H_2O to form H_2 and O_2, and the material decomposes in standard aqueous solution during photoreaction.[7-9] To enable the use of this material, many researchers have demonstrated the hydrogen evolution reaction in reducing agents such as EDTA, S^{2-}, SO_3^{2-} or hypophosphite ions to prevent photoanodic dissolution.[7-13] Stabilization of CdS on support materials such as TiO_2, AgI, ZnO, or HgS has also been investigated,[14-16] and may improve the efficiency of charge separation and photoreaction efficiency.

Semiconductor particles with diameters on the order of nanometers exhibit unique size-dependent properties, such as the quantum size effect which drastically alters electrical properties.[17-20] In the conventional infinite-depth well model[21], the excitation energy level E_{ln} of an ultra-small semiconductor particle with radius R is a function of the bandgap energy E_g of bulk

semiconductor and kinetic energy. The kinetic energy can be calculated as the energy of a particle in a box having a spherically symmetric square well potential of infinite depth:

$$E_{\ln} = E_g + \left(\frac{\eta^2}{2m^* R^2} \right) \phi_{\ln}^{\ 2}$$

where m^* is the reduced effective mass of the conduction band electron and valence band hole. ϕ_{ln} is the nth root of the spherical Bessel function of *l*th order.[21] The equation indicates that the bandgap of nanosize CdS (≤6 nm) is larger than that of CdS bulk, and the gap increases with decreasing particle size. Thus, nanoparticles show distinct oxidative and reductive abilities for photocatalytic reactions. Decreasing particle size also leads to an increase in surface area, altering mechanical, thermal and catalytic properties.

Well-tuned CdS nanoparticles have been synthesized with a very narrow size-distribution in the presence of protective ligands suspended in organic solution.[22-24] In contrast to many other studies, where CdS was synthesized from Cd solution and immobilized on a support material simultaneously,[25-32] we immobilized already-prepared CdS nanoparticles on TiO_2 to maintain the original particle sizes and avoid aggregation upon removal of the protective ligands and during photoreactions. By varying the immobilization method, CdS particle size, surface area of the support, and the amount of CdS and Pt (as a co-catalyst), the immobilized CdS/TiO_2 catalysts were tested for photocatalytic H_2 evolution and photoelectrochemical reactions in the presence of Na_2S/Na_2SO_3 sacrificial reagent under visible light irradiation. This study clearly shows the beneficial effects of immobilizing nanoparticles with quantum size effects, providing high efficiency and stability for photocatalytic reactions.

4-2.Experimental Section

4-2-1.Immobilization of CdS Nanoparticles on TiO_2 Support

CdS nanoparticles were synthesized based on the previously reported method.[22-24] The CdS nanoparticles were immobilized on TiO_2 photocatalysts then prepared by heat treatment and alkali treatment. CdS nanoparticles (1.6±0.2, 2.9±0.3, 3.4±0.4, 4.1±0.6, and 12.5±1.6 nm) suspended in hexane solution (Kanto Chemical, 96 %) with oleic acid (b.p. 468 K) and oleyl amine (b.p. 441 K) as protective ligands were added to TiO_2 (Degussa, P25) and mixed by ultrasonic agitation until the hexane was vaporized at 298 K. In the heat treatment, dried samples were heated at 473 or 623 K for 5 h in air. In the alkali treatment method, dried samples were added to 50 mL of 0.1 M NaOH solution and stirred for 1 h to remove protective ligands. The samples were filtered and washed with 50 mL of distilled water, then dried at 343 K in static air.

4-2-2.Characterization

Differential thermal analysis and thermogravimetry (TG-DTA; TG 8120, Rigaku) were used to study the crystallization, decomposition, melting and sublimation processes. The crystalline structure of the catalyst was examined by powder X-ray diffraction (XRD; Panalytical X´Pert Pro MPD). The optical properties were analyzed by an ultraviolet-visible diffuse reflectance spectrometer (DRS; V-560, Jasco). Particle size and photocatalyst morphology were examined by transmission electron microscopy (TEM; JEM-2010F, JEOL). The elemental compositions were probed by X-ray fluorescence (XRF; JEOL Element Analyzer JSX-3202C) and energy-dispersive X-ray spectroscopy

(EDX; Emax-7000, Horiba). The Brunauer-Emmett-Teller (BET) specific surface area was measured using a Coulter SA-3100 instrument at 77 K.

4-2-3.Photocatalytic Reactions

H_2 evolution reactions from 0.1 g of CdS/TiO_2 catalysts were performed using an aqueous solution (200 cm^3) in the presence of 0.1 M Na_2S and 0.1 M Na_2SO_3 as sacrificial electron donors. A Pt co-catalyst was loaded by photodeposition in the presence of the sacrificial electron donors (0.1 M Na_2S and 0.1 M Na_2SO_3) using $H_2PtCl_6 \cdot 6H_2O$ (Aldrich; ≥37.50% as Pt).

Photocatalytic reactions were carried out in a Pyrex reaction vessel connected to a closed gas circulation system. The reaction solution was evacuated several times to remove residual air from the reaction solution, and then irradiated under visible light using a 300 W xenon lamp via a cutoff filter ($\lambda \geq 420$ nm) to eliminate ultraviolet (UV) light and a water filter to block infrared light. The amounts of H_2 evolved were measured by gas chromatography (GC-8A, Shimadzu; MS-5A column, TCD, Ar carrier). The catalyst is denoted as Pt (n)/M wt% CdS (D)/TiO_2, where n, M and D are the wt% of Pt based on CdS, wt% of CdS based on TiO_2, and particle size in nm. P25 was used as a TiO_2 support unless otherwise noted.

4-2-4.Photoelectrochemical Measurements

CdS/TiO_2 electrodes were fabricated by spreading a viscous slurry of the prepared powder on fluorine-doped tin oxide (FTO) transparent conductive glass (ca. 20 Ω; Asahi Glass). Before

spreading the slurry, the substrates were ultrasonicated, first in acetone and then in distilled water. The slurry consisted of the sample (0.1 g), water (100 mL), acetylacetone (100 mL), and 10 mL surfactant (Triton X-100, Aldrich). The electrode (coated area: 1×4 cm^2) was then heated in air at 573 K for 1 h to remove organic solvent and surfactant and to improve the contact between catalyst and substrate.

Current–voltage and current–time curves were measured using a conventional Pyrex electrochemical cell attached to a planar side window. The cell consisted of a prepared electrode, a platinum wire counter electrode (diameter: 1 mm, length: 250 mm), and an Ag/AgCl reference electrode. Aqueous solutions of 0.1 M Na_2S–Na_2SO_3 were used as electrolytes. The electrolytes were saturated with argon prior to each electrochemical measurement, and electrode potential was controlled by a potentiostat (HZ-5000, Hokuto Denko or SDPS-501C, Syrinx). Light irradiation was performed using a 300 W xenon lamp with a cutoff filter ($\lambda \geq 420$ nm).

4-3.Results and Discussion

4-3-1. Immobilization of CdS Nanoparticle on TiO_2 Support

4-3-1-1. Characterization of CdS Nanoparticles

The different sized CdS nanoparticles (1.6-12.5 nm) protected by oleyl amine and oleic acid were prepared according to the literature methods.[22-24] Figure 4-1 shows the TEM images of these CdS nanoparticles. All CdS nanoparticles were monodisperse and soluble in nonpolar solvents, such as hexane, toluene and chloroform. As shown in Figure 4-2, UV-vis spectra of 1.6, 2.9, 3.4 and 4.1

nm sized CdS nanoparticles showed exiton peaks at 370, 432, 448, 458 nm, respectively, due to the quantum size effect, whereas 12.5 nm CdS nanoparticles showed bulk like spectrum.

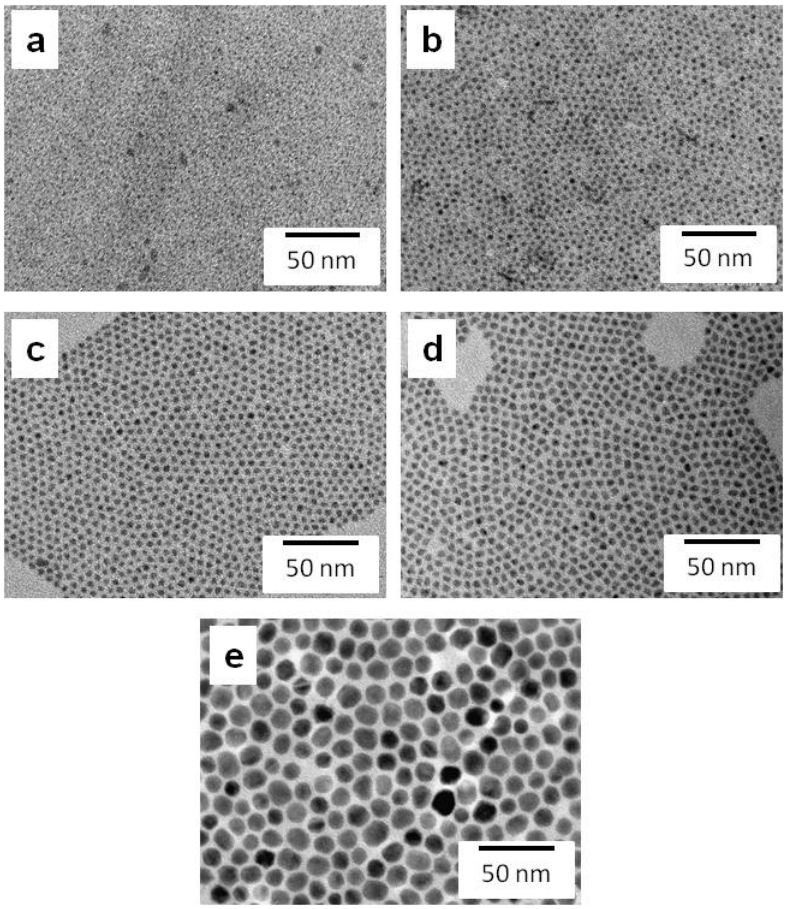

Figure 4-1. TEM images of CdS nanoparticles with (a) 1.6±0.2, (b) 2.9±0.3, (c) 3.4±0.4, (d) 4.1±0.6, and (e) 12.5±1.6 nm in size. The scale bars indicate 50 nm.

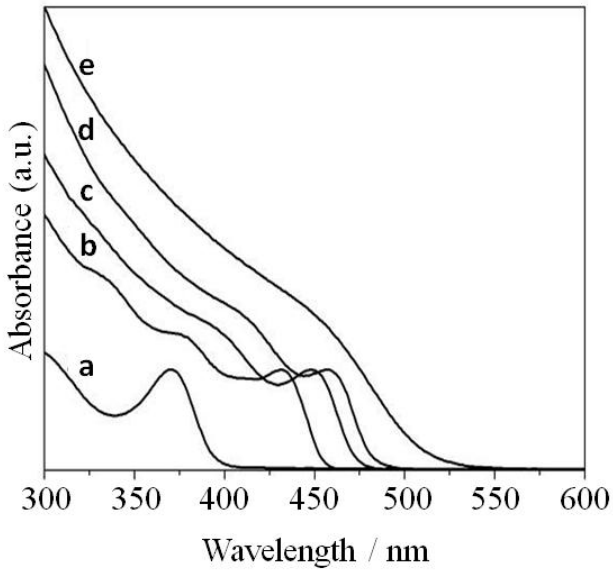

Figure 4-2. UV-Vis spectra of n-hexane solution of CdS nanoparticles with (a) 1.6±0.2 nm, (b) 2.9±0.3, (c) 3.4±0.4, (d) 4.1±0.6, and (e) 12.5±1.6 nm in size

4-3-1-2. Removal of the Protective Ligands

Immobilization of CdS nanoparticles on TiO_2 support was accomplished by sonicating TiO_2 suspension in CdS hexane solution at room temperature. Hexane was proved to be the most effective solvent in supporting as many CdS nanoparticles as possible on TiO_2 owing to the lowest polarity. The prepared CdS nanoparticles were stabilized in the presence of protective ligands, oleic acid (b.p. 468 K), and oleyl amine (b.p. 441 K). The removal of these protective ligands were attempted to improve the accessibility of the CdS surfaces. Figure 4-3 shows the TG-DTA curves under dry flowing air for 0.072 wt% CdS(3.4)/TiO_2 catalysts with (a) no treatment, (b) heat treatment (HT) at 473 K for 5 h, and (c) alkali treatment (AT) in 0.1 M NaOH solution at 298 K for 1 h. The TG profile for non-treated CdS/TiO_2 (Figure 4-3 (a)) shows weight loss at 500-700 K, presumably ascribed to the removal of protective ligands such as oleyl amine and oleic acid and the decomposition of sulfide

to oxide. This is consistent with the observed exothermic profile in the corresponding temperature range, as shown in the DTA curve.[33-35] Bulk CdS showed no weight change at 300-900 K (results not shown). Figures 4-3 (b) and (c) show that heat treatment (HT) at 473 K for 5 h and alkali treatment (AT) drastically reduced the degree of weight loss and exothermicity.

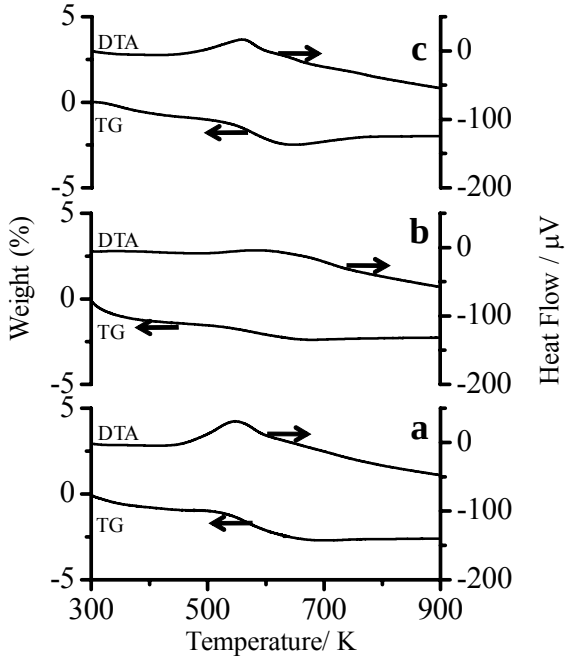

Figure 4-3. TG-DTA curves under dry flowing air for 0.072 wt% CdS (3.4±0.4)/TiO_2 catalysts with (a) no treatment, (b) heat treatment (HT) at 473 K for 5 h, and (c) alkali treatment (AT) in 0.1 M NaOH solution at 298 K for 1 h.

Figure 4-4 shows UV-Vis DRS for (a) TiO_2 (P25) and (b) CdS (Mitsuwa) for reference, and for 0.072 wt% CdS(3.4)/TiO_2 samples with (c) no treatment, (d) HT at 473 K for 5 h, (e) HT at 623 K for 5 h, and (f) AT in 0.1 M NaOH. The absorption band edges of TiO_2 and CdS (Figures 4-4 (a) and (b)) were 380 and 530 nm corresponding to B.G. of 3.26 eV and 2.34 eV, respectively. The absorption peak of the as-prepared CdS nanoparticle (3.4±0.4 nm) was 449 nm (B.G. = 2.76 eV), a

shorter wavelength by about 90 nm than for bulk CdS (blue shift, ΔB.G. = 0.46 eV) due to the quantum size effect. The observed peaks for 0.072 wt% CdS(3.4)/TiO_2 with (c) no treatment, (d) HT method at 473 K, and (f) AT method remained almost unchanged from that of as-prepared CdS nanoparticles, confirming that the methods successfully immobilized CdS nanoparticles while maintaining the particle size. The absorption at wavelengths beyond the absorption edge of CdS, which was observed for CdS(3.4)/TiO_2 by HT at 473 K, was probably due to reduced Cd species. On the contrary, the absorption by CdS nanoparticles completely vanished, and only adsorption due to TiO_2 was observed after HT at 623 K for 5 h (e). Therefore, HT at 473 K and AT methods were used to remove the protective ligands.

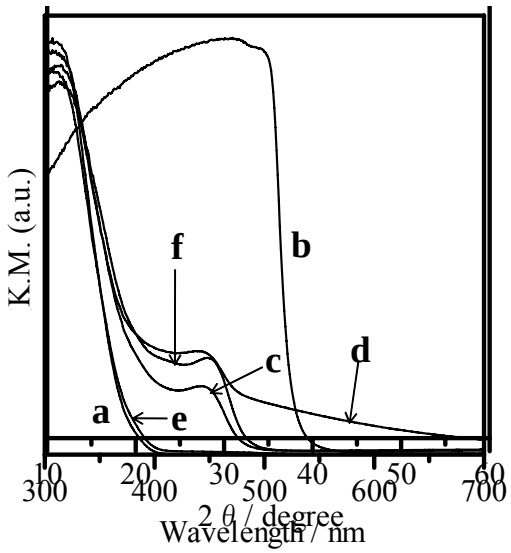

Figure 4-4. UV-Vis DR spectra for (a) TiO_2 (P25), (b) bulk CdS (99.999%, Mitsuwa Chemical), CdS (3.4±0.4 nm)/TiO_2 samples with (c) no treatment, (d) HT at 473 K for 5 h, (e) HT at 623 K for 5 h, and (f) AT in 0.1 M NaOH.

4-3-1-3. Loading of CdS Nanoparticle

Figure 4-5 shows UV-Vis DRS for 0.072 wt% CdS/TiO_2 prepared with different CdS particle sizes (1.6±0.2 (c), 2.9±0.3 (d), 3.4±0.4 (e), 4.1±0.6 (f), and 12.5±1.6 nm (g)) by HT at 473 K for 5 h as well as (a) TiO_2 (P25) and (b) bulk CdS (Mitsuwa). No absorption due to CdS was observed for CdS(1.6)/TiO_2 (Figure 4-5 (c)), which originally showed absorption at 370 nm before immobilization. The CdS(2.9)/TiO_2, CdS(3.4)/TiO_2, and CdS(4.1)/TiO_2 (Figure 4-5 (d)-(f)) showed absorption at 430, 446, and 459 nm, respectively. These absorptions corresponded well to those of the original CdS nanoparticles at 432, 449, and 457 nm for CdS particle sizes of 2.9, 3.4, and 4.1 nm, respectively.[22-24] As seen in Figure 4-5 (g), the CdS(12.5)/TiO_2 absorption edge was observed at 540 nm, matching that of the original CdS nanoparticle (12.5±1.6 nm).[22-24] Therefore, it can be concluded that the optical properties and particle size of CdS supported on TiO_2 remained unchanged from the original CdS particles.

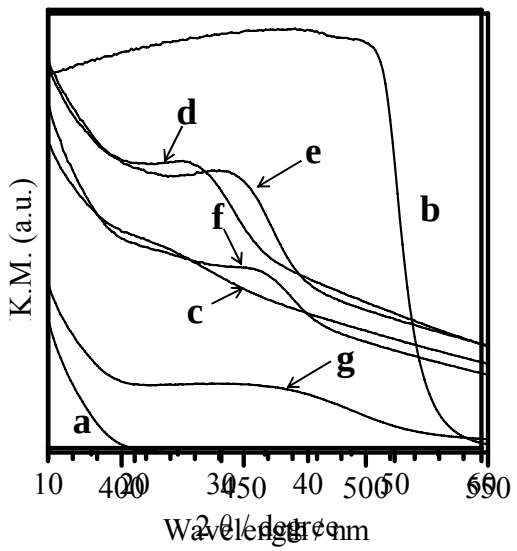

Figure 4-5. UV-Vis DR spectra of (a) TiO_2 (P25), (b) bulk CdS (99.999%, Mitsuwa Chemical), several particle sizes (1.6±0.2 (c), 2.9±0.3 (d), 3.4±0.4 (e), 4.1±0.6 (f), and 12.5±1.6 nm (g)) CdS nanoparticles on TiO_2 by HT method.

Next attempt was to increase the CdS loading on TiO_2 by starting with CdS with a particle size of 3.4±0.5 nm. Figure 4-6 shows UV-Vis DRS for CdS/TiO_2 (0.072-3 wt%-CdS) after HT. The CdS/TiO_2 samples after AT had very similar UV-Vis DRS properties as shown in Figure 4-7. Absorption was observed at 450 nm in the range 0.072-1 wt% CdS loading (Figure 4-6). The absorption edge shifted to longer wavelengths with increasing amount of CdS (1-3 wt%). This indicates that the CdS particles aggregated to form larger particles, where the quantum size effect was no longer operative. Assuming the CdS particles were spherical or square in shape, 14.7 wt% or 11.6 wt% of CdS(3.4) could be theoretically loaded to form a CdS monolayer on TiO_2 (P25, 54 m^2 g^{-1}), respectively. A surface coverage of 6.8% (sphere) or 8.6% (square) was estimated as the loading at which CdS nanoparticles should begin to aggregate in the current treatments.

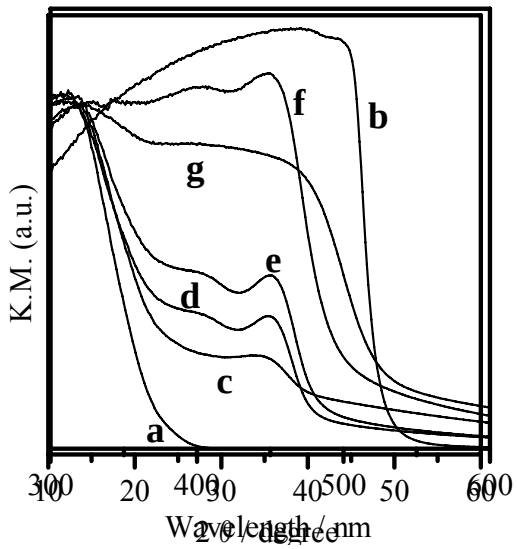

Figure 4-6. UV-Vis DR spectra for (a) TiO_2 (P25), (b) bulk CdS (99.999%, Mitsuwa Chemical), CdS nanoparticles loaded on TiO_2 after HT treatment; The amounts of CdS were (c) 0.072 wt%, (d) 0.3 wt%, (e) 0.7 wt%, (f) 1 wt%, and (g) 3 wt%.

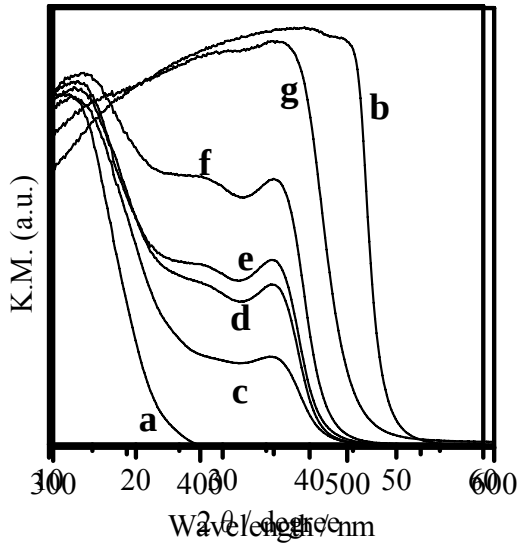

Figure 4-7. UV-Vis DR spectra for (a) TiO_2 (P25), (b) bulk CdS (99.999%, Mitsuwa Chemical), CdS nanoparticles loaded on TiO_2 after AT treatment; The amounts of CdS were (c) 0.072 wt%, (d) 0.3 wt%, (e) 0.7 wt%, (f) 1 wt%, and (g) 3 wt%.

4-3-2. Photocatalytic H_2 Evolution Reaction

Table 4-1 lists the steady-state H_2 evolution rates from 0.1 g of TiO_2 (P25) support only (B.G. = 3.26 eV), 72 μg of CdS nanoparticle colloid without support (B.G. = 2.76 eV), 0.1 g of 0.072 wt% CdS(3.4)/TiO_2 (HT or AT), and 0.1 g of Pt(50) loaded 0.072 wt% CdS(3.4)/TiO_2. No H_2 evolution was detected from TiO_2 support only, due to its obvious lack of visible light response. Although protective ligands should have been removed from CdS particles in Na_2S/Na_2SO_3 solution (pH 13), only negligible H_2 was evolved from CdS nanoparticle colloid (without support), probably because unstable CdS nanoparticles may aggregate easily when they are not immobilized on a support. Supported CdS nanoparticles, on the other hand, had much higher photocatalytic activity (>20 times) than CdS nanoparticles only, although the amounts of CdS in the reaction solution were identical.

Moreover, the deposition of Pt on CdS/TiO_2 considerably enhanced the photocatalytic activity (~ 5 fold). These results clearly show that immobilization of nanoparticles on a support material is essential to establish their intrinsic activity for photocatalytic reaction.

Table 4-1. The rate of H_2 evolution of TiO_2(support), CdS nanoparticle, CdS/TiO_2(no HT), CdS/TiO_2 and $Pt/CdS/TiO_2$

sample	rate of H_2 evolution / μmol h^{-1}
TiO_2	0
CdS nanoparticle	1
CdS/TiO_2(HT)	23
CdS/TiO_2(AT)	68
$Pt/CdS/TiO_2$(HT)	104
$Pt/CdS/TiO_2$(AT)	119

Catalyst (0.1 g): Pt (50 wt% for CdS) - loaded sample, Reactant solution (200 mL): Na_2S (20 mmol) and Na_2SO_3 (20 mmol) /distilled water, Light source: 300 W Xe Lamp with a cutoff filter ($\lambda > 420$ nm).

Unusual properties due to quantum size effects should significantly influence photocatalytic activity, and can be probed by varying CdS particle size. Table 4-2 shows the H_2 evolution rates of the Pt(50)/0.072 wt% CdS/TiO_2 with starting CdS particle sizes of 1.6±0.2, 2.9±0.3, 3.4±0.4, 4.1±0.6, and 12.5±1.6 nm under visible light and UV light irradiation. Under visible light irradiation, the photocatalytic activity increased as particle size increased up to 3.4 nm, but then began to decrease. Under UV-light irradiation, the photocatalytic activity increased with decreasing particle size. The bandgap of CdS nanoparticles measured by UV-Vis DRS (Figure 4-5) and CdS surface area estimated from the particle size assuming a spherical shape are summarized in Table 4-2. With

increasing particle size, the bandgaps narrowed due to quantum size effects. On the other hand, the estimated CdS surface area drastically decreases with increasing particle size. It should be noted that 12.5 nm CdS particles exhibited the bandgap of bulk CdS material. The photocatalytic activity should be affected by absorptions of visible and UV light by the catalysts, and the ease of oxidation and reduction determined by the positions of the conduction and valence bands of the catalysts. Under UV light irradiation, the H_2 evolution rate decreased with increasing initial CdS particle size, corresponding to a decrease in bandgap (i.e., oxidation-reduction ability) and an increase in surface area. Under visible light irradiation, CdS samples with 1.6 nm particles did not have sufficient absorption in the visible light region (absorption: 370 nm), resulting in a comparatively low H_2 evolution rate. By increasing CdS particle size beyond 3.4 nm, the photocatalytic activity decreased because of a depression of the oxidative-reductive power with a narrower bandgap. It is notable that nanoparticles exhibiting quantum size effects gave much higher rates than the 12.5 nm CdS sample, which had bulk CdS nature, suggesting that utilization of these nanoparticles had significant benefits for this reaction.

Table 4-2. The rate of H_2 evolution for several particle sizes of CdS (1.6±0.2, 2.9±0.3, 3.4±0.4, 4.1±0.6, and 12.5±1.6 nm) loaded on TiO_2.

diameter / nm	band gap / eV	surface area[a] / m^2 g^{-1}	H_2 evolution rate[b] / μmol h^{-1}
1.6±0.2	3.35	778	43(346)
2.9±0.3	2.87	429	60 (-)
3.4±0.4	2.76	356	104(227)
4.1±0.6	2.71	304	66(106)
12.5±1.6	2.34	89	2(6)

a. Surface areas are estimated by particle size in assumption to sphere in shape
b. Catalyst (0.1 g): Pt (50 wt% for CdS) - loaded sample, Reactant solution (200 mL): Na_2S (20 mmol) and Na_2SO_3 (20 mmol) /distilled water, Light source: 300 W Xe Lamp with a cutoff filter (λ > 420 nm). This value in parenthesis is the rate of H_2 evolution under light irradiation (λ > 300 nm). In the case of CdS(2.9)/TiO_2 was not measured.

Next, the effects of the TiO_2 support surface area on the photocatalytic activity were investigated. TiO_2 support candidates were rutile (S_{BET} = 4 m^2 g^{-1}), anatase (S_{BET} = 29 m^2 g^{-1}), anatase (S_{BET} = 103 m^2 g^{-1}), and P25 (ca. 70% anatase, 30% rutile, S_{BET} = 54 m^2 g^{-1}). The H_2 evolution rates for the CdS(3.4)/TiO_2 catalysts are plotted against BET surface area in Figure 4-8. Without support (plots at x=0 in Figure 4-8), the photocatalytic activity for CdS nanoparticles was almost negligible, clearly demonstrating the positive effects of CdS nanoparticle dispersion onto the support. Even for the low loading of 0.072 wt%, the H_2 evolution rate was lower for a low-surface-area rutile sample than for other samples with higher surface areas. The comparable rates for the latter samples indicate that nanoparticles were well-dispersed on the support at low CdS loading (0.072 wt%). For 0.3 wt% CdS loaded samples, the photocatalytic activity increased with increasing the surface area of the support by 54 m^2 g^{-1}. It is clear that a higher surface area support can disperse the active CdS species more efficiently, resulting in enhancement of the H_2 evolution

rate. 0.3 wt% CdS/TiO_2 samples showed higher activity than 0.072 wt% CdS/TiO_2 samples.

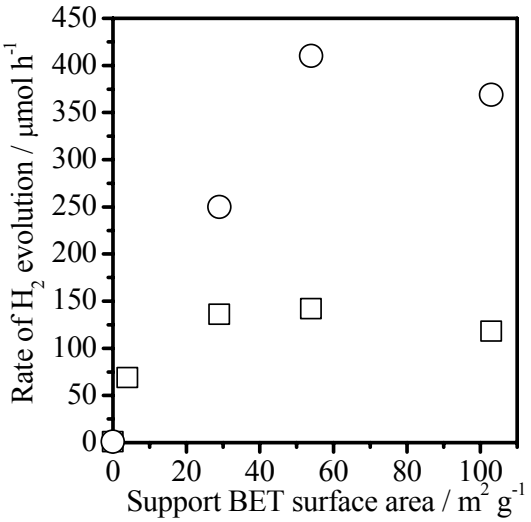

Figure 4-8. Dependence of the rate of H_2 evolution from Pt (100 wt%) / CdS ((□)0.072 and (○)0.3, particle size = 3.4 nm) / TiO_2 by HT upon the BET surface area ; support candidates were rutile (S_{BET} = 4 m^2 g^{-1}), anatase (S_{BET} = 29 m^2 g^{-1}), anatase (S_{BET} = 103 m^2 g^{-1}), and P25 (S_{BET} = 54 m^2 g^{-1}). Catalyst (0.1 g): Pt (50 wt% for CdS) - loaded sample, Reactant solution (200 mL): Na_2S (20 mmol) and Na_2SO_3 (20 mmol) /distilled water, Light source: 300 W Xe Lamp with a cutoff filter (λ > 420 nm).

Dependence of the rate of H_2 evolution upon the amount of Pt cocatalyst loaded on 0.072 wt% CdS(3.4)/TiO_2 were shown in Figure 4-9. The Pt (100) loaded photocatalyst showed high activity. This figure indicates that the maximum photocatalytic activity increased from 100 wt% up to Pt (100) for CdS(3.4)/. This dramatically higher than the maximum amount (1-3 wt%) of bulk CdS and corresponds to an increase in activity sites per unit weight (BET surface area of bulk CdS: 0.9 m^2g^{-1}, Specific surface area of loading 3.4 nm-CdS nanoparticle: 356 m^2g^{-1}). For 1 wt% Pt loading on TiO_2,

the initial rate was the same as for 100 wt% Pt on CdS, and the photocatalytic activity after 1 h was in activated. This may be because Pt on CdS was aggregated beyond 100 wt% for CdS. Elemental analysis by EDX showed that Pt existed in the neighborhood of CdS.

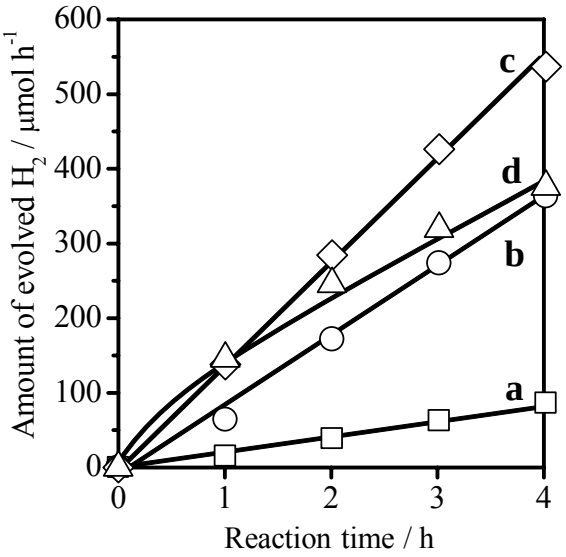

Figure 4-9. Time course of H_2 evolution of non loaded (a), and several amounts of Pt (b) 50 wt%, (c) 100 wt% for CdS and (d) 1 wt% for TiO_2 on 0.072 wt% CdS/TiO_2 by HT (0.1 g). Catalyst (0.1 g): Pt (non or several wt% for CdS) - loaded sample, Reactant solution (200 mL): Na_2S (20 mmol) and Na_2SO_3 (20 mmol) /distilled water, Light source: 300 W Xe Lamp with a cutoff filter ($\lambda > 420$ nm).

The H_2 evolution rate is plotted against the amount of CdS(3.4) in HT (a) or AT (b) in Figure 4-10. The H_2 evolution rates for the catalysts obtained by HT or AT reached maxima when 0.7 or 0.3 wt% of CdS was loaded, respectively. The rate drastically decreased for highly loaded (1 wt%) samples. UV-Vis spectra (Figure 4-6 and Figure 4-7) showed that the absorption shifted to wider wavelength (narrower bandgap) compared to samples with lower loading, indicating that particle size

increased with increasing amount of CdS, while photocatalytic rates decreased accordingly. These results suggest that the immobilization of CdS nanoparticles exhibiting quantum size effects resulted in high-efficiency H_2 evolution.

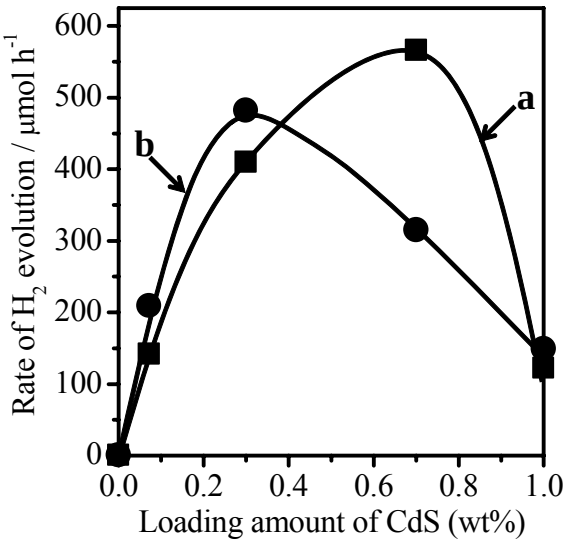

Figure 4-10. Dependence of the rate of H_2 evolution on the loading amount of CdS in HT (a) or AT (b). Catalyst (0.1 g): Pt (100 wt% for CdS) - loaded sample, Reactant solution (200 mL): Na_2S (20 mmol) and Na_2SO_3 (20 mmol) /distilled water, Light source: 300 W Xe Lamp with a cutoff filter ($\lambda > 420$ nm).

Finally, photocatalytic measurements were carried out of Pt(100)/0.3 wt% CdS(3.4)/TiO_2 with AT followed by HT at 473 K under visible light irradiation in the presence of Na_2S-Na_2SO_3. The rate of H_2 evolution was 616 μmol h^{-1}, the highest value observed in this study and remained constant for 5 h as shown in Figure 4-11. Figure 4-12 shows the wavelength dependence of photocatalytic H_2 evolution from aqueous Na_2S-Na_2SO_3 solution over Pt(100)/0.3 wt% CdS(3.4)/TiO_2 catalyst. The H_2 evolution rate decreased with increasing cutoff wavelength, corresponding to excitation at the

absorption edge of CdS nanoparticles (3.4±0.4 nm). It is confirmed that these photocatalytic H_2 evolution reactions occur by the photogeneration of electrons and holes under visible light irradiation in the presence of Na_2S-Na_2SO_3.

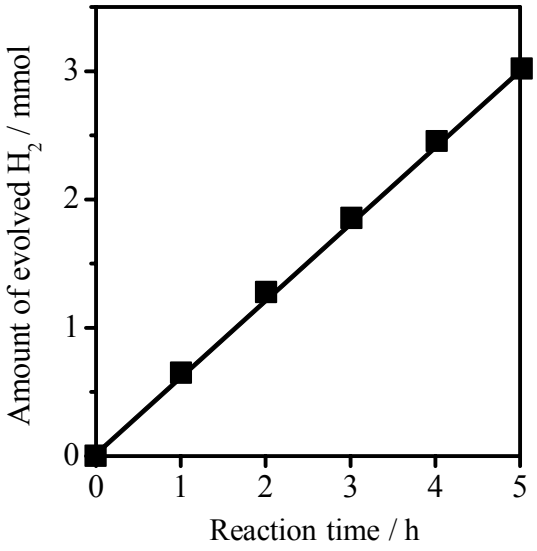

Figure 4-11. Time course of H_2 evolution for Pt (100) / 0.3 wt% CdS (3.4)/TiO_2 with AT followed by HT. Catalyst (0.1 g): Pt (100 wt% for CdS) - loaded sample, Reactant solution (200 mL): Na_2S (20 mmol) and Na_2SO_3 (20 mmol) /distilled water, Light source: 300 W Xe Lamp with a cutoff filter ($\lambda > 420$ nm).

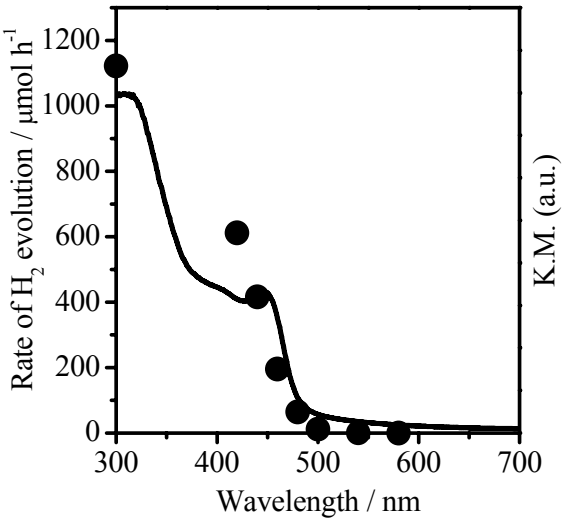

Figure 4-12. Wavelength dependence of the steady rate of H_2 evolution and UV-Vis DRS results for Pt (100 wt% for CdS) / CdS (0.3 wt%) / TiO_2 (P25) with AT followed by HT. Catalyst (0.1 g): Pt (100 wt% for CdS) - loaded sample, Reactant solution (200 mL): Na_2S (20 mmol) and Na_2SO_3 (20 mmol) /distilled water, Light source: 300 W Xe Lamp with a cutoff filter ($\lambda > 420$ nm).

4-3-3. Photoelectrochemical Measurements

Figure 4-13 shows the current-voltage curves for 0.3 wt% CdS(3.4)/TiO_2 sprayed on an FTO electrode compared to bulk CdS (99.999%, Mitsuwa Chemical) in a solution containing Na_2S and Na_2SO_3 as sacrificial electron donors (pH 13) under visible light (λ>420 nm). The measurements were conducted by scanning potential from -1.5 V to 0 V versus Ag/AgCl. The observed anodic photocurrent is attributed to oxidation of Na_2S and Na_2SO_3, indicating that the CdS(3.4)/TiO_2 functioned as an n-type semiconductor as shown in Figure 4-14. A photocurrent onset for CdS(3.4)/TiO_2 was observed at -1.45 V; a -0.37 V negative shift compared to bulk CdS electrode (-0.108 V). From UV-Vis DRS, the bandgap of CdS(3.4)/TiO_2 and bulk CdS/TiO_2 were determined

to be 2.76 and 2.34 eV, respectively, and the difference in bandgap was 0.42 eV, very similar to the difference of onset potential. Thus the difference in bandgap mainly originated from the difference in conduction edges, and the positions of the valence bands of CdS(3.4)/TiO_2 and bulk CdS/TiO_2 were very similar, as reported previously.[17] The large difference in photocatalytic activity for H_2 evolution between quantum dot CdS(3.4)/TiO_2 and bulk-like CdS(12.5)/TiO_2 as discussed above (Table 4-2), can be attributed to the high reduction capability of quantum dot CdS derived from a negatively shifted conduction edge. In addition, a large photocurrent was observed for CdS/TiO_2 (6.8 mA cm^{-2} at -0.2 V versus Ag/AgCl) compared to bulk CdS (0.1 mA cm^{-2} at -0.2 V versus Ag/AgCl), reflects the high reduction capability of quantum dot CdS, and possible charge separation by TiO_2 support when photoexcited electrons migrate to the TiO_2 support to facilitate photoelectric reaction.[29, 31]

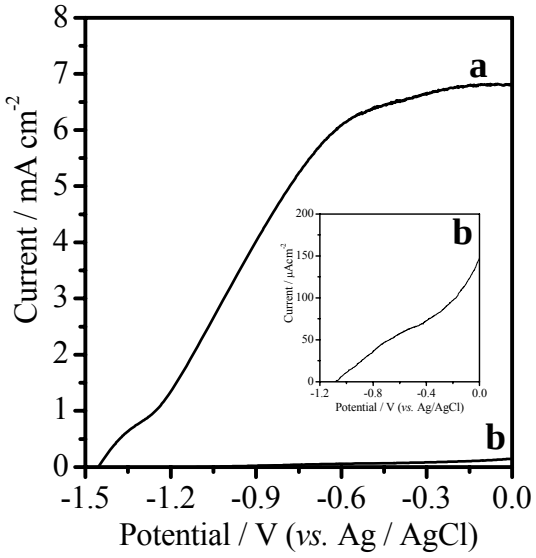

Figure 4-13. Photocurrent versus voltage of CdS (0.3 wt%) / TiO_2 (P25) after AT followed by HT on FTO in 0.1 M Na_2S-Na_2SO_3 solution at -0.2 V versus Ag/AgCl under visible irradiation at $\lambda \geq 420$ nm.

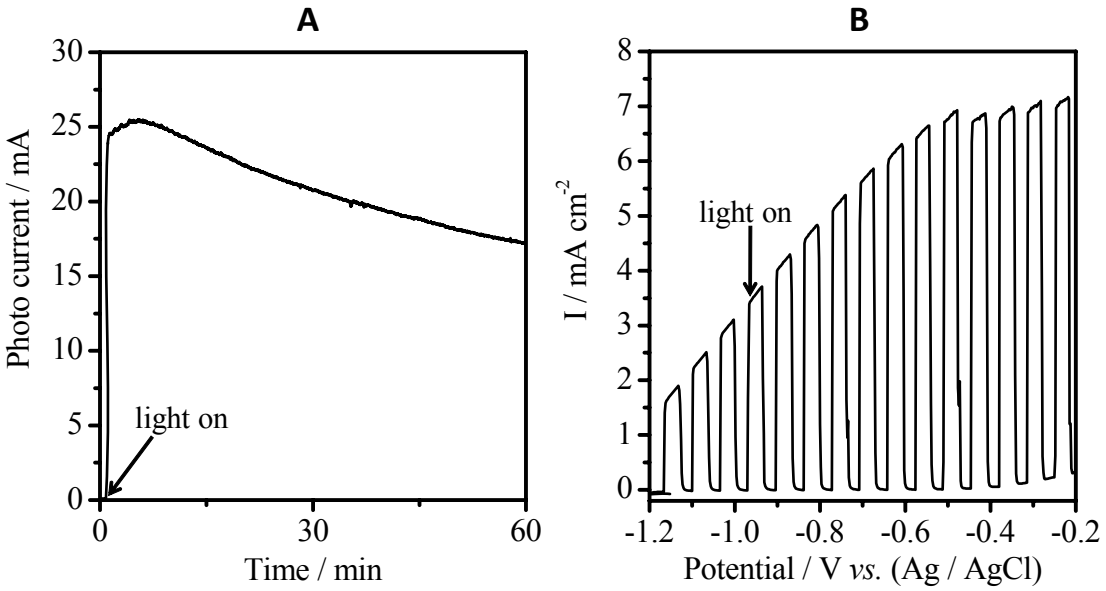

Figure 4-14. The (A) current-time at -0.2 V vs. Ag/AgCl and (B) the current-potential curves for 0.3 wt% CdS(3.4)/TiO_2 on FTO electrode in a solution containing Na_2S and Na_2SO_3 as sacrificial electron donors under intermittent irradiation.

Figure 4-15 shows the dependence of IPCE (-0.2 V versus Ag/AgCl) on the cutoff wavelength of incident light for the 0.3 wt% CdS/TiO_2 electrode. The incident photon-to-photocurrent efficiency, *IPCE*, is defined by the following equation.

$$IPCE(\%) = \frac{hc}{e}\frac{i_{photo}}{\lambda \Phi} \times 100$$

where i_{photo}, λ, and Φ are photocurrent density (A m^{-2}), wavelength (m), and light flux (W m^{-2}), and c, h and e are the speed of light (2.998 × 10^8 m s^{-1}), Plank's constant (6.626 × 10^{-34} W s), and the elementary electric charge (1.602 × 10^{-19} A s). A monochromatic light source (Asahi Spectra MAX-301) was used with a bandpath filter (half bandwidth: ±10 nm) in the wavelength region of 420 to 560 nm. The DRS results for the 0.3 wt% CdS(3.4)/TiO_2 powder are also shown. Photocurrent was observed at up to 500 nm, and the variation in photocurrent with respect to wavelength was in

good agreement with the DRS results. The observed photocurrent can thus be attributed to a photoelectrochemical oxidation reaction via the bandgap transition of CdS. The IPCE at 420 nm for CdS/TiO_2 at -0.2 V versus Ag/AgCl was thus derived to be 12.9 %.

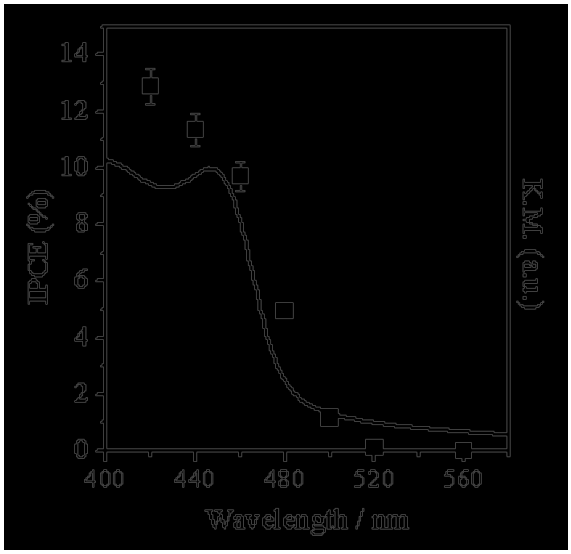

Figure 4-15. Wavelength dependence of IPCE and UV-Vis DRS results for CdS (0.3 wt%) / TiO_2 (P25) with AT followed by HT on FTO in 0.1 M Na_2S-Na_2SO_3 solution at -0.2 V versus Ag/AgCl under visible irradiation at $\lambda \geq 420$ nm.

4-4. Conclusion

CdS nanoparticles dispersed on TiO_2 to maintain particle size were successfully prepared by heat treatment and alkali treatment to effectively remove protective ligands. The photocatalytic measurements suggest that CdS/TiO_2 catalyzed the reduction of H^+ to H_2 under visible light irradiation in the presence of a sacrificial electron donor (Na_2S-Na_2SO_3). Quantum size effects in CdS particles on TiO_2 were observed from 1.6 to 4.1 nm (1.6±0.2, 2.9±0.3, 3.4±0.4, and 4.1±0.6), and the photocatalytic activity was maximum at 3.4±0.4 nm, about fifty times higher than 12.5±1.6

nm CdS with similar properties to bulk CdS. To further investigate the preparation method, the loading amount of CdS or Pt and several supports with different surface areas were examined. The photocatalytic activity was 616 μmol h^{-1} at Pt (100 wt% for CdS)/CdS (0.3 wt%)/TiO_2 (P25, S_{BET} = 54 m^2 g^{-1}) after alkali treatment followed by heat treatment. For CdS/TiO_2 on an FTO electrode, photoanodic current (6.8 mA cm^{-2}) was measured in the presence of 0.1 M Na_2S-Na_2SO_3 under visible irradiation (λ>420 nm). It was shown that CdS functions as a high activity n-type semiconductor. The high efficiency was attributed not only to quantum size effects, but also to charge separation due to the difference between the bottoms of the conduction bands of CdS and TiO_2. There are still large margin for photocatalytic activity improvement by optimizing type and surface area of the support with supplementary deposition of CdS. The knowledge acquired in this study can be applied for general usage of organic-ligand protected nanoparticle materials.

References

1. A. Fujishima and K. Honda, *Nature (London)*, **238**, 37 (1972).

2. K. Domen, A. Kudo, and T. Ohnishi, *J. Catal.*, **102**, 92 (1986).

3. A. Kudo, and H. Kato, *Chem. Phys. Lett.*, **331**, 373 (2000).

4. J. F. Reber, and K. Meier, *J. Phys. Chem.*, **88**, 5903 (1984).

5. A. Kudo, I. Nagane, I. Tsuji, and H. Kato, *Chem. Lett.*, **9**, 882 (2002).

6. I. Tsuji, H. Kato, H. Kobayashi, and A. Kudo, *J. Am. Chem. Soc.*, **126**, 13406 (2004).

7. R. J. Williams, *Chem. Phys.*, **32**, 1505 (1960).

8. H. J. Gerisher, *Electroanal. Chem. Interfacial Electrochem.*, **58**, 263 (1975).

9. J. R. Wilson, and S. -M. J. Park, *Electrochem. Soc.*, **129**, 149 (1982).

10. J. R. Darwent, *J. Chem. Soc., Faraday Trans.2*, 77, 1703 (1981).

11. J. R. Harbour, R. Wolkow, and M. L. Hair, M. L. *J. Phys. Chem.*, **85**, 4026 (1981).

12. T. Inoue, T. Watanabe, A. Fujishima, and K. Kobayakawa, *J. Electrochem. Soc.*, **124**, 719 (1977).

13. H. Minoura, and M. Tsuiki, *Electrochimica Acta*, **23**, 1377 (1978).

14. K. R. Gopidas, M. Bohorquez, and P. V. Kamat, *J. Phys. Chem.*, **94**, 6435 (1990).

15. S. Hotchandani, and P. V. Kamat, *J. Phys. Chem.*, **96**, 6934 (1992).

16. A. Eychmueller, A. Haesselbarth, and H. J. Weller, *Lumines.*, **53**, 113 (1992).

17. L. E. Brus, *J. Chem. Phys.*, **80**, 4403 (1984).

18. Y. Nosaka, *J. Phys. Chem.*, **95**, 5054 (1991).

19. Y. Wang, *Acc. Chem. Res.*, **24**, 133 (1991).

20. A. Henglein, *Chem. Rev.*, **89**, 1861(1989).

21. Al. L. Efros, and A. L. Efros, *Sov. Phys. Semicond.*, **16**, 772 (1982).

22. T. Teranishi and M. Kanehara, unpublished work.

23. J. Joo, H. B. Na, T. Yu, J. H. Yu, Y. W. Kim, F. Wu, J. Z. Zhang, and T. Hyeon, *J. Am. Chem. Soc.*, **125**, 11100 (2003).

24. M. Kanehara, H. Arakawa, R. Hironaga, and T. Teranishi, *Trans. Mater. Res. Soc. Jpn.*, **31**, 437 (2006).

25. S. G. Hickey, D. J. Riley, and E. J. Tull, *J. Phys. Chem. B*, **104**, 7623 (2000).

26. T. Hirai, Y. Bando, and I. Komasawa, *J. Phys. Chem. B*, **106**, 8967 (2002).

27. J. C. Yu, L. Wu, J. Lin, P. Li, and Q. Li, *Chem. Commun.*, 1552 (2003).

28. J. C. Tristão, F. Magalhães, P. Corio, and M. T. C. Sansiviero, *J. Photochem. Photobiol. A*, **181**, 152 (2006).

29. S. Chen, M. Paulose, C. Ruan, G. K. Mor, O. K. Varghese, D. Kouzoudis, and C. A. Grimes, *J. Photochem. Photobiol. A*, **177**, 177 (2006).

30. J. S. Jang, W. Li, S. H. Oh, and J. S. Lee, *Chem. Phys. Lett.*, **425**, 278 (2006).

31. H. Park, W. Choi, and M. R. Hoffmann, *J. Mater. Chem.*, **18**, 2379 (2008).

32. C. F. Chi, Y. L. Lee, H. S. Weng, *Nanotechnology*, **125**, 704 (2008).

33. P. J. Sebastian, and M. E. Calixto, *Thin Solid Films*, **360**, 128 (2000).

34. F. E. Tantawy, K. M. A. Kader, F. Kaneko, and Y. K. Sung, *European Polymer Journal*, **40**, 415 (2004).

35. L. Yang, Q. Shen, J. Zhou, and K. Jiang, *Materials Letters*, **59**, 2889 (2005).

Chapter 5

Conclusions

This thesis discusses synthesis and photocatalytic performance of novel (oxy)sulfide materials in attempt to achieve visible light driven overall water splitting. This study demonstrates development of oxysulfides with metal ions with d^0 or d^{10} electronic configuration, with adequate cocatalyst introduction using other elements on the material surfaces. The thesis also describes application of well-size-defined cadmium sulfide nanoparticles exhibiting quantum size effect, by immobilizing them on oxide surfaces so as to maximize activity for photocatalytic and photoelectrochemical reactions under visible light. The thesis consists of 5 chapters as described below.

Chapter 1: This chapter describes the background of this research and basic principles of photocatalytic reactions including overall water splitting. The strategies for development of visible light driven photocatalysts are also discussed.

Chapter 2: This chapter describes development of novel oxysulfides as visible light driven photocatalysts, which consist of metal ions (Cu^+, Zn^{2+}, Ga^{3+}, In^{3+}, Ge^{4+}, and Sn^{4+}) with d^{10} electronic configuration. In particular, La-Ga based materials; $LaGaO_3$, $LaGaS_2O$, and La_3GaS_5O are focused. La_3GaS_5O oxysulfide is prepared, characterized and tested for photoelectrochemical measurements and photocatalytic reactions. The band-gap energies of $LaGaS_2O$ and La_3GaS_5O are estimated from diffuse reflectance UV-Vis spectra to be 3.0 eV and 2.3 eV, respectively. This result clearly indicates that the band gap becomes narrower with increasing sulfur content, making it possible to absorb light at visible region. Investigation of the electronic band structure shows that the upper part of the valence band is composed of S 3p orbitals, resulting in the narrower band gap of La_3GaS_5O than

those of $LaGaO_3$ and $LaGaS_2O$. La_3GaS_5O prepared on FTO is shown to function as an n-type semiconductor in the presence of 0.01 M Na_2S–Na_2SO_3 and 0.1 M Na_2SO_4 under visible irradiation ($\lambda \geq 420$ nm). The band-gap positions of these oxysulfides are located at suitable potentials for the reduction and oxidation of water. The results of photocatalytic activity on these La-Ga based oxysulfides in the presence of sacrificial reagents show that the photodeposition of Ru or Pt on La_3GaS_5O significantly promotes the H_2 evolution. The deposition of colloidal IrO_2 on La_3GaS_5O also promotes O_2 evolution. Although over all water splitting under visible irradiation has not been achieved on these materials, the obtained results clearly show that these oxysulfide materials are good candidates for these visible light driven photoreactions, yet requiring further investigation.

Chapter 3: This chapter discusses the possibility of new oxysulfide materials based on metal ions (Ti^{4+}, Nb^{5+}, and Ta^{5+}) which possess d^0 electronic configuration as visible light driven photocatalysts by examining the photocatalytic reactions and photoelectrochemical measurements. In particular, surface modification of $Sm_2Ti_2S_2O_5$ using cocatalysts is investigated in attempt to achieve overall water splitting reaction. Modification with two different functioning materials for H_2 and O_2 evolutions, respectively, has been designed in order to promote both H_2 and O_2 evolution reactions simultaneously during overall water splitting reaction. Rh/Cr_2O_3 cocatalyst shows highest rates for H_2 evolution in the presence of Na_2S-Na_2SO_3 sacrificial reagents. IrO_2 colloid, MnO_2, and Co_3O_4 cocatalysts promote O_2 evolution rates in the presence of Ag^+ sacrificial reagent. These results show that the materials have potential for overall water splitting with adequate band positions. The overall water splitting reaction, however, has not been achieved on the promoted $Sm_2Ti_2S_2O_5$ photocatalysts,

suggesting that the presence of sacrificial reagents is essential for the investigated materials.

Chapter 4: This chapter describes the application of CdS nanoparticles exhibiting quantum size effect dispersed on TiO_2 for the photocatalytic and photoelectrochemical reactions by immobilization onto oxide support. The CdS nanoparticles used in this study are originally stabilized in the presence of oleic acid and oleyl ammine as protective ligands, which have to be removed prior to photocatalytic reactions. UV-Vis spectroscopic results indicate that the original size of the CdS nanoparticles is successfully retained after immobilization on TiO_2 and removal of the protective ligands by oxidative treatment in flowing air at 473 K or alkali treatment at ambient temperature. By varying the original particle size of the CdS, H_2 evolution rates at different light wavelengths are correlated with CdS particle size (quantum size effect) using CdS/TiO_2 catalysts. H_2 evolution rate using Na_2S-Na_2SO_3 sacrificial reagents significantly depends on CdS particle size and the highest rate is observed with a CdS particle size of ~3.4 nm under visible light irradiation (>420 nm), probably due to appropriate band gap and position, which significantly changes in this range of particle size. Modification of the CdS/TiO_2 catalysts by photodeposition of Pt drastically enhances H_2 evolution rates. CdS/TiO_2 catalyst suspended on a fluoride tin oxide (FTO) electrode functions as an n-type semiconductor in Na_2S-Na_2SO_3 aqueous solution with high photoelectric current.

Chapter 5: The results described in the Chapters 1-5 are summarized.

Some novel oxysulfide materials with d^0 or d^{10} electronic configuration were demonstrated to have a potential as a visible light driven photocatalyst for water splitting reaction as shown in the

Chapter 2 and 3. It was also found that the photocatalytic activities were affected by the preparation condition of oxysulfide, the reaction conditions, and surface modifications. In particular (Chapter 3), cocatalyst loaded $Sm_2Ti_2S_2O_5$ was effectively proceeded H_2 and O_2 evolution reactions in the presence of sacrificial reagents. However, the overall water splitting reactions over two different cocatalysts which are loaded on oxysulfides as H_2 and O_2 evolution sites have not been achieved. This result suggested that cocatalyst did not function as H_2 or O_2 evolution site. Therefore, further investigation for appropriate and selective surface modification of both H_2 and O_2 evolution cocatalysts are necessary.

The author also has succeeded that CdS nanoparticles were immobilized on TiO_2 with maintaining their original particle size and optical property after impregnation and removal of the protective ligands by oxidative heat treatment and/or alkali treatment. The photocatalytic H_2 evolution rates in Na_2S-Na_2SO_3 solution under visible light were strongly affected by the CdS particle size (quantum size effect), CdS loading amount, and TiO_2 surface area. The findings in this study can be extended information to further development in the field of nanoparticle materials covered with protective ligands.

The author believes that the present results are expected to give important information for the research fields. Finally, the author would like to expect this research field to be progressed more in the future.

List of publications (peer reviewed papers)

1. Lanthanum-Indium Oxysulfide as a Visible Light Driven Photocatalyst for Water Splitting

   Kiyonori Ogisu, Akio Ishikawa, Kentaro Teramura, Kenji Toda, Michikazu Hara, and Kazunari Domen

   Chemistry Letters, **36**, 854-855 (2007).

2. Electronic Band Structures and Photochemical Properties of La-Ga based Oxysulfides

   Kiyonori Ogisu, Akio Ishikawa, Yoshiki Shimodaira, Tsuyoshi Takata, Hisayoshi Kobayashi, and Kazunari Domen

   Journal of Physical Chemistry C, **112**, 11978-11984 (2008).

3. Structure and Electron Density of Oxysulfide $Sm_2Ti_2S_2O_{4.9}$, a Visible-Light-Responsive Photocatalyst

   Yashima, Masatomo, Kiyonori Ogisu, Kazunari Domen

   Acta Crystallographica Section B: Structural Science, **B64**, 291-298 (2008).

4. Application of CdS Nanoparticles Exhibiting Quantum Size Effect by Dispersed on TiO_2: Photocatalytic H_2 evolution and Photoelectrochemical Measurements

   Kiyonori Ogisu, Kazuhiro Takanabe, Masaki Saruyama, Takahiro Ikeda, Masayuki Kanehara, Toshiharu Teranishi, Kazunari Domen.

   Bulletin of the Chemical Society of Japan, in press.

Others

1. Thermal Response of Graphite Electrode to Electrochemical Intercalation and De-intercalation of Cations

   Yasuhisa Maeda, Kiyonori Ogisu

   Tanso, **215**, 252-254 (2004).